Abstract

Cross section of bottom electrons in proton-proton collisions in the ALICE experiment

Tomas Robert Prem-Raj Aronsson

2014

High-energy heavy-ion collisions at the LHC allow for the study of the properties of the quark-gluon plasma (QGP). Heavy quarks, charm and bottom, produced in the initial hard-scattering processes of the collision are excellent probes of the QGP. When heavy quarks traverse the QGP they are expected to lose energy and such energy loss is predicted to be smaller than for gluons and light quarks. On the other hand, recent experimental data indicate larger energy loss than expected. Heavy-flavor production can be studied using electrons from semi-leptonic decays of hadrons containing charm and bottom quarks. The separation of electrons from these two sources (charm and bottom) is of crucial importance to address the expected mass dependence of energy loss. The ALICE EMCal detector possesses outstanding particle identification for electrons at high p_T, and this detector is used to identify electrons with high purity. A two-track algorithm to select secondary vertices involving these electrons and surrounding charged tracks was developed and implemented, so called b-tagging; exploiting the tracking precision provided by the Inner Tracking System the electron and surrounding tracks are used to select displaced decay vertices that are likely to originate from B-hadron decay. Bottom electron production in the transverse momentum range 7-13 GeV/c in 7 TeV pp collisions is measured. The invariant cross section for bottom-decay electrons is calculated and compared to fixed ordered next-to-leading-log (FONLL) pQCD predictions. This will serve as a reference for studies of bottom suppression in PbPb collisions.

Cross section of bottom electrons in proton-proton collisions in the ALICE experiment

A Dissertation
Presented to the Faculty of the Graduate School
of
Yale University
in Candidacy for the Degree of
Doctor of Philosophy

by
Tomas Robert Prem-Raj Aronsson

Dissertation Director: John W. Harris

2014

Table of Contents

Abstract **i**

List of Figures **ix**

List of Tables **xvii**

Acknowledgments **xix**

1 Introduction **1**
1.1 The Standard Model . . . 2
1.2 QCD . . . 5
1.3 The QGP and heavy-ion collisions . . . 7
1.4 Observables of the QGP . . . 10
1.4.1 Collective Flow . . . 10
1.4.2 Jet Tomography . . . 12
1.4.3 Nuclear Modification Factor . . . 13
1.4.4 Strangeness Enhancement . . . 15
1.4.5 Quarkonia Suppression . . . 16
1.5 Heavy Flavor . . . 17
1.5.1 Previous measurements . . . 19

2 The Experiment **23**
2.1 LHC . . . 23
2.2 ALICE . . . 25
2.2.1 Tracking in ALICE . . . 25
2.2.2 ITS . . . 26
2.2.3 TPC . . . 32
2.2.4 EMCal . . . 39
2.3 ALICE data analysis . . . 42
2.3.1 GRID computing . . . 42
2.3.2 Analysis trains and local clusters . . . 43

3 Electromagnetic calorimeters **45**
3.1 Electromagnetic calorimetry . . . 45
3.1.1 Particle interaction with the EMCal, shower development . . . 46
3.1.2 Energy response and non-linearity . . . 48

3.2 The ALICE EMCal . . . 48
3.3 The ALICE EMCal mini-module analysis . . . 52
3.3.1 The EMCal mini-module . . . 53
3.3.2 Non-linearity and energy resolution . . . 63
3.3.3 Shower shape studies and particle identification . . . 64
3.3.4 Conclusion . . . 74

4 Analysis of electrons **77**
4.1 Event selection . . . 77
4.1.1 Off-line event selection . . . 79
4.1.2 Simulation data . . . 81
4.2 Tracking . . . 83
4.2.1 ITS TPC data QA . . . 84
4.2.2 Tracking Efficiency . . . 87
4.2.3 p_T Unfolding . . . 91
4.3 Particle identification . . . 93
4.3.1 Track matching and E/p . . . 93
4.3.2 EMCal QA . . . 94
4.3.3 Efficiency & Purity TPC-EMCal . . . 98
4.3.4 Purity - EMCal . . . 102
4.4 Trigger correction . . . 104

5 B-tagging **109**
5.1 B-tagging Algorithm within ALICE . . . 111
5.1.1 Associated Hadron selection . . . 111
5.1.2 B-tagging Parameters . . . 112
5.1.3 Rejection of bad secondary vertices . . . 114
5.2 Optimization of parameters . . . 114
5.3 B-tagging Background Estimation and Subtraction . . . 118
5.3.1 Different methods to remove background . . . 120
5.3.2 Electron purity versus hadrons of b-tagged sample . . . 123

6 Estimation of Systematic Errors **125**
6.1 Systematic Errors . . . 125
6.2 Tracking and Unfolding . . . 126
6.3 Unfolding systematic error . . . 127
6.4 PID efficiency systematic error . . . 129
6.5 Trigger Correction . . . 131
6.6 B-tagging . . . 131
6.7 Combined Systematic Errors . . . 134

7 Results and conclusion **135**
7.1 Non-subtracted b-electron cross section . . . 135
7.2 b-electron cross section . . . 136
7.3 Conclusion . . . 137

Appendix A - Effective Signal **143**

Bibliography **145**

List of Figures

1.1 Elementary particles within the Standard Model. The three different generations are represented as the first three columns, with the mass increasing left to right. The last full column represent the gauge bosons. Finally, the Higgs boson (top right) has been "discovered", which adds to the success of the Standard Model. 3

1.2 The strong coupling constant α_s as a function of the energy scale Q. The respective degree of QCD perturbation theory used in the extraction of α_s is indicated above in brackets (NLO: next-to-leading order; NNLO: next-to-next-to leading order; res. NNLO: NNLO matched with re-summed next-to-leading logs; N^3LO: next-to-NNLO) [22]. . . 6

1.3 Phase diagram of QCD [29]. 8

1.4 Heavy ion collision. Left: the two heavy-ions before the collision with the impact parameter b defined as the distance between the two centers of the nuclei. Right: the overlap region contain the participant nucleons, while the spectator nucleons remain unaffected. Source [35]. 10

1.5 Evolution of a heavy-ion collision. Left hand side is without a QGP. Right hand side is the same evolution with quark-gluon degrees of freedom. Source [38]. 11

1.6 Collision at finite impact parameter creating an "almond-shaped" overlap region [39]. 12

1.7 Integrated elliptic flow (v_2) as a function of $\sqrt{s_{NN}}$ for different experiments. At 2.76 TeV the centrality class is 20-30%, and the other energies have similar centrality [36]. 13

1.8 Back-to-back high p_T hadrons as observed by STAR. In the pp and d-Au case a clear back-to-back structure can be observed. For the central AuAu the away-side at 180° is absent, indicating quenching of the parton interacting with the QGP [42]. 14

1.9 Quenching of a di-jet event in PbPb collisions at the CMS detector. The energy of the collimated "Jet 0" is more than double the energy of the away-side jet "Jet 1". The awayside jet is also less collimated, indicating energy loss to the medium. 14

1.10 The nuclear modification factor R_{AA} for pions, kaons, protons and charged particles, as a function of p_T as measured by the ALICE Collaboration. The two plots to the left use data with 0-5% collision centrality, while the plots to the right use data with 60-80% collision centrality [43]. 15
1.11 Enhancement of strange particles, ϕ, Λ, Ξ, and Ω in PbPb measured by ALICE along with a ϕ measurement in Au-Au measured by STAR. The two most central ϕ enhancement values for Au-Au collisions are for overlapping centrality intervals (0-5% and 0-10%) [46]. 16
1.12 Centrality dependent J/Ψ suppression in PbPb collisions as measured by the ATLAS collaboration [47]. Left: relative J/Ψ yield as a function of centrality (1-Centrality translates to 100% = fully central collisions), normalized to the most peripheral bin. The expected relative yields from the (normalized) number of binary collisions (R_{coll}) are also shown. Right: normalized yield (relative yield divided by expected yield), as a function of centrality. 17
1.13 Electrons from charm and bottom semi leptonic hadron decay [73]. Bottom is defined as the sum of $b \to e$ and $b \to c \to e$. The aim of this thesis is to extend the bottom electron spectrum to higher p_T using a new technique, new data and different sub-detectors. It will serve as a basis for a PbPb measurement. 21

2.1 The ALICE experiment using the former L3 Magnet, at the LHC Point 2. 26
2.2 Electron microscope photograph of a solder bump on the readout chip as used for the ALICE SPD. The bump diameter is about 25 microns and must be applied with extreme precision for the connection between readout and detector to function properly. Source: VTT, Finland. . . 29
2.3 ITS SPD, schematic drawings of individual components. Source: ALICE ITS. 30
2.4 Schematic of an SDD. An incident particle (here photon) creates drift electron/holes that will drift in a potential. This allows for a 2D position measurement. Source: ESA 2011. 31
2.5 Schematic of the working principle of a time projection chamber. An incident particle ionizes charge along its path. The charge will drift due to the potential field. The electrons will then be counted after amplification at the anode. Source lctpc.org. 33
2.6 The ALICE TPC. 36
2.7 Integrated luminosities delivered 2011 by the LHC to the different experiments. The ALICE integrated luminosity is very low, shown in red close to the x-axis. 37
2.8 TPC energy loss versus momentum for 7 TeV pp collisions. Ideal lines fitted to data using equation 2.1 have been added for electrons, pions, kaons and protons. Source: ALICE repository. 39

2.9 TPC r-ϕ-resolution versus drift length for the TPC test module [95]. In order to compare these numbers with the full size TPC simulations they have to be extrapolated to 250 cm. 40

2.10 TPC z-resolution versus drift length for the TPC test module [95]. In order to compare these numbers with the full size TPC simulations they have to be extrapolated to 250 cm. 40

2.11 ITS-TPC combined track momentum resolution versus transverse momentum. Source: ALICE repository. 41

3.1 The ALICE EMCal 49

3.2 The EMCal energy resolution as a function of energy. A simulation is shown as the red dashed curve and measured data points are shown in blue. The black curve is a fit to the data. 51

3.3 The combined TPC + EMCal energy resolution as a function of p_T of electrons. A simulation is shown as black data points and the measured data are shown in blue. The resulting curves are a combination (shown in red) of the underlying energy resolutions of the TPC (green) and the EMCal (magenta). 51

3.4 The ALICE EMCal mini-module (EMC) at the SPS test beam setup. The beam enters from the left and Mx are magnets for the beam line, Sx are x-y detectors and CE is the Cherenkov detector to purify the beam. The black rectangle behind the mini-module is absorber for the muon detector (MU) in the back. 53

3.5 The EMCal mini-module. The top row of illustrations are, from left, right side view, top view and left side view. The bottom illustration is the top view, where the gradual leaning of towers as a function of η can be seen. 53

3.6 Left: The V1 clusterizer adds the four closest neighbors for each cell in the cluster. In this event the V1 clusterizer will sum all the active towers, forming one cluster. Right: 3×3 clusterizer. It adds the closest 8 cells surrounding the most energetic cell to form a 3 by 3 cluster. 58

3.7 This shows a 2D plot of high and low channel signals for two towers in the test beam mini-module. The blue H/L ratio of tower (0,5) is a normal tower with a linear relationship between the low gain and high gain channel. The red H/L ratio of tower (6,2) shows some non-linearity at low ADC counts on the high-gain channel. This tower was excluded. 59

3.8 Calibration factors, along with associated error for solving for the 64 calibration constants without removing edge clusters. Note that two towers are excluded, i.e. the calibration constant is set to 0 (tower 6 and 50). 62

3.9 The non-linear response of the mini-module. The data points correspond to the measurement using two different clusterizers, v1 and 3×3. As expected at higher energies the 3×3 clusterizer will on average lose more energy than the v1 (due to increased spread of showers). 64
3.10 This shows R_p for electrons and hadrons at different momenta. Electrons in black, hadrons in blue. The inset contains the same figure but with a logarithmic vertical axis. 67
3.11 This figure shows a cluster in the mini-module generated by an electron. An ellipse is fitted and the two axes are labeled M02 and M20. 68
3.12 This shows the M02 (Right) and the M20 (Left) parameter for electrons and hadrons at different momenta. Electrons in black, hadrons in blue. Inlays show parameters in logarithmic y-axis. 69
3.13 The containment parameter for electron and hadron showers for different momenta. 70
3.14 This figure shows the cluster energy (ratio) distribution as a function of distance from the center of the cluster for electrons. This data were obtained from 5 GeV electrons incident on the EMCal mini-module. The red band is the mean. 70
3.15 This figure shows the cluster energy (ratio) distribution as a function of distance from the center of the cluster for hadrons. This data were obtained from 5 GeV pions incident on the EMCal mini-module. The red band is the mean. 71
3.16 The K-factor parameter for electron and hadron showers for different momenta. 71
3.17 This shows E/p for electrons and hadrons at different momentum. Electrons in black, hadrons in blue. In the electron sample there is considerable contamination thus one has to use E/p to actually distinguish an electron from a hadron; the electron peak has been sampled only between 0.8 and 1.1 E/p. This is the definition of an electron in the mini-module study. 73
3.18 This shows ξ for electrons and hadrons at different momenta. Electrons in black, hadrons in blue. 74
3.19 Rejection factor for the different shower shape parameters. Inlay shows the shower shape parameters with close to unity rejection. The x-axis is logarithmic. Clearly the E/p parameter is a very efficient discriminator between electrons and hadrons. The ξ is exploiting information about momentum to reach a rejection which is essentially E/p with an added component of shower shape information. 76

4.1 The z-position distribution of the reconstructed vertex for LHC11d 7 TeV 2011 proton-proton collisions before event selection cuts. 80
4.2 The $x-y$-position distribution of the reconstructed vertex for LHC11d 7 TeV 2011 proton-proton collisions before event selection cuts. . . . 81

4.3 ITS SPD: tracks with hits in both layers. Left: tracks per event with $p_T > 1.0$ GeV/c. Red lines indicate EMCal 2010 ϕ-coverage, green lines indicate 2011 ϕ-coverage. Right: ITS ϕ-η hit-map for tracks with $p_T > 1.0$ GeV/c. The blue box indicates 2010 EMCal ϕ-η coverage. . 85
4.4 ITS SPD: tracks with hits in both layers. Left: tracks per event with $p_T > 1.0$ GeV/c. Red lines indicate EMCal 2010 ϕ-coverage, green lines indicate 2011 ϕ-coverage. Right: ITS ϕ-η hit-map for tracks with $p_T > 1.0$ GeV/c. The blue box indicates 2011 EMCal ϕ-η coverage. . 85
4.5 ITS SPD: tracks with hits in either SPD layer, with a total of 4 ITS hits. Left: tracks per event with $p_T > 1.0$. Green lines indicate EMCal 2011 ϕ-coverage. Right: ITS ϕ-η hit-map for tracks with $p_T > 1.0$. The blue box indicates 2011 EMCal ϕ-η coverage. 85
4.6 TPC number of clusters for all electron tracks with p_T greater than 2 GeV/c. The real data are shown in blue and simulations in red. The simulations do not describe data well for this parameter. 87
4.7 Left: TPC dE/dx parameter as a function of track momentum for the "good" run 159582. Right: The respective TPC dE/dx for a "bad" run, in this case run 157560. Note the lower average dE/dx for the tracks. This is probably due to several regions in the TPC having low/no gain for this particular run. 88
4.8 Tracking efficiencies for electrons and pions with the track cuts listed in Table 4.3. This is in real p_T space, i.e. unfolded p_T. 90
4.9 Tracking efficiencies for electrons and pions using the track cuts listed in Table 4.3 using reconstructed p_T over real p_T, i.e. smeared tracking efficiency. 90
4.10 Left: reconstructed versus MC p_T (GeV/c) for electrons. The deviation from linear behavior is due to bremsstrahlung effects. Right: reconstructed versus MC p_T (GeV/c) for pions. 92
4.11 Toy model test of unfolding algorithm using simulated electron spectrum. The green histogram are the measured data points. This spectrum is then unfolded to yield the blue data points, the unfolded spectrum. This should coincide with the original red MC spectrum. The unfolding matrix is constructed from these data, thus per definition the unfolded spectrum must coincide with the original spectrum. The agreement is exact. 92
4.12 Distribution of the residuals for the EMCal clusters to track matching in pseudo-rapidity ($\eta_{cluster} - \eta_{track}$) vs. azimuth ($\eta_{cluster} - \eta_{track}$) in proton-proton collisions at $\sqrt{s} = 7$ TeV triggered by the EMCal. Only clusters with an energy $E_{cluster} > 1$ GeV and tracks with a transverse momentum $p_{T,track} > 1$ GeV/c are used. 95
4.13 E/p for (a) electrons and (b) hadrons in simulation and 7 TeV proton-proton data, matched track p_T of 2.5-3.0 GeV/c. Rough particle selection is done with TPC nσ. 96
4.14 Hits in the EMCal during run 158285. Masked out towers can clearly be seen. 97

4.15 The hit rate in the EMCal for run 158285. Masked out towers are put to zero, or they would have orders of magnitude larger hit-rate. . . . 97

4.16 E/p for electron candidates in 7 TeV proton-proton data, $7 < p_T < 8$ GeV/c tracks. Basic track selection is done with TPC nσ. 98

4.17 Left: nσ distribution for all tracks along with Gaussian fits to the different particle species peaks. Red is for "other hadrons", gray is for pions and blue is for electrons. Right: nσ distribution for all tracks with the EMCal E/p cut applied. 99

4.18 The nσ distribution as a function of p. Solid curves are ideal fits of particle species, taken from AliROOT (TSplines function). Data points are fitted Gaussian functions to the various particle species peaks in nσ space. 100

4.19 PID purity and efficiency as estimated from data. The red lines are fit to the curves and used in the correction step. 101

4.20 Data-driven E/p method to estimate the purity of an electron sample. The red line are pure hadrons (mostly pions) that have been randomly matched to clusters. This is the dominant reason for the background structure at lower E/p. By scaling the hadron background to fit the lower E/p region an accurate purity can be obtained. 103

4.21 The L0 trigger patch sliding a 4×4 tower window over a real electron shower event in the EMCal test module. It moves by 2 towers each slide and integrates everything within the window to deliver a trigger decision on ADC level. 105

4.22 Trigger efficiency for LHC11a. Trigger threshold was set at about 3 GeV. Black data points are EMCal-L0 trigger efficiency for EMCal clusters calculated via simulation. Red points are a comparison using real data. 106

4.23 All clusters for MB and HT triggered events, normalized by number of events. 107

4.24 Ratio of all clusters for MB and HT triggered events, normalized by number of events, for the 7 TeV data-set, along with a line-fit at high p_T. 108

5.1 The $M_{K-e^{\pm}}$-distribution in a MC simulation, enhanced with electrons from heavy flavor decays. 115

5.2 Raw b-tags using the 90% pure cuts on the electron candidate sample. The trigger turn-on has been included, and can be seen in the lower amount of b-tags at low p_T. 117

5.3 Efficiencies as a function of p_T (GeV/c) of the b-tag algorithm on different particles using the 90% pure cuts listed in Table 5.2. The b/c tagging efficiency is obtained from a b/c enhanced simulation, and the π^0 and η efficiencies from a π^0/η enhanced simulation. 120

5.4 E/p for b-tagged sample (mainly electrons) and the corresponding "b-tagged" hadronic background (mainly pions) by b-tagging on tracks from pions. The hadronic background is scaled to fit E/p in the region of about 0.6-0.8. 124
5.5 Electron vs hadron purity of b-tagged sample as a function of p_T. . . 124

6.1 The blue band indicates the tracking efficiency plus response matrix combined systematic error. 128
6.2 Systematic error of tracking+response-matrix and unfolding algorithm. 128
6.3 PID cuts in E/p and nσ used to determine the systematic error of the PID step. The middle window along with red and blue lines indicate normal cuts. 130
6.4 The blue band indicates the PID systematic error. 130
6.5 Systematic error of PID and trigger correction. 131
6.6 Systematic error when sDCA is varied. 132
6.7 Systematic error when pDCA is varied. 133
6.8 Systematic error when M_{inv} is varied. 133
6.9 Systematic error when p_T^{hadron} is varied. 133

7.1 Non-charm-subtracted cross section of b-electron production in 7 TeV pp collisions, along with estimated charm background component. The charm background is obtained from a charm electron cross-section FONLL calculation, multiplied by the factor ϵ_c/ϵ_b, see Section 5. . . . 136
7.2 Cross section measurement of b-electrons for high p_T in pp collisions at 7 TeV. 137
7.3 Bottom electron production cross section compared to FONLL[49]. The data points are divided by the FONLL prediction. Dashed lines are the corresponding FONLL prediction uncertainty. The boxes are the calculated systematic error and the vertical lines correspond to the statistical error. 138
7.4 ALICE low and high p_T measurements of b-electron cross section. . . 139
7.5 ALICE low p_T bottom electron cross section as measured using an impact parameter method, following the methodology in the published low p_T bottom electron cross section [73] measurement. The data are from 2010 2.76 TeV PbPb collisions, in the 0-20% centrality bin[128]. 140
7.6 ALICE low p_T bottom electron R_{AA}. Source: ALICE repository. . . . 140
7.7 ALICE bottom electron R_{pPb} as a function of p_T, as measured from the pPb run at the LHC in 2013. Source: ALICE repository. 141

List of Tables

1.1 Approximate parameters of the QGP expected at the three different generations of HI accelerators [34]. 9

2.1 Dimension of the ITS detector layers as initially designed [82]. 32
2.2 ITS Precisions and resolutions 32
2.3 ALICE TPC parameters, [90]. 35

3.1 The EMCal physical parameters 52
3.2 Mini-module physical parameters 54

4.1 Summary of all cuts used in the electron level analysis. 78
4.2 Event criteria set on Global Quality = 1 events. 80
4.3 Summary of all track cuts used in the electron level analysis. 89
4.4 Summary of all PID cuts used in the electron level analysis. 104

5.1 ALICE track cuts used for selecting hadron tracks to pair with the electron. 112
5.2 Values of the different parameters for the different cut sets. 117

6.1 Values of the tracking parameters for different sets of cuts. 127
6.2 Algorithms and parameters used to estimate the systematic error associated with the unfolding algorithm. 129
6.3 The sets of cuts used to estimate the PID systematic error. 130
6.4 Algorithms and parameters used to estimate the systematic error associated with the unfolding algorithm. 132
6.5 Summary of estimated systematic errors for the different correction steps. 134

In token of appreciation
this work is dedicated
to my family

Acknowledgments

"An nescis, mi fili, quantilla prudentia mundus regatur?"

— *A. Oxenstierna*

First of all I would like to thank my wife, Anne. You are the most important person in my life. Thank you for always being there for me, for helping in any way you can, for taking on problems with a smile and for being my best friend. Things certainly do not always end up as one planned, but the journey is what counts and really makes life exciting. From picking you up in Tokyo to getting married in Sweden, from moving to the US and back to Europe, then moving to France, back to Sweden and finally ending up in Switzerland is one hell of a journey indeed. I would not want to do it with anyone else than you.

Thanks to my parents who raised me with lots of love and for always being there to support and assist in any way possible. Thanks to my three sisters, Sara, Eva and Mariah, for everything you did for me and for who you are. From saving my life (literally multiple times) to dealing with the scratching sounds of Lego pieces early in the morning. A big thanks also to my parents-, brothers- and sisters-in-law; my new family that I gained through Anne.

I had an interest in physics since I was very young and I would like to thank all my teachers that I had during my time as a student. Special thanks to Ulf Hennig who taught me mathematics (delen genom hela!), to Björn Jonson who introduced

and taught me nuclear physics, to Mats Lindroos and Fredrik Wenander for being great supervisors. All of you are outstanding people with a special ability to teach and inspire.

Thanks to all my friends that are so close to me: Rickard, Carl, Ante, David and everyone else. Thanks Kinga, Susie and Andrew for being the best study partners ever. Thanks to Flavius and Simone for all those good times, for so much ice cream, bad food and even worse coffee. Some people write diaries, but instead, I took thousands of pictures while in New Haven. You are in most of them! Thanks also to Randy, Tarek and Lucas. You guys are the best musicians I ever had the pleasure to write and play music with. I'll never forget all the jam sessions we had and the way we made music; total confusion! *For Whom the Bell Tolls* in E-flat still echoes in my mind. Thanks to Cecile and Philip, whom I met and got to know in New Haven, for all the wonderful years at 123 Mansfield. Thanks to Chitra and Anil who we got to know very well during my time at CERN. It is rare to meet such a genuinely kind and interesting couple. Also thanks to Göran for teaching me a whole lot about "Bräcke", helping me get through my thesis writing.

I also would like to thank everyone that explicitly helped me on my thesis, the RHIG at Yale, and most notably Ben who was my wingman and partner in crime. Looks like we made it! I remember when we started with the compilation of ROOT, to figuring out the EMCal test-beam data, moving to St Genis for a while, having all those presentations and to finally get the code running and getting some "results". I'll never forget the snow storm which ended in both of us digging out the car with our bare hands at 3 am in the worst October snow storm that hit the East Coast in a decade. I certainly hope they found the other car that we drove straight into a big pile of snow! I'll also never forget the boiled rat, marina mayhem and the alice fish at the end of presentations; it never really got old.

Thanks to Shingo Sakai for helping me to guide my research through the bureau-

cratics and politics of the ALICE collaboration: いつもお世話になり、ありがとうございました。 Thanks to Andrea Dainese who took time to read and understand the physics and methodology in my thesis, for asking relevant questions and for successfully convincing the collaboration that b-tagging is important. Thanks to Mateusz Ploskon and Constantin Loizides for sending us out on wild goose hunts regarding figuring out the EMCal and the associated data. One sure learned how to be selective in choosing what task to complete and what to ignore! In all seriousness, the data analysis framework would never had worked out they way it did if it weren't for your constant help and assistance despite busy schedules and lack of time. Thanks to Manuel Calderón for reading my thesis and for giving me detailed, relevant and useful comments. Also thanks to the thesis committee members for reading my dissertation and for asking me interesting questions at the defense.

Last but certainly not least: Thanks to John Harris and Helen Caines; it was a privilege to work with you, an adventure and experience that I will never forget.

Chapter 1

Introduction

The theorized de-confined state of quarks and gluons, the Quark Gluon Plasma (QGP), is thought to have occurred in the very early stage of the Big Bang[1]. This hot and dense state was the prequel to what is left today, evolving by expansion and cooling where quarks eventually became confined to form the basis of our universe. The Standard Model is the current theory of elementary particles and their interactions. The strong force described by quantum chromodynamics (QCD) dictates the interaction between quarks and gluons. It is within this regime that heavy-ion collisions are used to understand the relation between the laws of elementary particle physics and collective phenomena. The search for this de-confined state was initiated experimentally at the SPS at CERN and at the AGS at BNL in the 80s. RHIC at BNL continued this search and has presented convincing results indicating the formation of the QGP [2],[3],[4],[5]. The investigation continues at the LHC where several experiments aim to probe this state of matter. The goal of this thesis is to find a method to measure one of the signatures of the QGP, namely in-medium energy loss for heavy quarks. In this thesis a method to measure bottom production through semi-leptonic decay of bottom to electrons in pp collisions is presented, which serves as a comparison baseline for R_{AA} measurements in heavy-ion collisions.

An overview of the relevant physics is described in Chapter 1, along with current measurements and motivation for this study. In Chapter 2 the experimental apparatus is described, from the LHC to the ALICE detector along with the specific sub-detectors used in this thesis. Chapter 3 describes electromagnetic calorimeters in general, and also the ALICE electromagnetic calorimeter (EMCal). Significant time and effort from the Yale group has been invested in the building and commissioning of this detector and it forms the main detector for the measurements within this thesis. Chapter 4 describes electron identification. In Chapter 5 the selection and tagging of

electrons from semi-leptonic bottom decay is presented, along with the actual algorithm, performance of the algorithm and how background was subtracted. In Chapter 6 systematic errors associated with the different components of the measurement are discussed and calculated. Finally in Chapter 7 the results are presented, along with a conclusion and outlook.

1.1 The Standard Model

The Standard Model is the framework of the current theoretical description of fundamental particles and their interactions. It describes fundamental interactions through three distinct forces[1] that distinguish themselves by different strengths and ranges of interaction [6],[7]. As a comparison the strong force, being the strongest, has a short range of about 10^{-15}m. The electromagnetic force has an infinite range and a relative strength governed by the fine structure constant. The weak force has a range of about 10^{-18}m. The fourth and final force is gravity which has an infinite range but a weak interaction, thought to be mediated via the graviton[2].

The Standard Model is formulated through quantum field theories and contains the theory of the strong interaction (QCD) and the combined forces of the electromagnetic and weak interactions in a single electroweak theory. It has significant predictive power and has been verified by numerous experiments since it was first conceived in the 60's and 70's, the most notable ones being the prediction of Z^0 and $W^{\pm}$ bosons, quark flavors, various composite hadrons and precision measurements of parameters such as the anomalous magnetic dipole moment [8],[9],[10].

The Standard Model can be visualized through the fundamental particles, seen in Figure 1.1. The particles, or fields, come in different flavors and generations and can be split in two parts; the fields that make up matter and the fields that mediate forces. The matter fields are fermions with half-integer intrinsic spin and come in three generations. The first generation makes up most of the universe we see today; namely the u and d quarks that are the constituent particles of nucleons. Together with electrons they form the atoms around us. The second and third generations of quarks and leptons are more massive, identical to their lower energy counterparts if it were not for the mass difference. They quickly decay into the quarks and leptons of

[1]Fundamental interactions can be described through four forces, however the Standard Model currently only incorporates three of them; gravity is yet to be included.

[2]The interaction associated with gravity is very weak on the quantum level, making it impossible to observe the fundamental interaction with experimental equipment currently available. The graviton is thus not part of the current Standard Model

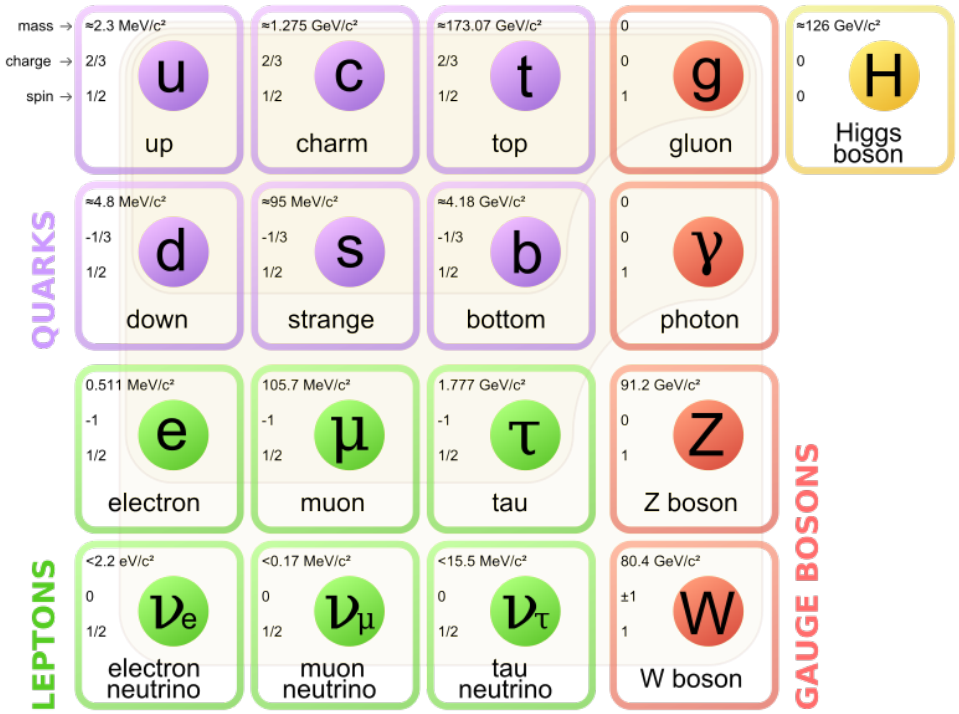

Figure 1.1: Elementary particles within the Standard Model. The three different generations are represented as the first three columns, with the mass increasing left to right. The last full column represent the gauge bosons. Finally, the Higgs boson (top right) has been "discovered", which adds to the success of the Standard Model.

the first generation. All particles interact via the weak force, (either through charged or neutral current processes) involving Z^0 and $W^{\pm}$ bosons. The electromagnetic force affects all particles with electric charge; both quarks and leptons. The strong force interacts only with colored particles, i.e. particles with color charge, which is a property found in the six different flavors of quarks.

The mediating particles, or gauge bosons, form the other category of fields having integer spin, they are responsible for all interactions. The massless photon acts on electric charge. The gluon acts on color charge and is massless, like the photon. It possesses color charge itself and this creates self-coupling of gluons which in turn leads to special properties of the strong force, such as an increasing coupling with increasing distance between particles with color charge. The Z^0 and $W^{\pm}$ bosons mediate the weak force which is responsible for processes such as radioactive decay and flavor change. It exhibits a behavior that lacks conservation of many properties, such as flavor conservation and other symmetries. The weak and electromagnetic forces have been shown to be a manifestation of a singular combined electroweak

force at sufficiently high energies.

Although describing the interactions between fundamental particles and it passed the test of many experimental measurements, the Standard Model is by no means a complete theory. It lacks in several aspects such as the small difference in abundance of matter and antimatter, and perhaps the most controversial, whether the fundamental interactions can be unified. As mentioned the unification of the electromagnetic and weak forces has been successful and this begs the question if the strong force also can be incorporated. This can perhaps be facilitated by Grand Unification Theories [11], but most of the physics involved is about 16 orders of magnitude higher in energy than what is accessible today. Most of these theories require the (slow) decay of the proton. No sign of proton decay has yet been observed[3]. Gravity would then be the next and perhaps final step to a grander unification, however there are many hurdles to cross before this can take place. Gravitation is currently best described by general relativity and the challenge is to formulate a (quantum) theory for gravitation that describes interactions on a small scale. The task of describing gravitation, which is mostly associated with large celestial bodies, on a very small quantum scale is yet unfinished [12],[13],[14].

The Standard Model is however the best current description of fundamental physics at small scales that we have, and on a recent note it just got updated with the discovery of the Higgs boson [15],[16]. The mechanism in which particles acquire mass can be explained by the Higgs field, which has for a long time been a fundamental problem with the Standard Model; why do particles have mass and how come some particles have a large mass (compared to lighter particles)? The discovery of the Higgs boson certainly adds credibility to the Standard Model. Symmetries, a hallmark of the Standard Model, are broken and the Higgs mechanism hints at how symmetry breaking can occur. There are still however many questions left to be answered.

Broken symmetries of the Standard Model, or symmetries in general, indicate that a model is not fully understood. Symmetries can in many cases produce very good predictions; with a simple model complicated systems can be approximated. However, the slightly-broken symmetries, i.e. cases where the model fails to deliver decent predictions, hints at a more fundamental theory. We have to settle for the fact that the Standard Model is an approximation of some more general and fundamental theory, and while the Standard Model works well for the (low) energies currently accessible for experimental physics (much like Newtonian mechanics is a low energy

[3]The current upper limit on proton lifetime is of the order of 10^{34} years, which is about 24 orders of magnitude larger than the age of the universe!

approximation of relativistic mechanics), it ultimately fails as a general fundamental theory of everything. The explanation of issues like masses of fundamental particles, renormalization, mixing angles, neutrino masses & oscillations, CP violation, matter/antimatter discrepancy, dark energy, dark matter, and everything else will hopefully be properly explained in a future theory of everything.

1.2 QCD

Quantum Chromo-Dynamics (QCD) [17] is the theory of color charge that describes the interplay between quarks and gluons. In the late 50s many new hadronic states were seen in detectors. This paved they way for the "Eightfold Way" that postulated the additional quantum number *strange*. This gave rise to theorized baryon nonets, decuplets, meson nonets etc, and these diagrams were subsequently populated with newly found hadrons. This vast particle zoo hinted that perhaps these particles were not fundamental but composed of even smaller particles, namely quarks. Three different quarks, u, d and s were postulated. These formed the first elements of the quark model. This gave rise to predictions such as the triple "sss" hadron, along with its theorized mass. The Ω^- was confirmed at BNL in 1964 [18] with a mass close to the predicted mass of a particle composed of three strange quarks. This posed another problem; the quarks are fermions and cannot possess the same quantum numbers without violating the Pauli principle. This led to the introduction of an additional quantum number labeled color, and three different colors were needed. The hypothesis of three quarks was later expanded and finally six different flavors of quarks were theorized. The experimental establishment of QCD has been accomplished through numerous experiments, a few of the most prominent being the "running" of the strong coupling constant α_s, substructure of nucleons [19] and quark-gluon jets where quark pairs head off in separate directions but one of them radiates a gluon causing a three-jet-event [20].

The QCD Lagrangian is responsible for describing all strong force processes:

$$\mathcal{L}_{\text{QCD}} = \bar{\psi}_i \left(i(\gamma^\mu D_\mu)_{ij} - m\,\delta_{ij} \right) \psi_j - \frac{1}{4} G^a_{\mu\nu} G^{\mu\nu}_a \tag{1.1}$$

where $\psi_i(x)$ is the quark field and

$$G^a_{\mu\nu} = \partial_\mu \mathcal{A}^a_\nu - \partial_\nu \mathcal{A}^a_\mu + g f^{abc} \mathcal{A}^b_\mu \mathcal{A}^c_\nu. \tag{1.2}$$

$\mathcal{A}^a_\mu(x)$ are the gluon fields and f_{abc} are the structure constants of SU(3). Three

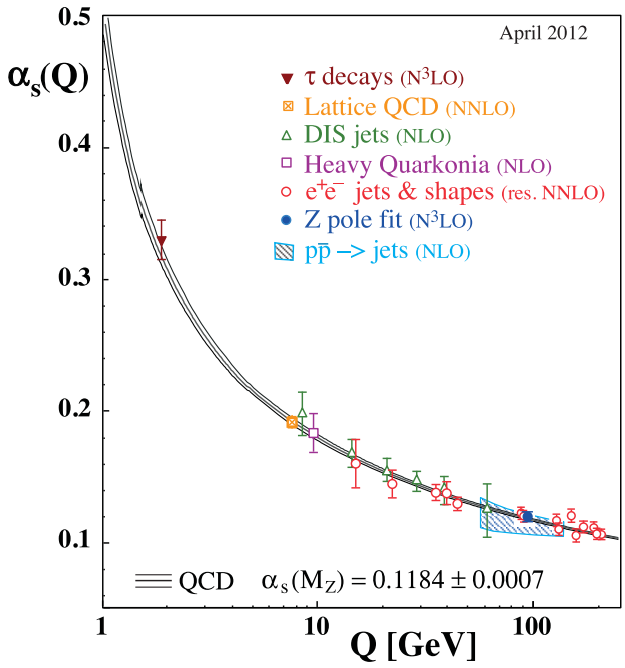

Figure 1.2: The strong coupling constant α_s as a function of the energy scale Q. The respective degree of QCD perturbation theory used in the extraction of α_s is indicated above in brackets (NLO: next-to-leading order; NNLO: next-to-next-to leading order; res. NNLO: NNLO matched with re-summed next-to-leading logs; N^3LO: next-to-NNLO) [22].

postulated colors hint that SU(3) should form the symmetry group of QCD, which indeed seems to be the case with 6 flavors of quarks each with 3 colors along with 8 gluons.

The fact that no free quarks are observed comes from the assumption that bound hadrons must be colorless to the outside, which means that any bound quark state is a *color singlet*. Color charge is a property much like electric charge in Quantum Electro-Dynamics (QED) but it differs in that the mediating boson for QCD, the gluon, also carries charge as opposed to the photon. QCD has a running coupling constant α_s meaning that its value depends on the scale, increasing in strength with increasing distance. The strong coupling constant can be seen in Figure 1.2,[21] [22].

This leads to two properties that characterize QCD:

- *Confinement* which states that quarks are bound together by the strong force in color singlets, i.e. color-less states.

- *Asymptotic freedom* means that at high energy, or small distances, quark and gluon interaction becomes smaller. Quarks and gluons can then be treated as free particles [23],[24].

The increasing coupling constant with large distance leads to a stronger force with larger separation, thus the energy of the system increases when trying to pull two quarks apart. At some point the energy is larger than the threshold of creating additional quark-antiquark pairs, which then form hadrons with the original quarks. This is the basic principle of confinement. Confinement has not been proven, however since free quarks have never been observed it generally appears to be true. Furthermore, in the high-energy limit one encounters asymptotic freedom since the coupling constant α_s decreases logarithmically at high energies, or small distances. At these high energies α_s can be written [25], to leading order, as

$$\alpha_s(Q^2) = \frac{4\pi}{(11 - 2/3n_f)\log Q^2/\Lambda^2_{QCD}} \tag{1.3}$$

where Q^2 is the momentum transfer for the process, n_f is the number of quark flavors and Λ_{QCD} is the momentum scale where non-perturbative effects become important (about 0.2-0.3 GeV [25]). Perturbative Quantum Chromo-Dynamics (pQCD) successfully describes the physics at high energies. At lower energies pQCD fails and other methods have to be used.

1.3 The QGP and heavy-ion collisions

When Q^2 is smaller than the scale Λ^2_{QCD} other methods than pQCD must be used. There are several different models for performing calculations in this regime, however the most successful one is *lattice QCD* [26]. Discrete points are used for placing quarks in a lattice where the fields are localized to the space-time point of the lattice. Gluons are fields between the quarks at the lattice points. Calculations are done numerically and are rather demanding, often requiring the use of large computer clusters or other super-computers to evaluate the model. The scale of the discrete points is changed and the model re-calculated and this continues until one can use a trend in the calculations to extrapolate to the continuum limit. Results show a coupling that increases with increased distance between quarks, which hints at the confinement property of QCD.

Another thing the model predicts is a phase transition at a certain energy. The transition can be observed by an increase in the energy density of the system [27]. Density and pressure increases as the temperature rises through the transition phase and the lattice calculations show that around about 180 MeV there is a transition between hadronic matter and a new phase labeled as the Quark Gluon Plasma (QGP).

This phase transition has been discussed long before lattice QCD, and the idea is that if one considers hadrons as single particles and add pressure and/or increase energy, at some point these objects will be as packed together as they can, reaching the high density limit of matter. However, hadrons are composite objects with a substructure and if one could further press them together, the quark fields from different hadrons will start to overlap. A quark close to other quarks from neighboring hadrons has no way to identify itself with the original hadron. The concept of the hadron as a particle will cease to exist and the quarks would be unbound or "free". The matter would then melt into a QGP which, as an electromagnetic plasma, consists of (color) charged objects that freely move around [28]. Figure 1.3 shows a phase diagram of QCD matter. The critical points and all the details of the phase diagram are not explicitly known, but the fundamental trends are quite clear. In light of this phase diagram the Standard Model also predicts that the QGP can exist in extreme pressure environments, such as within neutron stars or cores of supernovae. This makes the field of QGP an interesting and diverse topic.

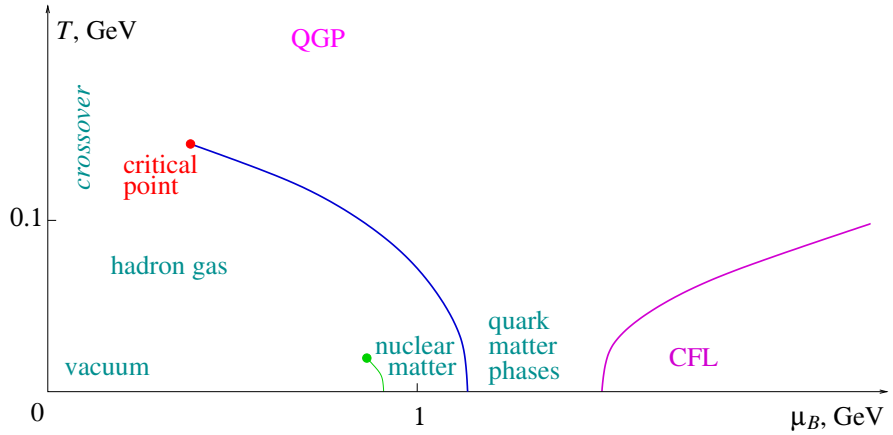

Figure 1.3: Phase diagram of QCD [29].

To create this state in laboratories one effectively injects sufficient energy over a large enough volume, leaving the quarks and gluons temporarily in a de-confined state. This is done with heavy-ion collisions where the nuclei of heavy elements are collided and studied. Heavy-ion collisions have been investigated at the alternating gradient synchrotron (AGS) at BNL and at higher energies ($\sqrt{s_{NN}}$ of about 17 GeV) at the SPS at CERN. Investigations at SPS experiments hinted at the formation of the QGP, a new state of matter [30],[31]. RHIC at BNL increased the energy to

Parameter		SPS	RHIC	LHC
$\sqrt{s_{NN}}$	[GeV]	17	130-200	2750-5500
dN_{gluons}/dy		∼450	∼1200	∼5000
dN_{ch}/dy		400	650	∼2000-3000
Initial temperature	[MeV]	200	350	>600
Energy density	[GeV/fm^3]	3	25	102
Life-time	[fm/c]	<2	2-4	>10

Table 1.1: Approximate parameters of the QGP expected at the three different generations of HI accelerators [34].

$\sqrt{s_{NN}} = 200$ GeV and since its completion in 2001 [32] several interesting properties of this state of matter, such as anisotropic flow and large energy loss of partons transversing the color-charged volume [33], were found. With the new era of the LHC the ALICE collaboration aims to further study this matter at an order of magnitude larger energy $\sqrt{s_{NN}} = 2.76$ TeV. See Table 1.1 for properties of three generations of the QGP studying accelerators.

Although fixed target experiments have been done, collider experiments are the dominant method since colliding two ions increases the available collision energy. The ions are first accelerated with a linear accelerator with stripping foils to remove electrons from the nuclei. The ions are then further accelerated in bunches within a circular accelerator containing two beams in opposite directions. The two beams cross over at certain collision points where collisions can occur and detectors are present. At the collision points the ions collide much like pp collisions, however since they are composed of hundreds of nucleons they are not point-like particles, so the geometry of the collision is of utmost importance for the event. A relative impact parameter b is introduced where b=0 corresponds to head-on *central* collisions and $b = 1$ means *peripheral* collisions barely touching, see Figure 1.4 where two nuclei are illustrated before and after collision. b is the vector that is formed between the centers of the two nuclei at collision, perpendicular to the beam-axis. The number of nucleons involved in the collision is dependent on the impact parameter, and so is the geometry of the formed overlap region and the QGP dependent on b.

In Figure 1.5 the evolution of a HI collision can be seen, with and without the QGP. The vertical y-axis is time and at $y = 0$ the two nuclei collide. The left side shows the collision without the formation of a QGP which has a color neutral pre-hadronic phase. The right side of the illustration includes the formation of a QGP with quark-gluon degrees of freedom. The QGP is theorized to be formed in the beginning of

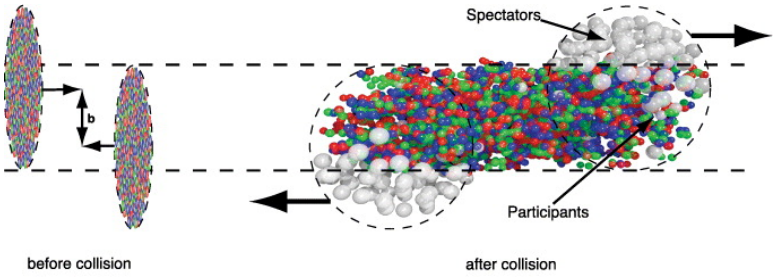

Figure 1.4: Heavy ion collision. Left: the two heavy-ions before the collision with the impact parameter b defined as the distance between the two centers of the nuclei. Right: the overlap region contain the participant nucleons, while the spectator nucleons remain unaffected. Source [35].

the collision, reaching thermal equilibrium quickly (within 1 fm/c) [36]. As the QGP expands and cools the system moves through the hadron-plasma phase transition [37]. A mixed phase may occur where the QGP and a hadron gas coexist, depending on the exact nature of this phase transition. After the system has transfered to a hadronic gas, chemical freeze-out occurs when chemical equilibrium cannot be maintained. Shortly after or simultaneously thermal freeze-out occurs where kinetic equilibrium is no longer maintained. The remaining final-state particles carry information about the evolution of the collision and are detected in the experimental apparatus to study the QGP.

1.4 Observables of the QGP

There are many observables associated to the QGP, however no single observable exists that will give the entire picture. Instead a combination of different measurements must be taken into consideration when determining the properties of the QGP. Here follows an explanation of the most common observables.

1.4.1 Collective Flow

The azimuthal distribution of momentum in a collision is commonly expanded in a Fourier series [37]:

$$E\frac{d^3N}{d^3p} = \frac{d^3N}{p_T d\phi dp_T dy}\sum_{n=0}^{\infty} 2v_n \cos n(\phi - \Phi_R) \tag{1.4}$$

where ϕ is the azimuthal angle of particles with respect to the orientation of the

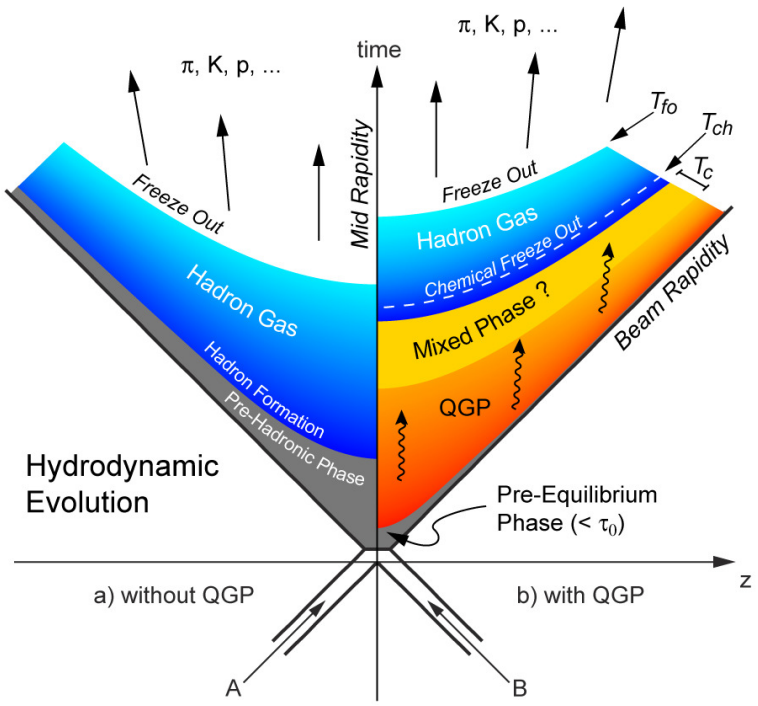

Figure 1.5: Evolution of a heavy-ion collision. Left hand side is without a QGP. Right hand side is the same evolution with quark-gluon degrees of freedom. Source [38].

reaction plane Φ_R. The reaction plane is the plane spanned by the z-axis and the impact parameter vector, see Figure 1.6. The coefficients v_n are used to parameterize the strength of any anisotropy in the azimuthal momentum distribution called *flow* components. v_1 indicates *directed flow* and v_2 indicates *elliptic* flow. *Flow* is used to describe a thermalized QGP that can be treated as a viscous fluid using hydrodynamical equations. The idea that high-energy collisions could be treated using relativistic fluid dynamics grew strong during the 70s when fixed target HI collisions were studied. In the RHIC era data agreed well with predictions from ideal fluid dynamics. It became clear that the hydrodynamic description should be limited to the QGP state of the collision, and for the hadronic state other models should be used.

Of particular interest are collisions in a peripheral collision geometry. It will create an overlap region with an azimuthally non-uniform geometry, see Figure 1.6, creating an azimuthally non-uniform QGP. When treated hydro-dynamically the anisotropic QGP will have pressure gradients that are non-uniform in the azimuthal plane. This causes a momentum boost in directions where the gradient is large. The pressure gradients are largest in the direction where the distance over which the pressure extends is shortest. This creates the elliptic flow in a peripheral collision geometry.

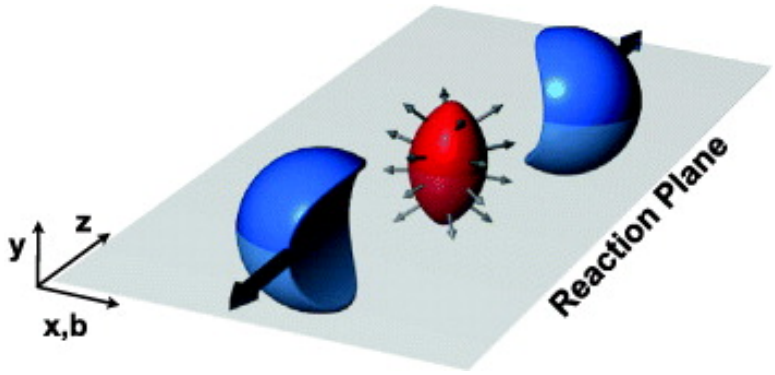

Figure 1.6: Collision at finite impact parameter creating an "almond-shaped" overlap region [39].

The elliptic flow, or v_2 parameter, for a centrality class of 20-30% can be seen in Figure 1.7 as measured by different experiments at different energies. For low collision energy the nuclear mean-field potential dominates, leading to a negative v_2, as nucleon-nucleon interactions are unavailable [40]. As collision energy is increased above 1 GeV/c, elliptic flow becomes positive. This indicates the formation of a state of matter that should be treated hydrodynamically. Elliptic flow is the most studied flow parameter, however higher order v_n terms, especially the odd-n components, can also hint at interesting flow physics [37].

1.4.2 Jet Tomography

In parton interactions where a large momentum transfer is involved hard scattering can occur which results in partons with large momentum that subsequently form a directed shower of lighter hadronic particles. These particles that are very close in phase space form what is called a *jet* and are the remnants of the original parton. Jet physics is a large field in itself since jet finding is no trivial undertaking. Several jet-finding algorithms exist and issues such as background, neutral components, etc. make it a complicated field of study.

Hard partons in a strongly-interacting QGP will lose energy through various QCD energy-loss mechanisms as they propagate through a colored medium [41]. This leads to *jet quenching* which can occur if the two partons that would form a back-to-back di-jet pair (with 180° azimuthal separation) traverse the QGP. This jet quenching is especially prominent in central collisions where the presence of a large QGP increases the chance for the partons to traverse the QGP. Specifically if the back-to-back partons are created at the periphery of the QGP, then one parton can escape the QGP forming

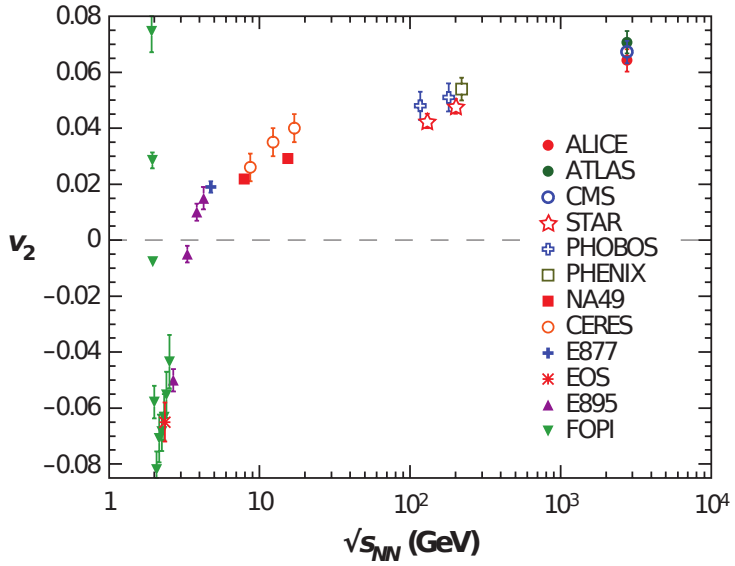

Figure 1.7: Integrated elliptic flow (v_2) as a function of $\sqrt{s_{NN}}$ for different experiments. At 2.76 TeV the centrality class is 20-30%, and the other energies have similar centrality [36].

a collimated jet while the other propagates through the QGP, losing much or most of the energy to the medium, removing any jet trace in exchange of an increased amount of soft hadrons. Experimentally this would mean that one of the jets would not be detected. This was one of the major successes of RHIC when two-particle azimuthal correlations were studied and the "away-side" peak vanished in central Au-Au collisions, see Figure 1.8. The same effect has been observed at the LHC in ALICE, ATLAS and CMS. A nice illustration of jet quenching can be seen in the event of Figure 1.9.

1.4.3 Nuclear Modification Factor

The nuclear modification factor, R_{AA} is defined as [37]:

$$R_{AA} = \frac{dN_{AA}/dp_T}{\langle N_{coll} \rangle \times dN_{pp}/dp_T}, \tag{1.5}$$

where dN_{AA}/dp_T is the differential invariant yield in nucleus-nucleus collisions and dN_{pp}/dp_T is the corresponding differential yield, or cross section, in pp collisions. $\langle N_{coll} \rangle$ is the average number of binary collisions in a given centrality range. Empirical models are used to calculate $\langle N_{coll} \rangle$ where collision geometry and detector responses are used as input for the computation.

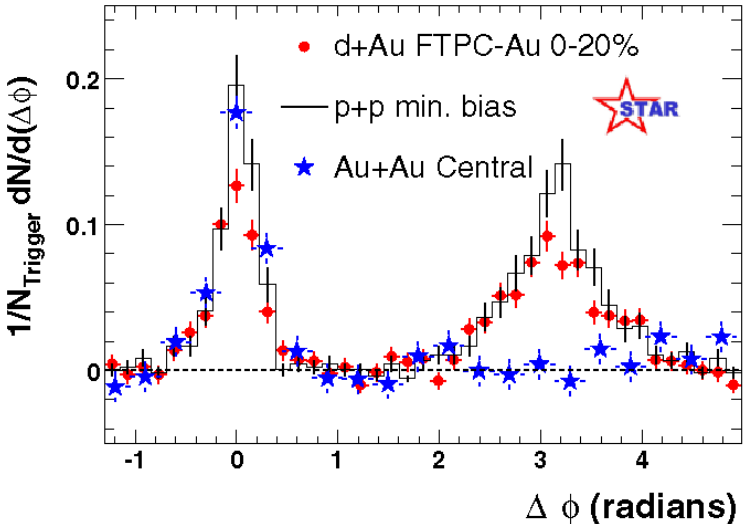

Figure 1.8: Back-to-back high p_T hadrons as observed by STAR. In the pp and d-Au case a clear back-to-back structure can be observed. For the central AuAu the away-side at 180° is absent, indicating quenching of the parton interacting with the QGP [42].

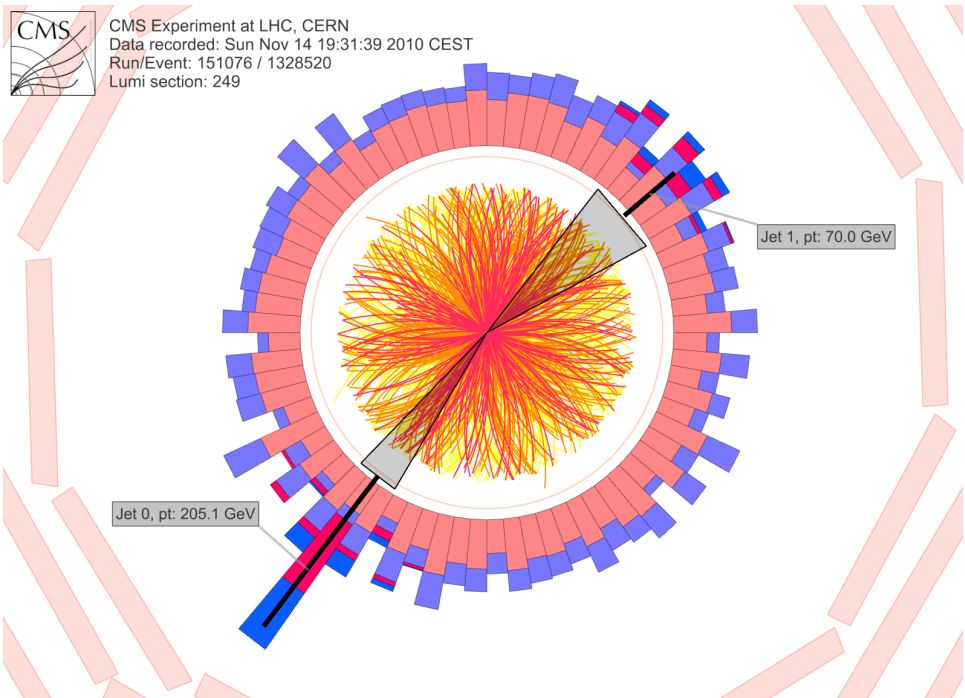

Figure 1.9: Quenching of a di-jet event in PbPb collisions at the CMS detector. The energy of the collimated "Jet 0" is more than double the energy of the away-side jet "Jet 1". The awayside jet is also less collimated, indicating energy loss to the medium.

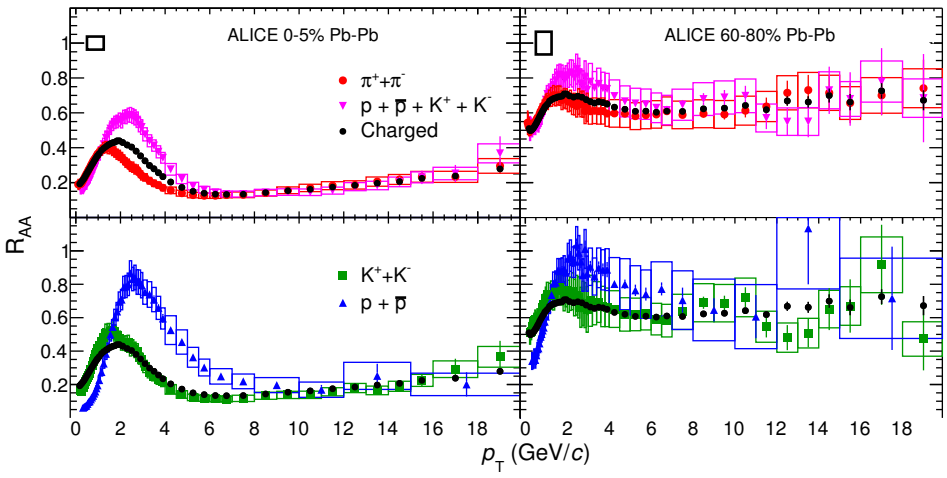

Figure 1.10: The nuclear modification factor R_{AA} for pions, kaons, protons and charged particles, as a function of p_T as measured by the ALICE Collaboration. The two plots to the left use data with 0-5% collision centrality, while the plots to the right use data with 60-80% collision centrality [43].

In HI collisions high-p_T particles are thought to mainly arise from initial hard scattering. If HI collisions are a superposition of equivalent number of nucleons colliding, then $R_{AA} = 1$, meaning that the number of high-p_T particles would coincide with the equivalent number obtained in pp collisions, scaled with number of binary collisions in the HI case. Jet quenching can also suppress the production of high-p_T hadrons and thus a non-unity R_{AA} would be expected for hadrons at high p_T. R_{AA} can be seen in Figure 1.10 for different particles as measured in PbPb collisions at ALICE. As expected, suppression is found at large transverse momentum. Also, R_{AA} is smaller in central events than in peripheral events due to the larger average suppression caused by the larger QGP in central collisions. This suppression has been found and measured both at RHIC and LHC.

1.4.4 Strangeness Enhancement

Production of the s quark is suppressed in ordinary matter due to the large mass of the s compared to the lighter u and d quark masses. If a QGP is formed de-confined quarks should revert to their *bare* mass [44] and the threshold for the creation of $s\bar{s}$ pairs would significantly decrease. In addition, due to the presence of many gluons, the cross section for production by gluon fusion increases significantly. This would then result in an increase in the number of s quarks, which eventually form hadrons with other quarks, increasing the strangeness of measured hadrons relative to the case

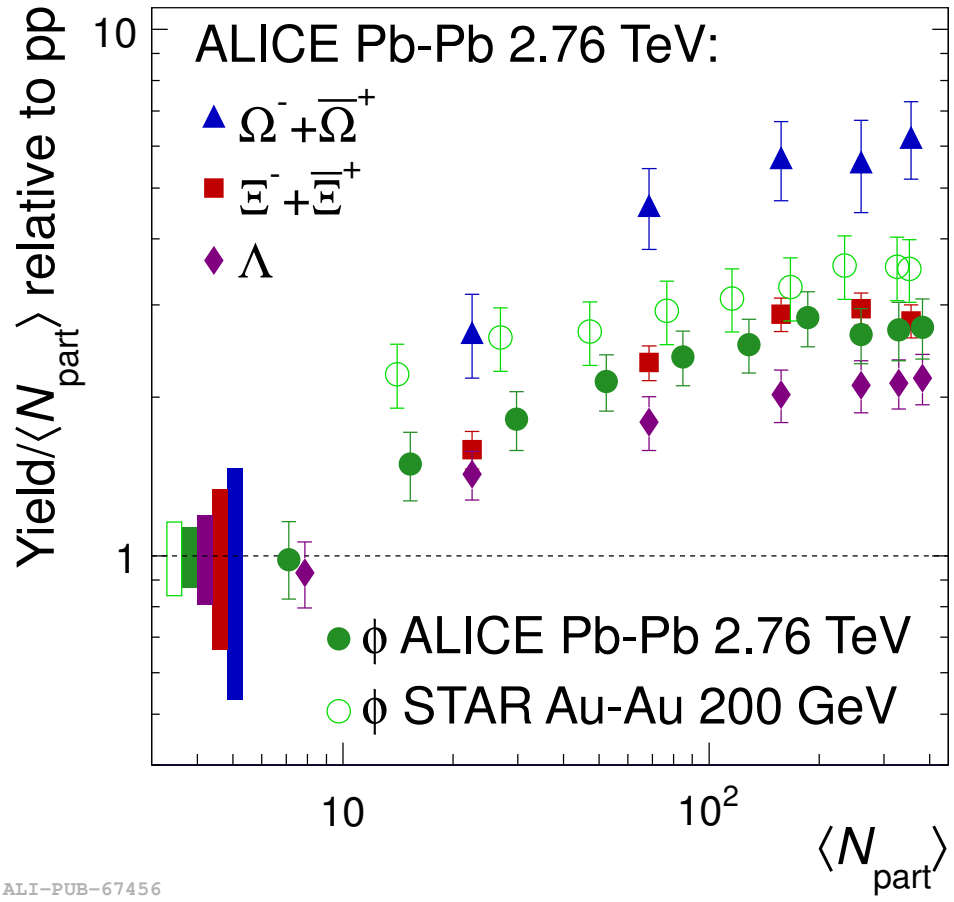

Figure 1.11: Enhancement of strange particles, ϕ, Λ, Ξ, and Ω in PbPb measured by ALICE along with a ϕ measurement in Au-Au measured by STAR. The two most central ϕ enhancement values for Au-Au collisions are for overlapping centrality intervals (0-5% and 0-10%) [46].

without a QGP. This enhancement was seen in the NA57 and WA97 measurements of strange hadrons [45], and also subsequently at both RHIC and the LHC [46]. A recent ALICE measurement, compared with STAR data, can be seen in Figure 1.11.

1.4.5 Quarkonia Suppression

At the high energy available in pp and AA collisions many quark-antiquark pairs will be produced and quarkonium states ($q\bar{q}$) can be formed. This is also true within a QGP. However, since the binding of quarkonia is of the order of a few hundred MeV, in an environment of other free quarks with high energy these bound states are very likely to break apart and ultimately form other more stable states. Thus, a QGP will suppress the yield of quarkonium states. For the J/Ψ particle which is composed of a

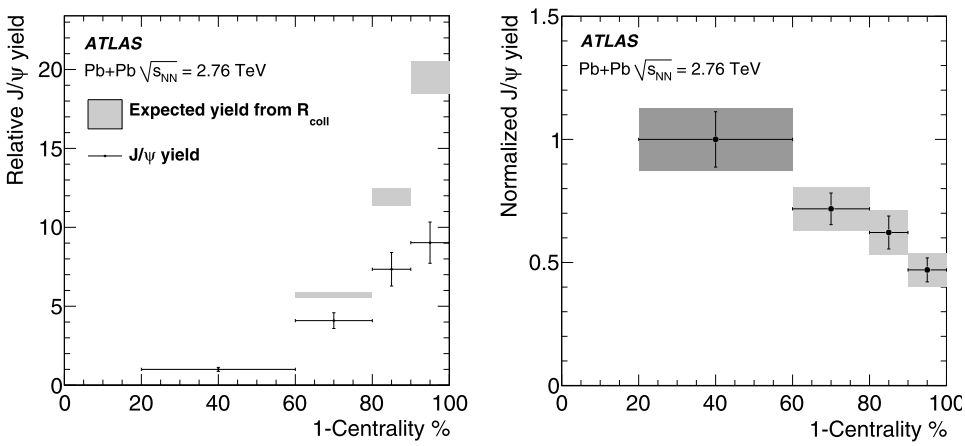

Figure 1.12: Centrality dependent J/Ψ suppression in PbPb collisions as measured by the ATLAS collaboration [47]. Left: relative J/Ψ yield as a function of centrality (1-Centrality translates to 100% = fully central collisions), normalized to the most peripheral bin. The expected relative yields from the (normalized) number of binary collisions (R_{coll}) are also shown. Right: normalized yield (relative yield divided by expected yield), as a function of centrality.

$c\bar{c}$ pair, the production is mainly through hard scattering in the initial collision, thus if the J/Ψ is suppressed it would indicate the formation of a QGP. J/Ψ suppression was observed at the SPS, RHIC and LHC. However, since suppression has also been observed in p-A and d-A collisions this indicates that other physics is at play [37]. Figure 1.12 shows suppression of J/Ψ as a function of centrality for PbPb collisions at the LHC as measured by ATLAS. Largest suppression is found for fully central collisions (here labeled as 1-Centrality), as expected due to the larger QGP. The suppression is not limited to J/Ψ, but to all quarkonia, thus further measurements may shed light on the physics involved in this suppression.

1.5 Heavy Flavor

Heavy-flavor hadrons, or more specifically open heavy-flavor hadrons, are particles that carry one charm or bottom quark in addition to lighter quarks. Since charm and bottom quarks are heavy ($m_c = 1.29^{+0.05}_{-0.11}$ and $m_b = 4.19^{+0.18}_{-0.06}$ GeV [48]) they are produced mainly through hard interactions in the beginning of a collision. This is in contrast with u, d and s quarks, which can be produced through thermal means if the average temperature is high enough. Since charm and bottom quarks are produced through hard scattering with large Q^2 they can be treated in pQCD. In fact, since heavy flavors are preferentially produced through hard processes even at

zero momentum, pQCD is a valid approach for all heavy flavor momenta. This is a unique feature and makes heavy flavor an excellent testing ground for pQCD. Since in-medium energy loss is expected to be dependent on mass [37], heavy flavor is also an excellent probe of the QGP.

The calculation of heavy flavor production in hadron collisions is treated in pQCD using QCD *factorization*, which applies to many hard processes within QCD. It allows the calculation to be separated into perturbative (calculable) and non-perturbative parts. The non-perturbative can be parameterized through parton distribution functions and fragmentation functions. The factorization is then divided into the following:

- The initial conditions are described via parton distribution functions, PDFs. These describe the non-perturbative initial conditions and are obtained from the fractional momenta the interacting partons have of the incoming hadron.

- The partonic scattering cross section which is calculated through pQCD.

- The fragmentation of heavy quarks into hadrons is described through fragmentation functions and are of non-perturbative nature. Heavy quarks can undergo fragmentation to open heavy flavor hadrons and bound quarkonium states. The latter is only 1-2% of total amount of all produced heavy flavor, but is in itself of great interest in heavy-ion physics.

To calculate the perturbative part there are different methods to choose from. The most common pure pQCD method is in "fixed order next-to-leading-log" re-summation models (FONNL) [49], where the cross section is calculated at fixed order with next-to-leading-log re-summation of higher orders in α_S.[4] Also MC generators like PYTHIA, HERWIG and HIJING [50],[51],[52],[53] can provide predictions for specific heavy flavor processes, but focus on general behavior of all observables. MC generators are of utmost importance in modern particle physics where measurements, such as detector efficiencies, are obtained almost exclusively from MC simulations. In this thesis PYTHIA was used for the calculation of various efficiencies, and FONLL was used as a final check at the invariant yield level.

[4]Leading order means gluon fusion and quark-antiquark annihilation contributions. Next to leading order means processes like gluon splitting or flavor excitation are taken into account

1.5.1 Previous measurements

Charm was discovered when the J/ψ was found in 1974, however the first heavy flavor measurements were done at CERN using the ISR collider at $\sqrt{s} = 52.7$ GeV [54] where single electrons from heavy flavor decays were observed but not explained. After the discovery of charmonium and other charmed hadrons it became clear where the single electrons came from. Bottom production at hadron colliders started in the late 1980s at the CERN Sp$\bar{\text{p}}$S, where muons plus jets and dimuon pairs were detected which resulted in the measurement of the bottom production cross section [55],[56]. A good agreement with pQCD models at the time was observed. The next step in heavy flavor measurements was the Tevatron at Fermilab where the proton-antiproton collider took collision energy to a new level. Studying mainly bottom production the full reconstruction of $B^{\pm} \rightarrow J/\psi K^{\pm}$ was measured for the first time. Later also B^0 mesons were measured through the $B^0 \rightarrow J/\psi K^*(892)$. Both CDF and D0 measured bottom production and both established that bottom was being produced over-abundantly compared to current pQCD calculations. A complicated puzzle had to be solved and more careful investigations of both pQCD calculations and experimental data led to the agreement of data and theory [37]. Also charm was studied and the fully reconstructed hadronic decays $D^0 \rightarrow K^-\pi^+, D^{*+} \rightarrow D^0\pi^+, D^+ \rightarrow K^-\pi^+\pi^+, D_s^+ \rightarrow \phi\pi^+$, along with their respective charge conjugates, were successfully measured.

With the advent of RHIC and heavy-ion colliders heavy-flavor measurements were increased when PHENIX and STAR measured heavy flavor in both pp and HI collisions. Fully reconstructed $D^0 \rightarrow K^-\pi^+, D^{*+} \rightarrow D^0\pi^+$ in pp collisions [57] and $D^0 \rightarrow K^-\pi^+$ in AuAu collisions [58] were measured by STAR. PHENIX measured charm and bottom production through electrons in pp and AuAu collisions [59], and through muons in pp and CuCu [60]. Non-photonic electrons were measured in pp and AuAu at STAR [61],[62]. Disentanglement of electrons from bottom and charm has also been done in both PHENIX and STAR for pp [63],[64] with limited precision. In general, heavy-flavor measurements at pp agree well with theory and pQCD is indeed a good theoretical tool for heavy-flavor production [37]. When it comes to heavy-ion collisions the current theoretical models, specifically regarding energy loss of heavy flavor and high p_T suppression, have not been entirely successful. The suppression of partons in a QGP medium, or quenching, comes from the strong interaction between partons and the medium. As quenching was observed for jets, heavy quarks are also expected to lose energy due to several processes. However, most models indicate that a heavy mass, such of charm and bottom quarks, will result in less suppression[65].

When RHIC measurements showed suppression of electrons from heavy flavor decays at mid- and high-p_T in central AuAu collisions it came as a surprise [66]. Separation of charm and bottom with increased accuracy is needed. The coming upgrades of PHENIX and STAR may shed light on this issue.

At the LHC the new energy frontier has opened up a new range of physics. The four experiments at LHC, ALICE, ATLAS, CMS and LHCb all measure heavy flavor and so far many measurements have already been published, and many more are in the making. In pp where there is abundant data CMS has performed full reconstruction of $B^{\pm}$, B^0 and B_s^0 [67],[68],[69], ATLAS has measured $B \to J/\psi$ in a wide range of p_T [70]. ALICE has measured D^0, D^+ and D^{*+} production along with heavy-flavor electron production and individual charm and bottom electron spectra [71],[72],[73]. Specifically, the charm and bottom electron spectra are extended to higher transverse momentum in this thesis, see Figure 1.13. In all pp measurements there is good agreement with pQCD. For the HI case, PbPb and pPb collisions have been measured. Many results are in progress and soon to be published. Mentioned here are just a few of many measurements, for a more comprehensive review see [37].

In this thesis bottom hadrons were selected in order to probe the theorized QGP created at the LHC. After hadronization the resulting bottom hadron decays and can be identified from other processes due to the long lifetime of the bottom hadron [48]. Bottom quarks and the corresponding bottom hadrons are abundantly formed in ALICE and the dominant decay mode is through the semi-leptonic decay $B \to eX$, with about 10%. In this thesis a method for measuring the production of electrons from bottom hadron decay is presented along with the differential production cross section of electrons from bottom through semi leptonic decay at $\sqrt{s} = 7$ TeV. The measurement serves as a test for pQCD calculations at the LHC, and also serves as a baseline for a future measurement of bottom electron production and possible suppression in PbPb collisions in the context of a QGP.

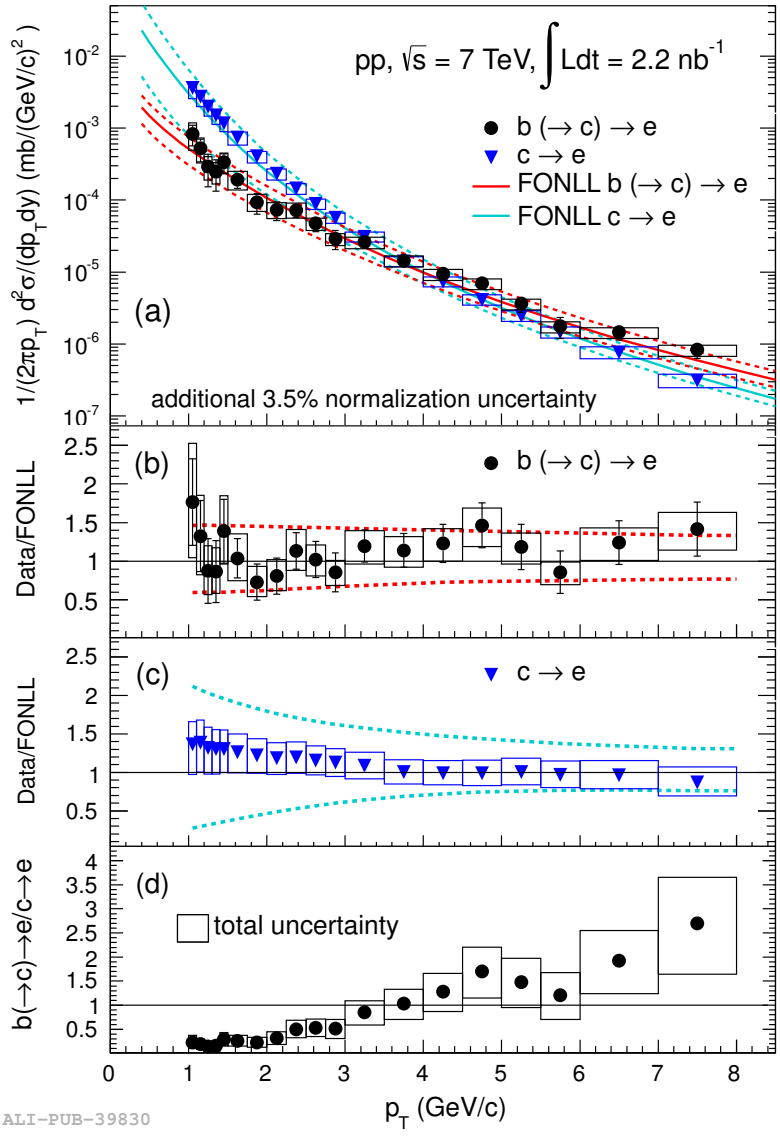

Figure 1.13: Electrons from charm and bottom semi leptonic hadron decay [73]. Bottom is defined as the sum of $b \to e$ and $b \to c \to e$. The aim of this thesis is to extend the bottom electron spectrum to higher p_T using a new technique, new data and different sub-detectors. It will serve as a basis for a PbPb measurement.

Chapter 2

The Experiment

In November 2009 the ALICE detector recorded the first collision in the LHC [74]. That moment marked the beginning of an era of new physics and new discoveries. In this chapter the experiment as a whole is described, starting with the LHC in section 2.1 followed by the ALICE experiment in section 2.2. Then the detectors used in the analysis are described in more detail; the ITS in section 2.2.2 and the TPC in section 2.2.3. The EMCal is briefly presented in section 2.2.4, and for an in-depth description see section 3.2. Finally the computing part of the analysis is briefly described in section 2.3.

2.1 LHC

Ever since their invention in the early 1930's, particle accelerators have played a fundamental role in physics. The first accelerators were direct-current accelerators such as the Van de Graaff accelerator, used to accelerate particles to an energy of a few hundred keV. With the advent of oscillating RF field accelerators the linear accelerators could increase the energy of the accelerated particles even higher, beyond one MeV. The cyclotron, along with the synchrotron, which are circular accelerators, pushed the energy barrier even further and soon size and cost would be the limiting factor when designing particle accelerators. The Large Hadron Collider is a superconducting hadron synchrotron collider and is the largest particle accelerator ever built (also the largest machine ever built by humans). The idea was conceived in 1994, and the original plan was to collide protons at 10 TeV, but since then many things have changed and it was subsequently designed to collide two proton beams each at 7 TeV for a total energy of $\sqrt{s} = 14$ TeV and two lead heavy-ion beams at 2.76 TeV for a total of $\sqrt{s_{NN}} = 5.5$ TeV. On 10 September 2008, protons were successfully

circulated in the main ring of the LHC for the first time. However, 9 days later a magnet quenched due to an electrical fault causing the LHC to shut down for a year due to checks and repairs. In November 2009 it was again started and produced the first proton-proton collisions at $\sqrt{s} = 900$ GeV [74]. $\sqrt{s} = 2.36$ TeV was reached shortly thereafter, breaking the previous record held at $\sqrt{s} = 1.96$ TeV by the Tevatron at Fermilab. In March 2010 the collision energy was further increased to $\sqrt{s} = 7$ TeV and collisions were delivered at this energy until October 2010. In November 2010 the LHC accelerated lead nuclei for the first time, initially at a planned energy of $\sqrt{s_{NN}} = 2.76$ TeV, which is half of the maximum intended design energy. This running procedure was repeated for 2011, i.e. $\sqrt{s} = 7$ TeV pp collisions throughout the year, and one month of PbPb collisions at $\sqrt{s} = 1.96$ TeV. In 2012 the LHC delivered proton-proton collisions at 8 TeV and pA (proton-lead) collisions at about $\sqrt{s_{NN}} = 5.2$ TeV, then shut down for an extended time period to perform upgrades and repairs. It will resume operations at full design energy early 2015.

The LHC is built in the old LEP tunnel at CERN, stretching 26.7 km in circumference below the border of France and Switzerland just outside the swiss city of Geneva. The LHC is a twin proton-beam synchrotron collider with two beams in the same tunnel. It features an octagonal-shaped ring with 8 straight sections and 8 arcs. The straight sections used to house large amounts of RF cavities for the LEP accelerator to accelerate electrons and positrons, due to the considerable amount of energy lost in Bremsstrahlung when accelerating electrons. Since the LHC accelerates hadrons and there is an inverse dependence on synchrotron radiation and mass ($1/m^2$), Bremsstrahlung loss is not as much of a problem for the LHC. Only one set of RF cavities is used and placed at one of the straight sections. Longer arcs would have been optimal, however, one of the main reasons for building the LHC in the old LEP tunnel was the cost-savings associated with re-using already present infrastructure. The old LEP tunnel features 8 crossing points, four of them are in use at the LHC where the four main detector experiments are built, ALICE, ATLAS, CMS and LHCb. ATLAS and CMS are multi-purpose detectors constructed for mainly proton-proton collisions at high luminosity for the study of elementary particle physics. LHCb is a dedicated bottom-physics experiment that studies CP violations associated with b-hadron interactions. The ALICE detector is a dedicated Heavy Ion (HI) experiment that aims to study HI collisions in order to peek at the conditions a fraction of a second after the Big Bang. The LHC will deliver AA or pA collisions for about one month per year.

2.2 ALICE

ALICE is an acronym formed from "A Large Ion Collider Experiment"[1]. The ALICE detector (Figure 2.1) is located at "point 2" of the LHC complex just north of the French village of Saint Genis-Pouilly at the French side of the Franco-Swiss border. The ALICE collaboration consists of more than 1000 physicists, engineers and technicians from over 30 different countries worldwide. It features many sub-detector systems tuned for heavy-ion physics with high multiplicity events. The prime goal of the experiment is to study the behavior of nuclear matter at high temperature and density.

The ALICE detector can be subdivided into several parts, the main parts being central full-azimuthal tracking detectors, calorimeters/Cherenkov detectors inside a solenoidal magnet and muon detectors placed 7 meters "behind" the interaction point after a dipole magnet.

2.2.1 Tracking in ALICE

Closest to the crossing point is the inner tracking system (ITS), which consists of six layers of silicon trackers. In conjunction with the Time-Projection Chamber (TPC) and the Transition Radiation Detector (TRD) the ITS forms the main tracking system of ALICE. The ALICE tracking system is considered a slow detector system, mainly limited by the drift time in the TPC, but what it lacks in speed it makes up by reliable performance at high charged-track multiplicity (up to 20,000 charged tracks per collision event). The TPC was chosen as the main tracker because of the need for large amounts of measurable space points. At smaller radii a silicon tracker is needed for increased vertex resolution.

Outside the tracking system are the Time of Flight (TOF), then the High Momentum Particle Identification (HMPID), the Photon Spectrometer (PHOS) and the Electromagnetic Calorimeter (EMCal), which are mainly used for particle identification. These detector subsystems are located in a 0.5 T magnet conveniently called the "solenoidal magnet", which is the magnet from the decommissioned L3 detector previously housed at the same location. A 0.5 T field was selected since it gives a good tracking resolution down to 0.1 GeV/c. A higher field would cause such low-momentum tracks to escape proper measurement due to the small radius of curvature of charged tracks. Additionally there are several trigger detectors, the main ones be-

[1]Following traditional naming conventions commonly employed within the physics community [75]

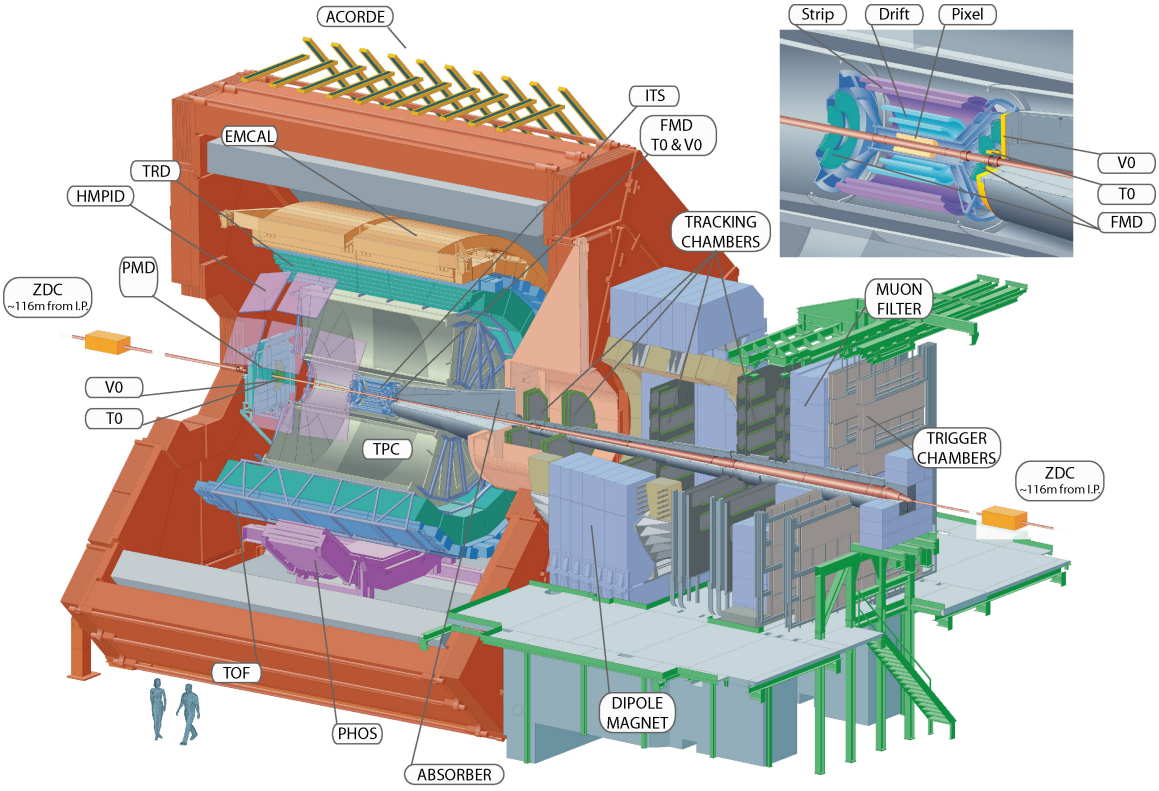

Figure 2.1: The ALICE experiment using the former L3 Magnet, at the LHC Point 2.

ing the V0 (Vertex centrality), T0 (Timing) and ZDC (Zero Degree Calorimeter) detectors. Finally the forward Muon spectrometer is situated after the absorber and dipole magnet and is mainly used for the study of quarkonia through muons [76].

For the analysis in this thesis the ITS, TPC and EMCal were used for tracking and particle identification. Following is a more in-depth explanation of these detectors that are relevant for the analysis within this thesis.

2.2.2 ITS

The main functions of the ITS are to locate the primary and secondary vertices, assist in the momentum resolution and tracking of the TPC, and provide basic particle identification of low momentum particles. A drawing of the ITS can be seen as an inlay to the top right corner in Figure 2.1, and the dimensions can be seen in Table 2.1. It consists of six layers of different semiconductor detectors, divided into three sub-detectors with two layers each of the SPD (Silicon Pixel Detector), SDD (Silicon Drift Detector) and the SSD (Silicon Strip Detector). The positioning and number of layers are optimized for track reconstruction and vertex resolution. The

choice of silicon technology is dependent on several factors, one of the most important being the average particle density, which becomes very high at small radii. Up to 90 tracks per cm^2 for the innermost radii and about one track per cm^2 for the outermost layers is expected, thus pixel detectors were selected for the two inner layers, silicon drift detectors as the two middle detectors, and micro-strip detectors for the two outermost layers. The four outermost layers (SDD & SSD) also have energy-loss readout capability in terms of energy loss per unit distance (dE/dx) that can be used for low-p_T particle identification below 100 MeV/c. The main function of the ITS is to provide accurate track reconstruction and identify the vertices. Most physics analyses depend on proper tracking and vertexing. Also since the ITS can provide energy-loss measurements, particle identification for the non-relativistic low-momentum part is provided by the ITS. Some of the first physics publications from ALICE were based on this information since the readout and analysis of the ITS is relatively straightforward [74].

Semiconductor detectors

Semiconductors have been developed at an unparalleled pace during the last few decades and have led to a wide range and widespread usage of semiconductor particle detectors. For a more detailed discussion, see [77],[78],[79]. The main benefits of using solid-state detectors are high-density spatial resolution, fast timing, good energy resolution and a standardized manufacturing process. As an example, excellent energy resolution can be achieved with semiconductor detectors; the statistical uncertainty of a particle-generated pulse is proportional to the number of charge carriers, which is related to the ionization energy required to create a charge-carrying-pair in the medium. Semiconductor detectors work conceptually like a gas-detector but instead of drifting ion-pairs, electron-hole-pairs are used as fundamental charge carriers. The ionization energy is around 30 eV for gas-detectors, but only a few eV for silicon detectors, giving a large advantage to silicon detectors in terms of signal resolution.

The working concept of a semiconductor detector is very basic. As usual in a semiconductor, impurities are introduced into a uniform crystal lattice of a semiconductor material. The semiconductor material most commonly used is silicon (thus "silicon detectors") and germanium. The introduced impurities have either one extra valence electron, or one missing, relative to the semiconductor material valence electrons. Without these impurities the semiconductor would have too large of a gap between the valence band and the conduction band for any conduction to occur. With the introduced impurities a number of donor electrons are formed just below the

conduction band (n-type semiconductor) or "holes" which are equivalent to mobile particles carrying positive charge just above the valence band (p-type semiconductor). An incident particle will then create electron/hole pairs that can drift in an applied electric field, thus creating a measurable signal. For all practical purposes, the ionization energy is constant with respect to incident particle type, particle energy and temperature of the semiconductor, however this can change in extreme circumstances [80].

SPD

Silicon pixel or silicon pad detectors are the densest semiconductor detector type. The design of pixel detectors is considered a "brute force" approach in the sense that each pixel is an individual detector and each needs a dedicated readout. With the rapid evolution of semiconductor technology, the pixels can be made very small, on the order of a few tenths of μm, yielding extremely dense detectors with incredible two-dimensional position resolution. Pixel detectors suffers from the drawback that each channel must be read out, either simultaneously, or in some pattern, giving rise to dense and complicated readout electronics. In most cases a read-out chip is directly attached to the silicon by the usage of solder beads, usually made from Indium, serving as conduction between silicon and the read-out chip, see Figure 2.2 where a solder bead is shown for the ALICE pixel detector assembly. This technique is difficult to master; a bad connection between detector and readout can result in dead pixels. It also has the disadvantage of adding extra material to the material budget of the detector which can distort sensitive measurements. Another technique is to integrate the readout electronics into the silicon detector, which is a complex, but not impossible undertaking. The advantages are a fast and reliable readout of the pixels and much less material, but the disadvantages are the integrated circuits' sensitivity to radiation damage and conflicts between the two different manufacturing processes of detectors (large active area and durable) versus integrated circuit silicon devices (small, compact and fragile) [81].

The two innermost ITS layers consist of silicon pixel detectors forming the SPD, as shown in Figure 2.3. It is crucial for minimizing the track resolution, in order to determine the primary vertex, the track impact parameter, and secondary vertices. The choice of detector type was limited by the pixel density needed for radii closest to the beam pipe, but there were also other factors such as speed of the detector and intense radiation close to the collision point. The SPD is a fast detector and can be operated at tens of kHz speeds. It is therefore used as a L0 and L1 trigger

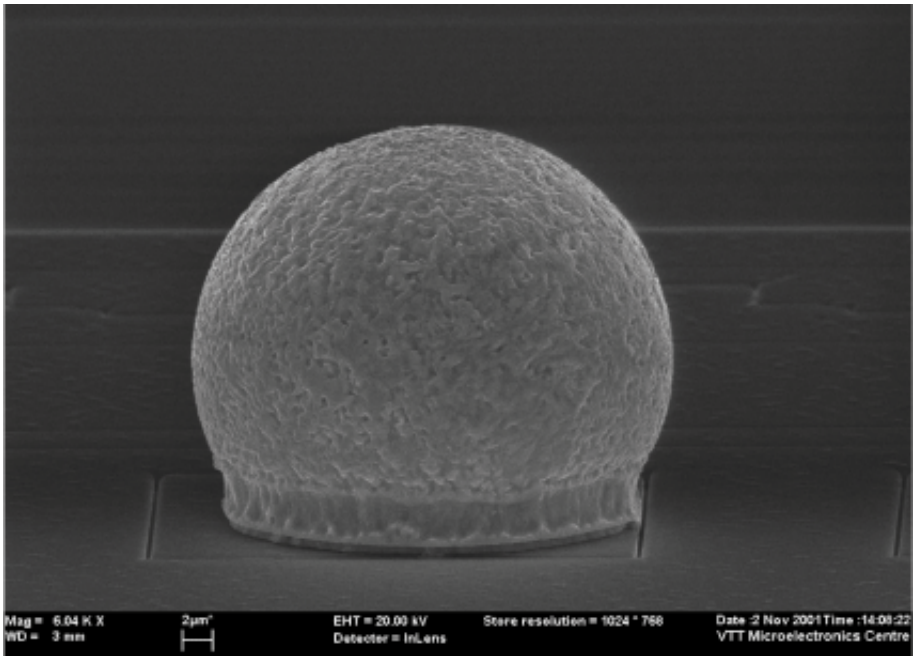

Figure 2.2: Electron microscope photograph of a solder bump on the readout chip as used for the ALICE SPD. The bump diameter is about 25 microns and must be applied with extreme precision for the connection between readout and detector to function properly. Source: VTT, Finland.

[2], mainly for centrality selection and muon arm trigger. A full pixel read out at HI luminosity takes about 400 μs yielding an effective 2.5 kHz readout for the L1 trigger. The 2D pixel layer is a very simple layout and this contributes to an easy alignment and calibration process due to the high geometrical precision. The very high density of pixels however requires a large amount of connections and electronic readout channels; the SPD was originally designed to have about 15 M individual pixels [82], this was later reduced to the installed 9.8 M 50×425 μm^2 channels [83]. Good track resolution is paramount for calculating the different parameters involved in a b-tagging algorithm. This makes the SPD an essential component for bottom-electron analysis through secondary vertexing. Unfortunately, during the 2009-2011 runs there was a problem with the cooling system of the SPD[3], thus parts of the SPD

[2]L0 and L1 triggers indicate on what "level" the trigger condition is computed. L0 is the fastest decision, usually done locally directly on the detector readout of a sub-part of a detector, while L1 is a slower more computationally intensive trigger selection usually employing larger information from a full detector. The final trigger is the High Level Trigger (HLT) which combines information from all detectors in a rough calculation on a cluster farm, after the event has been read-out, but before it has been saved to storage. As an example for the EMCal, a L0 trigger decision can be reached in about 1.44 μs and a L1 jet-patch trigger takes about 2.7 μs to compute.

[3]Private conversation with Elena Bruna, ITS expert.

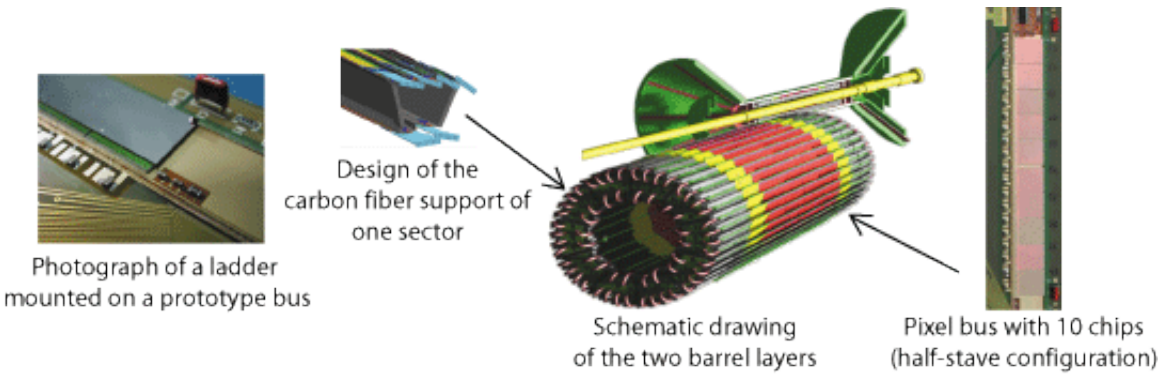

Figure 2.3: ITS SPD, schematic drawings of individual components. Source: ALICE ITS.

were kept off-line, reducing the efficiency of the detector by 30-50%, see Section 4.2. See Table 2.1 and 2.2 for dimensions and resolutions of the SPD.

SDD

The SDD consists of planar silicon drift detectors that make use of the time it takes for charges to drift to a collecting anode. This provides knowledge of one dimension and in combination with the ϕ-readout this allows for a two dimensional readout. Instead of diffusion/drift of the electron-hole pairs to the collector, the electron-hole pairs are confined into an electric potential well causing a drift perpendicular to the semiconductor surface, see Figure 2.4. This makes the design relatively easy in terms of density and readout channels, at the expense of speed. For a discussion about silicon drift detectors, see [84]. Drift detectors can be constructed in many different geometries, thin segments as the ALICE SDD, large rectangular areas up to 2.5 $\times$ 2.5 cm or radial geometry. The ALICE SDD consists of 260 detector components, each with 2$\times$256 channels. The sensitive area of a drift segment is 70.2$\times$75.3 mm^2 and has a two-dimensional resolution of 30 μm in both coordinates [85]. The drift time of the electrons is about 5.4 μs on average which sets the limit of the speed of the detector. In addition to two-dimensional read-out, it is also designed to be two of the four layers involved in the computation of dE/dx for low momentum tracks. In the 2011 data, the SDD had some operational problems and was excluded for certain analyses, most notably parts of the 2.76 TeV proton-proton run. In the data set that was analyzed for this thesis the SDD was used only in conjunction with the other six layers to have a minimum of four hits for a good quality track. See Table 2.1 and 2.2 for dimensions and resolutions of the SDD.

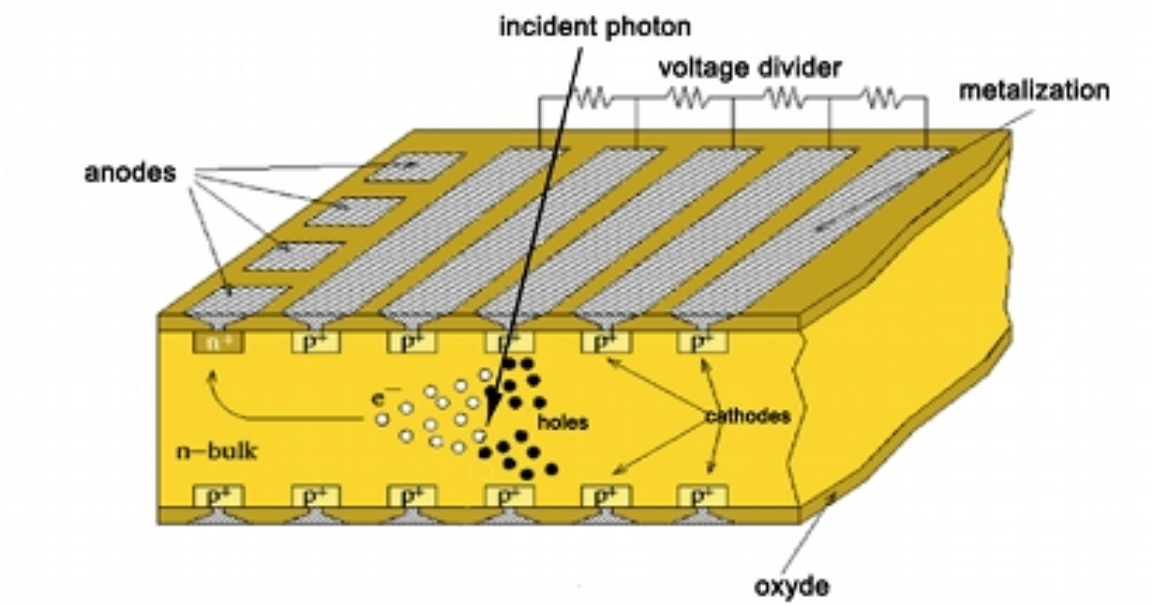

Figure 2.4: Schematic of an SDD. An incident particle (here photon) creates drift electron/holes that will drift in a potential. This allows for a 2D position measurement. Source: ESA 2011.

SSD

Silicon strip detectors are detectors that have a series of narrow parallel-strip electrodes that have been fabricated on a single surface. This provides for fine spatial resolution in one dimension. Double sided strip detectors have electrode strips in an orthogonal pattern on opposite sides of the wafer. This technique has been around for a long time and is today industrialized and relatively inexpensive. Since the average track density is less than 1 track per cm^2 at larger radii, this type of silicon detector was chosen for the two outermost layers of the ITS. For a more in-depth discussion, see [77]. The ALICE SSD is built from 1,698 strip modules, for a total of 2.7 M channels, that provides a resolution of a few tens of μm [86]. The high resolution at the outermost ITS radius is needed for TPC track-matching [76], see Section 4.2. The SSD is also used for dE/dx readout in conjunction with the SDD for a total maximum of four dE/dx measurements. This detector was used in the analysis of this thesis where a global constraint of a minimum of four of six hits in any of the silicon layers is required. See Table 2.1 and 2.2 for dimensions and resolutions of the SSD.

Table 2.1: Dimension of the ITS detector layers as initially designed [82].

ITS Layer	Type	r (m)	±z (m)	Area (m^2)	Channels
SPD 1	pixel	0.039	0.165	0.09	5.24 M
SPD 2	pixel	0.076	0.165	0.18	10.5 M
SDD 3	drift	0.150	0.222	0.42	43 k
SDD 4	drift	0.239	0.297	0.89	90 k
SSD 5	strip	0.380	0.451	2.28	1.20 M
SSD 6	strip	0.430	0.508	2.88	1.52 M

Table 2.2: ITS Precisions and resolutions

Parameter	unit	SPD	SDD	SSD
Spatial precision r-ϕ	μm	12	38	20
Spatial precision z	μm	70	28	830
Two track resolution r-ϕ	μm	100	200	300
Two track resolution z	μm	600	600	2400

2.2.3 TPC

The ALICE Time Projection Chamber (TPC) is the largest of its kind in the world. It is designed to study HI collisions at LHC energies yielding charged-track densities $dN_{ch}/d\eta$ of 8,000 tracks. For one PbPb collision this amounts to about 20,000 reconstructed charged tracks per event within the TPC. It can also measure ionization energy loss of particles, dE/dx, which is used for particle identification.

TPCs have been around since the late 1970s, invented by LBL (Lawrence Berkeley Laboratory) physicist David Nygren [87], [88] and used at SLAC. It has been used in many experiments, such as at LBL's Bevalac, CERN (NA36, NA49 and ALEPH) and the Relativistic Heavy Ion Collider (RHIC) at BNL (Brookhaven National Laboratory). After being out-competed by other faster detectors in high energy particle physics due to a few decades with rapid technological advancement, it found application in the study of HI collisions with high track densities.

A TPC is a gas detector that uses gas as a medium that particles interact with, creating electron-ion pairs that are measured. It has a large volume of inert gas as the ionization medium, a large static electric field causing ionized charge to drift to the end-plates where the deposited charge can be measured. See Figure 2.5. The measurement is performed by counting charge after some means of amplification,

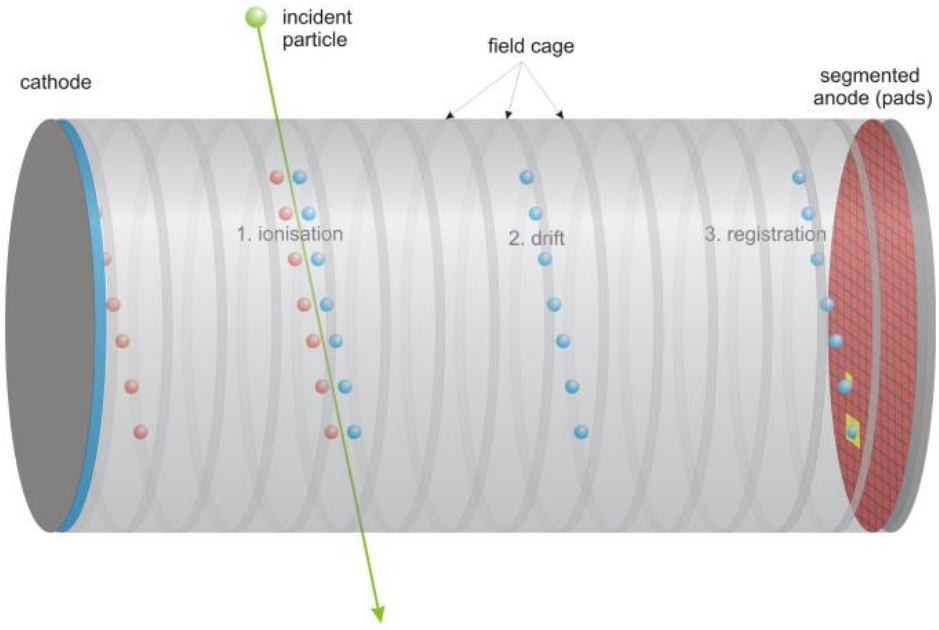

Figure 2.5: Schematic of the working principle of a time projection chamber. An incident particle ionizes charge along its path. The charge will drift due to the potential field. The electrons will then be counted after amplification at the anode. Source lctpc.org.

most commonly by the use of multi-wire proportional chambers. By measuring the drifting ionized electrons r-ϕ coordinates at the end-plates this gives information about two dimensions. By recording the times when the ionized particles arrive along with knowledge of the drift velocity, the third spatial dimension can be reconstructed. The result is a complete three-dimensional picture of the event. The advantages are a fairly inexpensive device with large acceptance that can measure charged tracks in three dimensions at superior track density. The main disadvantage is a slow detector, limited by the drift time of the ionized electrons from their point of origin to the end plates. ALICE's strategy to study heavy-ion collisions through an almost complete measurement of particle production in the central region resulted in selection of a TPC as the main tracker.

ALICE TPC

The ALICE TPC was designed with the following parameters in mind: large η-acceptance, low material budget, high event rate, good spatial resolution and reasonable readout-data size. For a full discussion, see [89] and for a layout of the TPC geometry see Figure 2.6. The large acceptance is needed to provide tracking for the other detectors involved in the experiment. The ITS, TRD and TOF are all designed

with an acceptance of $|\eta| < 0.9$. This is absolutely necessary to ensure sufficient statistics for the physics goals of the ALICE experiment, such as high-p_T electron measurements. The geometry of the TPC is of cylindrical design with an inner radius of 80 cm, an outer radius of 250 cm with a total length of about 5 meters. It is built with six main structural components, four cylinders (the TPC is split in half) and two end-plates. The reason for double cylinder design is the need for isolating the drift-gas from atmospheric gas components (O_2, N_2 and H_2O), some harmful to the drift gas. The second cylinder contains the field cage that houses the 100 kV static electrical field. The field cage is divided in the middle by the central high-voltage (HV) electrode, a thin conducting sheet where the potential is held at 100 kV. At both end-plates of the TPC, multi-wire proportional chambers are held at ground, or low potential. To minimize the distortion of the drift field by the amplification field, and to minimize the integral charge deposit on the anode wires, a gate grid is installed 3 mm above the anode wires. This prevents ion back flow, which may disrupt readout. The gate grid can operate in two modes, in the open-gate mode all the gating-grid wires are held at the same potential, allowing electrons from the drift gas to enter the amplification region and ions to flow back. The gate only stays open for about 100 μs when there is a valid trigger. In the closed mode the gate grid is biased with a dipole field which prevents drift electrons to reach the amplification region. The main drift field inside the field cage must be highly uniform and smooth for good track resolutions but also to protect against high-voltage discharges when a 400 V/cm field is present. To ensure high uniformity of the field, the mantle area of the TPC cylinder is coated with aluminum strips connected together by resistors, in order for the field to slowly decrease from maximum potential at the mid-section to ground at the readout pads. This creates a non-uniform field close to the outer radius of the active volume, but simulations show that the inhomogeneities have dropped to $\leq 10^{-4}$ at 2 cm from the TPC wall [89]. The layout of the ALICE TPC can be seen in Figure 2.6 and the TPC parameters are found in Table 2.3.

The requirement of low material budget is paramount to any physics measurement in order for particles not to undergo secondary scattering or create new particles via interactions with material. This is directly in contradiction to the strict high structural integrity against gravitational loads, thermal loads and high uniformity and smoothness of the field cage. The choice of material fell on composite material and a honeycomb-like structure of Aramide fiber, which is commonly used within the aerospace industry (which provides competence and manufacturing infrastructure). The ionization gas has to be included in the material budget and by selecting a light

Table 2.3: ALICE TPC parameters, [90].

Pseudo-rapidity coverage	$\|\eta\| < 0.9$ for full radial track length $\|\eta\| < 1.5$ for 1/3 radial track length
Azimuthal coverage	360°
Radial position active volume	848 < r < 2,466 mm
Radial size of vessel, outer dimensions	610 < r < 2,780 mm
Radial size of vessel, gas volume	788 < r < 2,580 mm
Length of active volume	2 × 2,497 mm
Inner readout chamber geometry	trapezoidal area, 848 < r < 1,321 mm
Pad size	4 × 7.5 mm^2 (r-ϕ × r)
Pad rows	63
Total pads	5,504
Outer readout chamber geometry	trapezoidal area, 1,346 < r < 2,466 mm
Pad size	6 × 10 and 6 × 15 mm^2 (r-ϕ × r)
Pad rows	96
Total pads	9,984
Detector gas	Ne-CO_2-N_2 [85.7-9.5-4.8 %]
Gas volume	90 m^3
Drift voltage	100 kV
Gain (nominal)	7,000-8,000
Drift field	400 V/cm^2
Drift velocity	2.65 cm/μs
Drift time	94 μs
Material budget (including gas)	$X/X_0 = 3.5$ % near $\eta = 0$

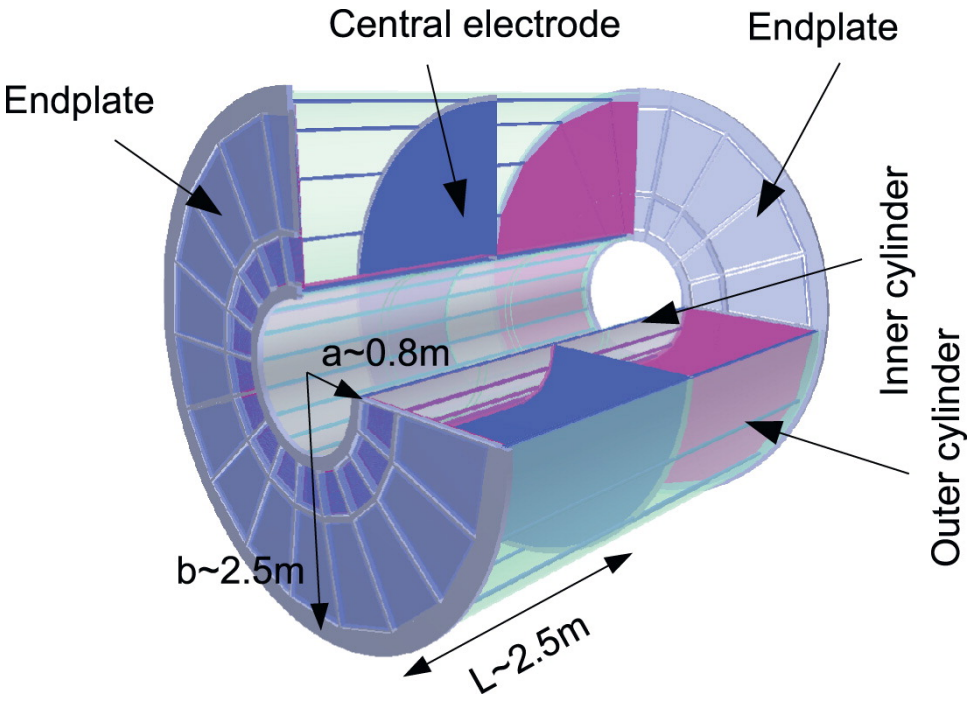

Figure 2.6: The ALICE TPC.

drift gas, a mixture of Ne-CO_2-N_2 (85.7-9.5-4.8 %), the total material budget for the TPC is less than 3% of a radiation length[4].

The high event-readout rate is a very important aspect of the TPC since the TPC is the slowest of all ALICE detectors, effectively setting an upper limit on the speed at which events can be recorded. The LHC delivers both proton-proton and PbPb collisions at a high rate, thus a fast detector is needed to minimize influence from other secondary colliding bunches. For proton-proton collisions the bunches are too well squeezed together at the collision point that one has to purposely defocus the proton-proton beams at the ALICE interaction point in order for the detector not to be saturated at all times. See Figure 2.7 for integrated luminosities, ATLAS, CMS and LHCb versus ALICE. The drift time is the limiting factor of the TPC. This is a function of the magnitude of the electric field present in the TPC and the type of gas mixture used. There are limits to each of these parameters; for the current choice of ionization gas and a 100 kV drift field an average drift time of 94 μs is obtained, yielding an upper rate of about 1.4 KHz for full readout of a proton-proton collision. The PbPb collisions are limited by the bandwidth of information that can be delivered to the counting rooms.

[4]For a definition, see Section 3.1

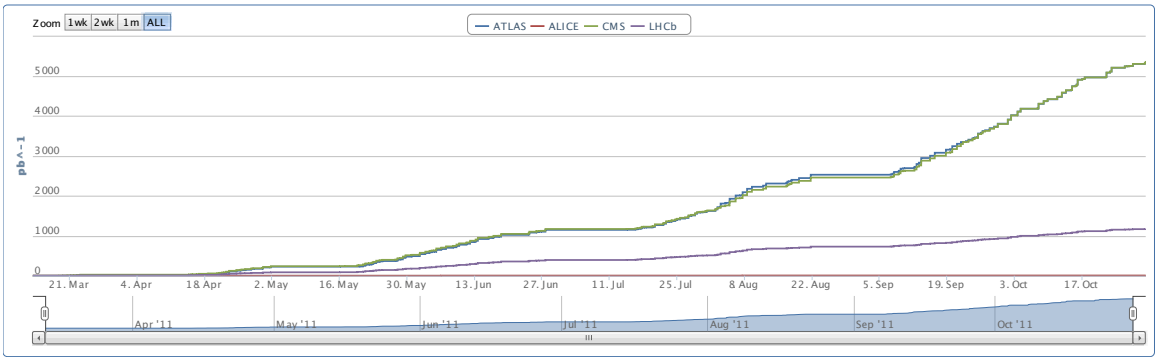

Figure 2.7: Integrated luminosities delivered 2011 by the LHC to the different experiments. The ALICE integrated luminosity is very low, shown in red close to the x-axis.

Good spatial resolution is needed for a precise track reconstruction. This is dependent on the readout electronics and the signal (number of electron-ion pairs created by a charged particle) amplification. Different readout techniques were studied, including Gas Electron Multipliers (GEM) and Ring Cathode Chambers (RCC) [91], but in the end multi-wire proportional chambers were selected. The multi-wire proportional chambers receive the drifting electron cloud, resulting from a particle passing through the drift gas. The electrons enter the anode-wire plane where a large electric field around the wires accelerate the electrons. The accelerated electrons cause secondary ionization resulting in an avalanche of electrons, amplifying the signal. The multi-wire proportional chambers yield a nominal gain of about 8,000. The overall area of the readout pads is 32.5 m^2 and consists of multi-wire proportional chambers with about 570,000 cathode-pad readouts. This is to keep the average occupancy low (maximum occupancy $< 40\%$) and ensure the necessary dE/dx and position-measurement resolution.

Finally a clever readout method must be employed. The average amount of information from the TPC readout in one proton-proton collision is about 100-200 kB, and about 70 MB for a PbPb event. With a data-taking rate of a few hundred Hertz for PbPb or 1 kHz for proton-proton collisions several tens of GB/s have to be processed. It is simply not possible to save data at that rate with any available commercial data system, thus first the data have to be delivered to the High Level Trigger cluster (HLT) [92]. This is done in parallel fiber-optic links from the detector to the counting rooms with a total bandwidth of 35 GB/s. The HLT provides for selection and recording of events of interest, reducing the data flow to manageable levels, i.e. 100s of MB/s.

Physics

Almost all the main physics goals of ALICE involve the use of the TPC; anything that requires central tracking makes use of the TPC. Initially when the ALICE experiment was conceived the TPC was the main PID detector for all particle types. This changed later when the Transition Radiation Detector (TRD) was added, to be positioned after the TPC and the TOF. Together with the ITS, the TPC provides charged particle momentum measurement up to p_T <100 GeV/c as well as particle identification through dE/dx measurement for studies of hadronic and leptonic signals with p_T <10 GeV/c and $|\eta| < 0.9$. As for electrons in particular, the TRD-TOF-TPC system was to be used for high-p_T (up to 10 GeV/c) electron identification and triggering. Including the TRD in the analysis of this thesis would have been optimal for electron identification, however the TRD was not fully operational and not well understood at the time of analysis, as a result instead only the TPC+EMCal combination were used for triggering and particle identification of high-p_T electrons.

Energy loss, Space-point Resolution and Momentum Resolution

Charged particles interact with the ionization gas through Coulomb collisions, creating free charges while losing energy. The mean energy loss of a charged particle in a medium was worked out by H. Bethe in 1930, see [93], [94], and later refined by F. Bloch[5] in 1933, thus forming the Bethe-Bloch equation:

$$\frac{dE}{dx} = \frac{4\pi}{m_e c^2} \cdot \frac{nz^2}{\beta^2} \cdot \left(\frac{e^2}{4\pi\varepsilon_0}\right)^2 \cdot \left[\ln\left(\frac{2m_e c^2\beta^2}{I \cdot (1-\beta^2)}\right) - \beta^2\right], \tag{2.1}$$

where β is the velocity of the particle, z particle charge, n is the electron density of the target and I is the mean excitation potential of the target. The energy loss is then measured in the TPC by integrating the charge deposited in a TPC cluster. It has also been shown that for tracks within the TPC acceptance one can use the "maximum digit", or essentially deposited charge, per readout pad in the TPC cluster for evaluation of dE/dx; no average in a TPC cluster is necessary. The charge of the cluster, or the maximum digit in the cluster, is divided by the length of the corresponding track segment, then the dE/dx value is calculated using the truncated mean method. Extensive simulations have been done for the track resolution, [89] which agrees with more recent test-beam measurements at the TPC test facility at

[5]Felix Bloch was a Swiss physicist who also was the first Directeur Général of CERN 1954, when the organization was officially formed.

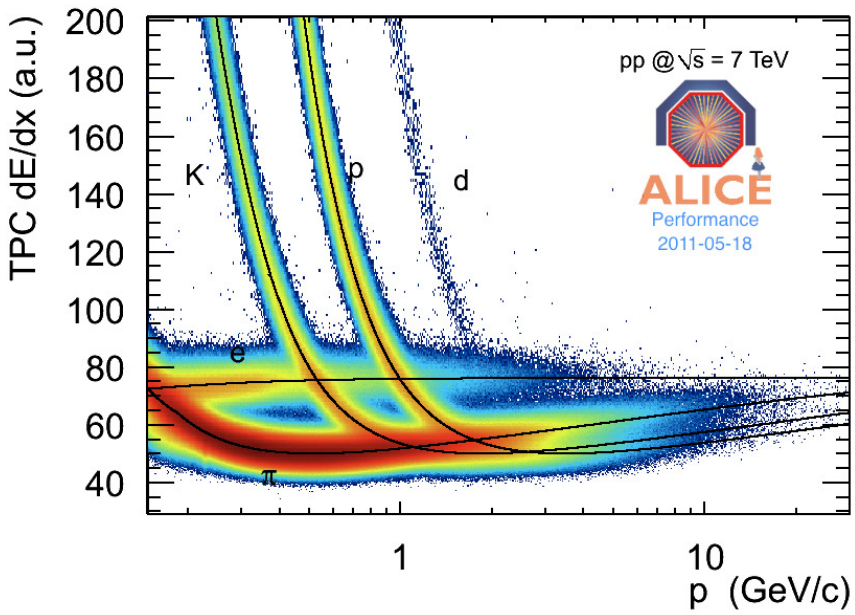

Figure 2.8: TPC energy loss versus momentum for 7 TeV pp collisions. Ideal lines fitted to data using equation 2.1 have been added for electrons, pions, kaons and protons. Source: ALICE repository.

CERN showing that energy-loss resolution for a 3 GeV/c proton is about 5.1 % [95]. An example of a TPC dE/dx measurement can be found in Figure 2.8.

A miniature TPC model was used to study and to estimate the space-point resolution of tracks reconstructed from TPC clusters by the ALICE TPC track-finding algorithm [89], [96], where the tracking efficiency is about 90%. This TPC mini-module was built for the purpose of trying out the TPC concept before a full scale model was constructed. The space-point resolution is dependent on many parameters, the major ones being granularity of readout, diffusion and distortion of the drifting charge clouds, readout gain factors, etc. The space-point resolution was calculated in simulations and measured with the miniature TPC model, and they were in agreement [95]. For the mini-module measured resolutions, see Figures 2.9 and 2.10.

Finally, the TPC-ITS combined track momentum resolution is shown in Figure 2.11. This has been estimated from the 2010 LHC10d period with 7 TeV pp collisions.

2.2.4 EMCal

The original ALICE plan did not include the EMCal detector; PHOS was the only electromagnetic calorimeter within ALICE capable of particle identification. PHOS

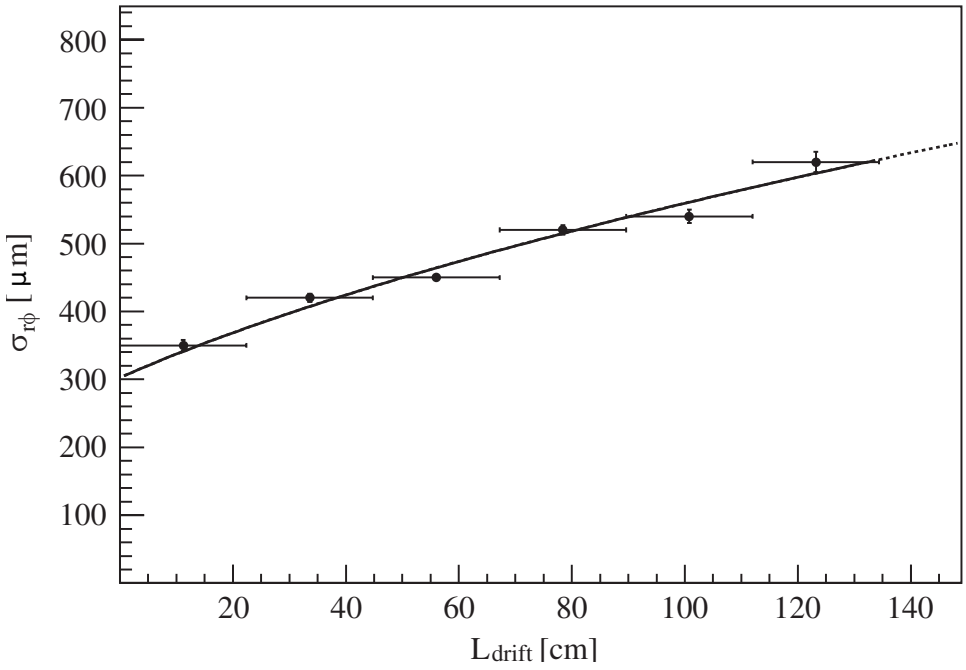

Figure 2.9: TPC r-ϕ-resolution versus drift length for the TPC test module [95]. In order to compare these numbers with the full size TPC simulations they have to be extrapolated to 250 cm.

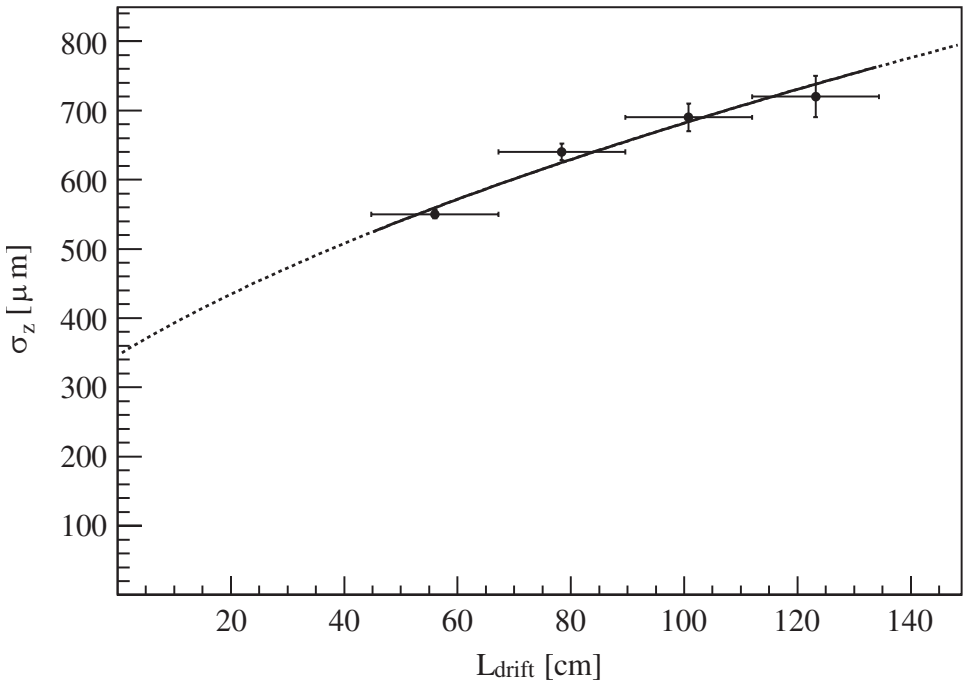

Figure 2.10: TPC z-resolution versus drift length for the TPC test module [95]. In order to compare these numbers with the full size TPC simulations they have to be extrapolated to 250 cm.

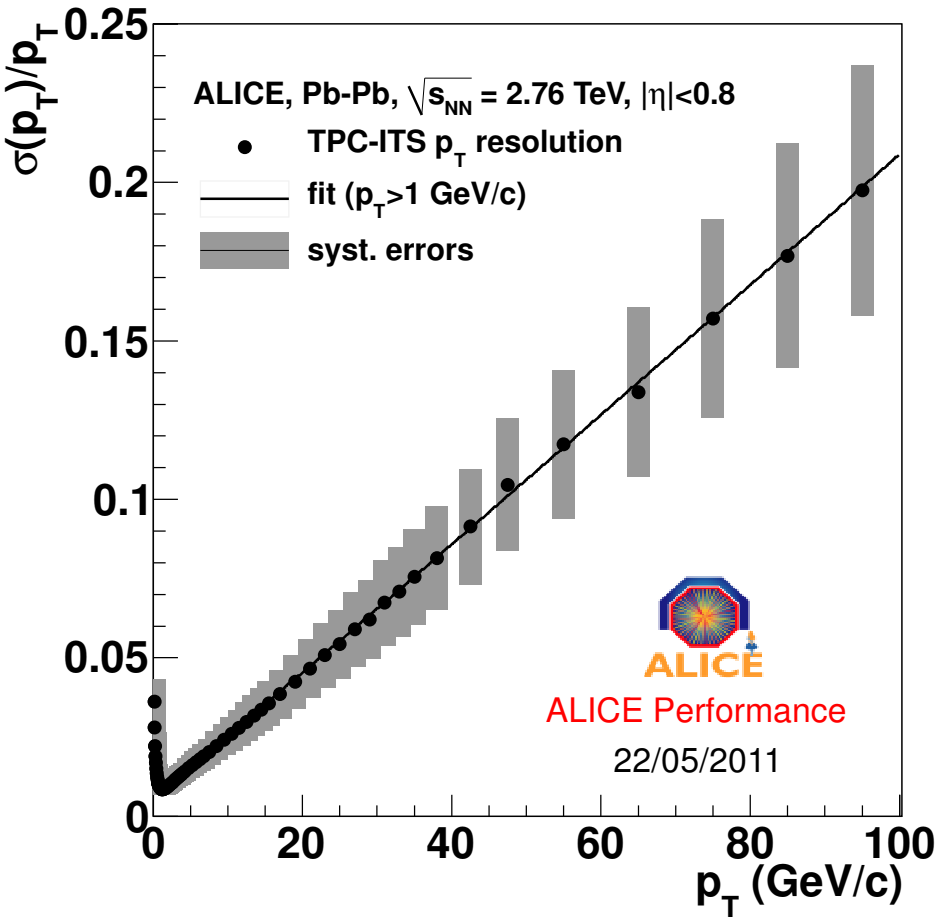

Figure 2.11: ITS-TPC combined track momentum resolution versus transverse momentum. Source: ALICE repository.

is a Photon Spectrometer built to measure photons, see Figure 2.1. It has a high granularity but a rather limited $\eta - \phi$ range; only $|\eta| < 0.12$ and $200° < \phi < 320°$ in azimuth. After the success of RHIC it was realized that there is a need for a larger-coverage calorimeter, for full jet reconstruction and other measurements. The EMCal was designed and built in the US and Europe. It was then tested, calibrated and installed in three rounds, four Super Modules (SM) before beam turn-on in 2009, six more SMs in 2010 and in 2012 two half modules were finally added. The full EMCal spans 110 degrees in azimuth with an η-acceptance of $|\eta| < 0.7$. A few of the SMs were assembled and calibrated at Yale in 2009-2010. For a more detailed description of electromagnetic calorimeters in general and the ALICE EMCal, see Section 3.2 where a more in-depth discussion of calorimeters along with test measurements performed with the EMCal mini-module is presented.

2.3 ALICE data analysis

The development of the AliROOT framework began in 1998 and it is the collection of all ALICE related software integrated into one software platform. It is an object-oriented addition to ROOT and requires several add-on packages to work properly (such as GEANT3 for simulation of particle-detector interactions). The software contains all the software components needed for a modern particle detector, including but not limited to, event simulation generation, detector simulation, event reconstruction, data acquisition, HLT cluster code, off-line data analysis and GRID computing. It is an enormously complicated framework that is updated on average 10 times a day for 14 years[6]. It is written in C++ as an addition to the ROOT framework and has about 4,000 C++ classes. This is the main software used for simulation, reconstruction and analysis in this thesis.

2.3.1 GRID computing

The GRID is the software and hardware used to allow for thousands of computers around the world and PB of data to be seamlessly available to anyone within the ALICE collaboration anywhere in the world. One of the greatest challenges with the ALICE experiment is the large amount of recorded data that needs to be securely stored and processed for analysis. The solution was a GRID computing network with different tier facilities spread around the world [97]. In one year of data-taking, ALICE

[6]Current AliROOT trunk SVN version is 53328 as of March 23, 2012.

stores about 10 PB of data and simulations, this will first be stored at transient storage Tier-0 at CERN when recorded. Tier-1 are major computer centers that provide safe storage, while Tier-2 are smaller regional computing centers. Data will be transferred to Tier-1 and Tier-2 facilities after reconstruction of a data set is completed, creating several backups and redundancy around the world by the use of automated scripts.

It works as a virtual super-cluster with a unified directory that uses the Internet and dedicated fiber to store and access data. When an analysis job is submitted efficient algorithms split the job into sub-jobs and distribute them to a certain facility that has access to whatever data are required for the analysis. The jobs will run at whichever site is allocated, and once the analysis is done the individual jobs will copy the output back to the user directory. At the moment ALICE has around 70 storage elements with about 30 PB of storage installed and about 40,000 computers available for reconstruction, simulation and user analysis[7].

2.3.2 Analysis trains and local clusters

Having a uniform directory with PBs of data and thousands of jobs running at any hour results in a somewhat complex system. Originally the GRID computing was the only supported and recommended solution for analyzing data. In 2010, when the first year of data became available, institutions with sufficient resources started to run on local clusters using local mass-storage elements, most notably the GSI. The choice between full control over software and execution of analysis along with extensive usage of local computational resources, versus using the GRID framework, fell on local clusters. In 2011 the ALICE EMCal group switched to PBS (Portable Batch System) execution on local Linux clusters, mainly at the LBNL computing site (NERSC) but also at Yale "bulldog" clusters. Much personal time was invested into writing data-copying macros, and interface scripts between the ALICE software and modern PBS Linux clusters. About 99 % of the analysis was done with these clusters using downloaded data from the GRID, but for the final spectra, due to standard policy, the analysis was run on GRID using the AliEn framework. In order to make data analysis as efficient as possible, time was also invested into building an "analysis train" [8]. The architecture, coding and deployment of this analysis train on NERSC,

[7] See `http://alimonitor.cern.ch/` for live statistics.

[8] An analysis train is a piece of software that will access recorded events and run one or several analyses over the data. The term *train* comes from the analogy to a real train which can have several train-cars added while running on the same track. This is commonly used to make data analysis more efficient running several analyses on the same data at the same time. For complete documentation of the NERSC EMCal analysis train, see `http://rnc.lbl.gov/Alice/wiki/index.`

along with the downloading of data, took about 6 months and was a prerequisite for this thesis to be completed. The train accesses a data set and performs certain analysis tasks in a certain order. That way, execution, data quality and reliability and physics selection could be controlled centrally, while individual users can add their specific analysis to the analysis train, maximizing the efficiency of computing resources utilization. The downside is that one has to keep local copies of large data sets and running over this uses large computational resources.

php/Analysis_train_info

Chapter 3

Electromagnetic calorimeters

This chapter describes electromagnetic calorimeters, the ALICE EMCal and analysis of test beam data. In section 3.1 electromagnetic calorimeter operation and physics are described in general. The ALICE EMCal is described in detail in section 3.2. Calibration of the ALICE EMCal is also described in section 3.3, along with non-linearity in subsection 3.3.2 since this is an important procedure in the analysis.

3.1 Electromagnetic calorimetry

It is important to understand the underlying processes in calorimetry to get a good understanding of what is involved in a measurement of particle energy and position, and to ultimately perform particle identification. This chapter describes how an electromagnetic calorimeter works, using the ALICE EMCal as an example.

The objective of the electromagnetic calorimeter is to measure the energy of particles, in particular of electrons and photons, interacting with the calorimeter. There are many advantages of using electromagnetic calorimeters as opposed to magnetic spectrometers, mainly good energy resolution and acceptance, measurement of the neutral energy component in events, and the compactness and economics of the device. The electromagnetic calorimeter is a destructive detector since it absorbs parts or all of the incoming particle energy, distorting or destroying any subsequent measurement. It relies upon an absorbing medium to slow down and absorb the particle, and a scintillating material to convert the particles' incident energy into photons. These photons are then detected and converted into an electric signal that can be measured.

Usually layers of absorbing material and scintillating material form the main part of the electromagnetic calorimeter. A dense material, such as lead, is used as absorber

and common scintillating plastics are used for scintillator material. In some calorimeters the scintillator also acts as absorber material, such as the tungsten crystals in the ALICE PHOS calorimeter. The resulting detector is far more expensive than a simple lead/plastic layered detector. The ALICE EMCal is a lead/plastic layered calorimeter.

When particles are absorbed in the calorimeter the kinetic energy is converted into exciting atoms or molecules in the calorimeter material. The excited atoms or molecules of the scintillating material will emit part of this excitation energy in the form of visible light. These photons are the basis for the calorimeter output signal, and are fed to photon multiplier tubes (PMTs) through optical fibers, to be converted into an electric signal. The absorbed energy by the calorimeter and the measured signal is very much linear for a wide range of particle incident energy. This is because the incoming particle's energy is converted into a shower of electron-positron pairs with less and less energy until the created electrons and positrons can be absorbed into the material themselves through excitation of atoms or molecules. Thus an electron with an energy of 2 GeV will create twice the amount of shower particles as an electron with an energy of 1 GeV creates. This is true for most energies and is discussed more in the non-linearity section.

3.1.1 Particle interaction with the EMCal, shower development

The electromagnetic calorimeter can detect a wide range of particles, but is particularly good at detecting photons and electrons due to their electromagnetic interaction. Also pions and muons as well as neutrons can be measured despite their relatively weaker interaction with the detector. Since the main goal of this thesis was to obtain a good electron sample it is important to understand the interaction of electrons versus other particles with the calorimeter. Electrons interact through a few well understood QED processes, such as Compton scattering, e^+e^- pair production and bremsstrahlung. The relevant energy range for electrons in the ALICE EMCal is greater than $\sim$750 MeV due to the distance of the interaction point to the calorimeter and the magnetic field. From the electrons that are created close to the collision, only those with momentum greater than $\sim$750 MeV will reach the EMCal due to the bending of charged particles in a magnetic field. At this energy Bremsstrahlung is the dominant source of energy loss, in fact any electron above 10 MeV will dissipate energy mainly though Bremsstrahlung. Secondary photons are created through the

Coulomb interaction with the electric fields of the atomic nuclei and can in turn create new electron-positron pairs. These tertiary electron-positron pairs will interact with the medium through Bremsstrahlung or other means and the process is repeated creating a shower of particles, each step with less energy. The number of particles will increase until the electron or positron has low enough energy to interact through ionization or excitation of the material.

One of the most important design parameters to consider is the radiation length X_0 which determines the properties of the shower shape. One radiation length is the distance an electron travels in a material such that its initial energy E_0 is reduced to $\frac{E_0}{e}$. Empirically the radiation length is approximately

$$X_0 \approx \frac{716 g cm^{-2} A}{Z(Z+1)\ln(287/\sqrt{Z})}, \tag{3.1}$$

where A is the weight of the material and Z is the atomic number [77]. The ALICE EMCal has $X_0 = 3.2$ cm. The average energy of an electron that travels a distance x is then given by

$$\langle E(x) \rangle = E_0 e^{-\frac{x}{X_0}}. \tag{3.2}$$

Furthermore the maximum depth of a shower is defined to be at the depth where the number of secondary particles is maximum. This is given by

$$t_{max} \approx \ln \frac{E_0}{\epsilon} + t_0, \tag{3.3}$$

where t_{max} has units of radiation lengths, E_0 is the original particle energy and $t_0 = -0.5$ for electrons. This shows the important property of the logarithmic dependence of the shower maximum on the initial energy. A thickness of a few tenths of a centimeter is sufficient to absorb electrons at hundreds of GeV.

The spread or dispersion of the shower as a function of depth is caused by scattering of electrons and positrons away from the incident axis. This can be parameterized by the Molière radius R_M, which is the average deflection from the incident axis at the critical energy after traversing one radiation length

$$R_M \approx 21 MeV \frac{X_0}{\epsilon(MeV)}. \tag{3.4}$$

A cylinder with this radius contains on average 90% of the shower energy. This radius in turn then determines the granularity of the detector if the position of the incident particle is to be determined. Another interesting property of shower shapes

from electrons is that R_M is almost entirely independent of energy. It is therefore a crucial parameter when one designs a calorimeter. The ALICE EMCal has a square granularity of 6×6 cm and most of the energy is expected to be deposited within one tower if the detected particle is incident at the center of the tower.

3.1.2 Energy response and non-linearity

The energy response of a calorimeter is defined as the average calorimeter signal divided by the energy of the particle responsible for the signal. The calorimeter signal itself is derived from an electric signal delivered by a PMT that amplifies and converts visible photons into an electric signal. The photons are a result of some of the deposited energy in the calorimeter being converted into visible photons. The photons are picked up by optical fibers, or another means of light guide, that leads the scintillated photons away from the active matter within the calorimeter towards the PMT. For the ALICE EMCal these optical fibers run along vertical holes in the Pb/scintillator sandwich array.

As previously mentioned, the relationship between the calorimeter signal and the energy of the particle is linear for most energies. Deviations from this relationship are mainly a decreasing response at low or high energies, and must be accounted for. There are many effects that contribute to this behavior, such as other means of energy loss (at low energies), saturation effects in the PMTs and shower leakage effects. In order to measure these effects the most common procedure is to use a test module along with particles with known energy. It can also be measured through other means such as by looking at the π^0 invariant mass peak within recorded data, or the reconstructed electron E/p peak. In Section 3.3 this non-linearity dependence is evaluated for the ALICE EMCal test beam mini-module. It was subsequently implemented into the clusterizer that ultimately yields the energy of a cluster that is used for particle identification.

3.2 The ALICE EMCal

Having covered the basics of calorimeters and their operation in general, and having put off the introduction of the ALICE EMCal in the second chapter, it is now appropriate to introduce it. For a full discussion, see [98] and [99].

The physics motivation for the ALICE EMCal focuses around the study of the QGP through hard probes or jets. Jet quenching measurements have played a sig-

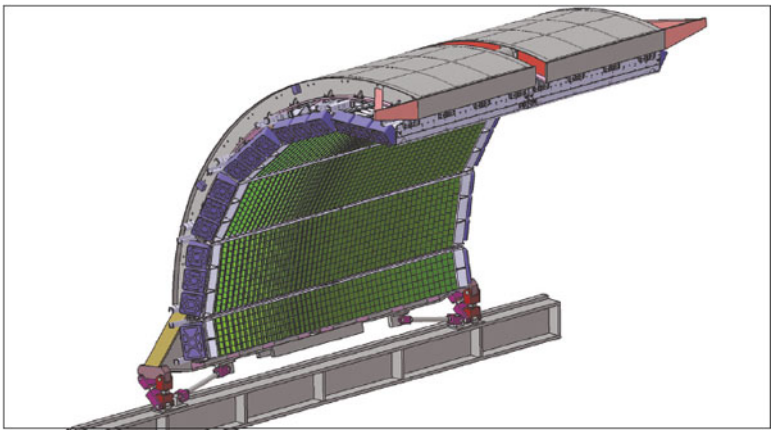

Figure 3.1: The ALICE EMCal

nificant role at RHIC and this was to be extended to ALICE with the help of the EMCal. It also includes enhancement of interesting events through triggering and extends the existing ALICE particle-identification range of electrons and photons to higher transverse momentum.

The ALICE EMCal is situated within the L3 magnet, after the central tracking detectors, the TRD and the TOF, see Figure 2.1. It has a cylindrical curvature with a depth of about 110 cm, see Figure 3.1. The face of the EMCal is about 450 cm from the collision point. The full detector spans about 107 degrees in azimuth and about ± 0.7 in η. The conceptual design of the detector is based on the Shashlik technology previously implemented in the PHENIX detector, HERA-B at HERA and LHCb at CERN, i.e. Pb-scintillator sampling calorimeter with 76 alternating layers of 1.44 mm Pb and 77 layers of 1.76 mm scintillator (polystyrene based, injection-modulated scintillator; BASF143E + 1.5 % pTP + 0.04 % POPOP). It is divided into 10 large so-called "super modules" (SMs) and two 1/3 size SMs. The SMs are further divided into modules, each module containing 4 towers (sometimes referred to as cells) each. Each full SM has $12 \times 24 = 288$ modules arranged in 12×1 strip modules (24 in each SM) for a total of 1152 towers per SM. The 1/3 SMs are each made from $4 \times 24 = 96$ modules for a total of 384 towers per 1/3 SM. Each full SM spans $\Delta\eta = 0.7$ and 7° in ϕ.

Each module that contains $2 \times 2 = 4$ towers is the smallest building block of the calorimeter and is a self-contained detector unit. The 4 towers in a module span about $\Delta\eta = 0.014 \times \Delta\phi = 0.014$ (about 6×6 cm^2) each at $\eta = 0$. The towers are approximately projective in both η and ϕ to the interaction vertex since the individual modules are tilted increasingly as a function of pseudo-rapidity, and along the total

width of 12 modules in ϕ this makes for approximately projective towers. The towers consist of 77 layers of Pb-scintillator for a total active depth of about 24.6 cm. This corresponds to about 20 radiation lengths and simulations show that the deviation from a linear response at maximum 100 GeV is about 2.8% (due to shower leakage at the back of the calorimeter). As a part of this thesis the linear response, or non-linearity was measured using a small section and known particles with known incident momentum, see Section 3.3.

The energy resolution of a calorimeter is an important parameter. For a magnetic spectrometer, such as the ALICE TPC, the relative energy resolution increases as a function of momentum. For a calorimeter however, the energy resolution can be parameterized as

$$\sigma/E = a/\sqrt{E} \oplus b \oplus c/E, \tag{3.5}$$

where a, b and c are constants and E is the shower energy. The energy resolution decreases with increasing energy. The first term is due to stochastic fluctuation effects from energy deposit, energy sampling, light collection, efficiency etc. The constant b term comes from systematic effects such as shower leakage or calibration errors etc. The third term c arises from electronic noise summed over the towers of the cluster used to reconstruct the electromagnetic shower. These three contributions add together in quadrature, where the first term dominates the energy resolution for most of the relevant energy range of the EMCal. Only at higher energies the constant term b overtakes the first term. A GEANT3 simulation of the full EMCal yields a combined resolution of about $11\%/\sqrt{E} \oplus 1.7\%$, with the constants $a = (1.65 \pm 0.04)\%$, $b = (8.0 \pm 0.2)\%$ and $c = (7.4 \pm 0.2)\%$ over an energy range of 5 to 100 GeV [100]. This is compared to and confirmed by studies made with a test beam setup, with the resulting simulation and measurement shown in Figure 3.2. Finally the combined energy resolution in the detector can be measured with real pp data, and the result of this is shown in Figure 3.3.

The EMCal was installed at point 2 in the ALICE detector in three steps. The first step was to install 4 SMs before the 2009/2010 data-taking. This resulted in extensive minimum-bias pp data and one month of PbPb data with about 40% of the full EMCal installed. This was in some sense a test-run of the EMCal. In the winter of 2010/2011 the remaining 6 full SMs were installed, resulting in a much larger azimuthal coverage. At this stage the EMCal was used for triggering purposes, significantly increasing the amount of interesting events, both for jet and electron studies. 2011 yielded the 2.76 TeV pp reference run, along with 7 TeV pp data.

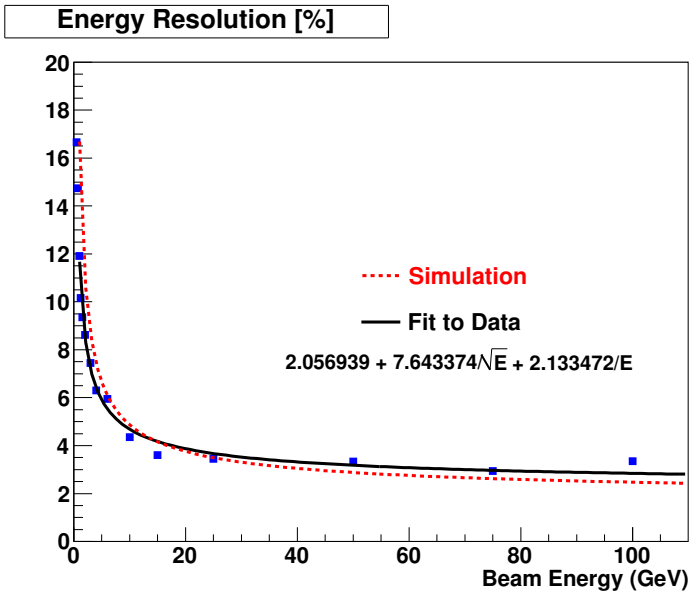

Figure 3.2: The EMCal energy resolution as a function of energy. A simulation is shown as the red dashed curve and measured data points are shown in blue. The black curve is a fit to the data.

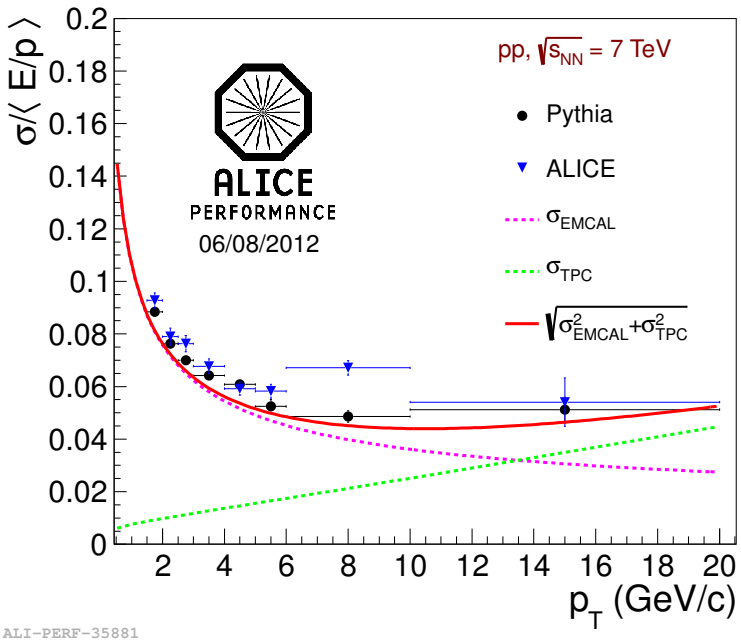

Figure 3.3: The combined TPC + EMCal energy resolution as a function of p_T of electrons. A simulation is shown as black data points and the measured data are shown in blue. The resulting curves are a combination (shown in red) of the underlying energy resolutions of the TPC (green) and the EMCal (magenta).

Table 3.1: The EMCal physical parameters

Quantity	Value
Tower Size (at η=0)	$6.0 \times 6.0 \times 24.6$ cm^3
Thickness Pb Absorber	1.44 mm
Thickness Scintillator	1.76 mm
Number of Layers	77
Effective Radiation Length X_0	12.3 mm
Effective Molière Radius R_M	3.2 cm
Effective Density	5.68 g/cm^2
Number of Radiation Lengths	20.1 X_0
Number of Towers	12288
Number of Modules	3072
Number of Super Modules	10 full, 2 one-third size
Weight of full SM	7.7 metric tons
Total Coverage	$\Delta\eta = 0.7$, $\Delta\phi = 107°$

The 2011 7 TeV pp data is the basis for this thesis. In the shutdown 2011/2012 the remaining two one-third SMs were installed, rendering the full design EMCal operational.

3.3 The ALICE EMCal mini-module analysis

Having introduced the basic concepts of calorimeters and being more familiar with the ALICE EMCal in particular, the response and physics were studied by using a part of the EMCal; the ALICE EMCal mini-module. One of the most important steps in commissioning an electromagnetic calorimeter is the test beam analysis. This section describes the mini-module and the test-beam data that were recorded in 2010 at the CERN PS and SPS accelerators in order to study the EMCal in a controlled environment. In this section we make use of known particles, electrons and (mostly) pions, along with known incident momentum, to study different aspects of the EMCal. Calibration is discussed which plays a fundamental role in the commissioning of a detector. Then the non-linearity response and the energy resolution of the EMCal mini-module is studied. Finally the shower shapes of electrons and hadrons are investigated, in order to ultimately try to optimize the particle identification step for the analysis. The SPS setup of the mini-module along with beam line elements is illustrated in Figure 3.4. A similar setup was used for the PS beam.

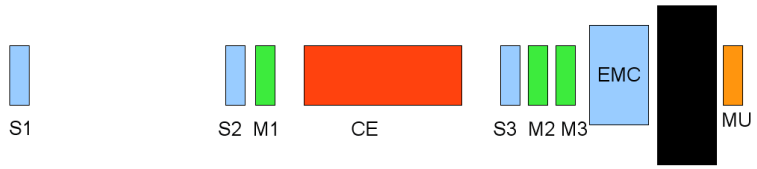

Figure 3.4: The ALICE EMCal mini-module (EMC) at the SPS test beam setup. The beam enters from the left and Mx are magnets for the beam line, Sx are x-y detectors and CE is the Cherenkov detector to purify the beam. The black rectangle behind the mini-module is absorber for the muon detector (MU) in the back.

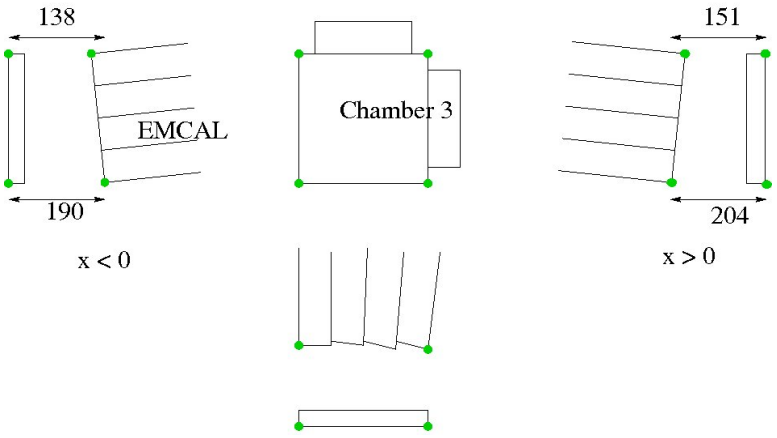

Figure 3.5: The EMCal mini-module. The top row of illustrations are, from left, right side view, top view and left side view. The bottom illustration is the top view, where the gradual leaning of towers as a function of η can be seen.

3.3.1 The EMCal mini-module

For the calibration and commissioning of the ALICE EMCal a mini-module was built resembling a 8×8 tower section of a full EMCal super module. This mini-module was built to have the exact same geometric properties, such as size, tilt of towers as a function of η etc., as the same 8×8 tower segment of the SM built for the ALICE detector. A sketch of the mini-module can be seen in Figure 3.5. 8×8 towers are sufficient to study the response of electrons and hadrons, and the resulting electron showers, since most showers have a maximum radius of about 2-3 towers. The towers used in the mini-module were also built according to the specifications of the EMCal, see Table 3.2.

The mini-module was subjected to test beam on two occasions; 2010 with (secondary) beam from the PS, and with (also secondary) beam from the SPS accelerator in 2010. The setups of the two test beam measurements were similar; protons were

Table 3.2: Mini-module physical parameters

Quantity	Value
Tower Size (at η=0)	6.0 x 6.0 x 24.6 cm^3
Thickness Pb Absorber	1.44 mm
Thickness Scintillator	1.76 mm
Number of Layers	77
Effective Radiation Length X_0	12.3 mm
Effective Molière Radius R_M	3.2 cm
Effective Density	5.68 g/cm^2
Number of Radiation Lengths	20.1 X_0
Number of Towers	8 x 8 = 64

accelerated and collided with a target that produced a wide range of particles at different energies. Particle type and momentum could be selected by using a setup of magnets and other detectors. PS data was taken in discrete momentum steps from 0.5 GeV/c to 8 GeV/c, both electrons and hadrons. For the SPS setup data were taken from incident particles with momentum ranging from 10 to 250 GeV/c. A careful calibration had to be done in order to analyze the data. After a calibration was performed the non-linearity correction curve was obtained. As discussed above, the main deviations from the linear behavior are mainly caused by different interaction processes at low energy and shower leakage at high energies.

Calibration of the mini-module

Although the same mini-module was used for both of the test beam sessions, external conditions such as temperature and slightly different electronic-readouts made the two setups different. Therefore two sets of calibration constants were obtained. For most energies the incident beam was only incident at the center of the detector. However, the beam needed to be swept across all towers in order to calibrate the full module. Such full-tower data were taken for three energies, 6 GeV electrons from the PS beam and 10 and 50 GeV electrons from the SPS beam.

The standard method to calibrate a detector is, as previously mentioned, to study the response when known particles of known energy interact with the detector. Normally minimum ionizing particles (MIPs) are used if one does not have the luxury of an accelerator. This MIP calibration was performed on the full EMCal before it was inserted into ALICE. For the mini-module however, we had access to different

particles over a wide range of momentum. This section describes a self-developed method that was used as an attempt to calibrate the mini-module by using electrons.

The calibration coefficient is defined to be the coefficient that the detector response is multiplied with in order to convert the response into energy, i.e. $E = cX$, where E is the actual particle energy, c is the calibration coefficient (sometimes calibration constant) and X the signal from the detector. When an electron with a known energy hits the mini-module it will be absorbed which creates an electron shower. If the entire electron shower is contained in one tower, the calibration factor is given directly tower by tower. To average out statistical fluctuations many electrons must be detected. The response signal will manifest itself as a peak in a plotted histogram of the measured response and is a direct result from the mono-energetic electrons. This (Gaussian fitted) peak maximum is at the incident electron energy, thus c can be calculated.

If the cells in the calorimeter do not contain the entire shower some additional work needs to be done in order to obtain the calibration coefficients. One way to do this is to parameterize how much of the shower is on average lost from the main tower, i.e. the ratio of the incident tower energy and the incident energy of the particle. This works well if the geometry and Molière radius R_M of the calorimeter are known. It also requires the beam to be centered at a cell, and not displaced. For the ALICE EMCal $R_M = 3.5$ cm, which is roughly the dimension of one tower, thus a first approximation would be that about 90% of the energy of the incident electron is contained within one cell. The calibration constants can then be calculated by measuring the response of each tower when the beam is incident on the center of the individual towers. The summed energy of the cells in one cluster multiplied by the calibration constants should sum up to the energy of the original electron, and this can then be used as a test that the fraction of energy contained within one tower was correctly chosen.

This, however, requires an iterative and empirical process where one tries to assign a fraction to the whole system in order to obtain the optimal result as a whole. It is also sensitive to many circumstances such as if the electron were not centered on one tower, the clustering algorithm, the tilt of towers, etc. Instead of assigning a ratio and iterating until a satisfying result is obtained, another approach was tried. Using a linear model of the cells in the mini-module, one can postulate that the sum of the individual cells signal multiplied by its unique calibration constant will add up precisely to the original incident electron energy. The one dimensional (one tower) problem has already been dealt with, the next step is the two dimensional problem. Consider a calorimeter with two towers with each a unique detector response (i.e.

calibration constant) labeled a and b respectively. The cells absorb all the energy of the electron incident perpendicular to the calorimeter surface with a momentum of 10 GeV/c. The resulting combined output signal that the tower signals should sum to is precisely 10 GeV, which is each tower response multiplied with the respective calibration constant c_1 and c_2:

$$a \cdot c_1 + b \cdot c_2 = 10\,GeV. \tag{3.6}$$

The calibration constants are unknown, but with simple linear algebra the system can be solved explicitly by considering two separate events. For example, imagine that in the first event the response from the two towers were 8 and 2 respectively, and in the next event 4 and 6 was measured:

$$8 \cdot c_1 + 2 \cdot c_2 = 10\,GeV, \tag{3.7}$$

$$4 \cdot c_1 + 6 \cdot c_2 = 10\,GeV. \tag{3.8}$$

This system is trivial to solve. If there are more than two events, say N events, then one has to minimize the error from all the N events combined. This can be thought of as a two dimensional fit; each equation describes a line in 2D space, and the constants c_1 and c_2 that minimizes the total error of N events should be computed. More formally the sum of the different N equations describing each event should be constructed, and the derivative with respect to c_1 and c_2 should be zero. The solution to these two equations gives the c_1 and c_2 that minimizes the total error. Since this method per definition minimizes the spread of the reconstructed cluster energy, plotting the reconstructed cluster energy in a histogram will yield a Gaussian with minimal σ.

Since the one and two dimensional cases have been solved, one can now generalize to a detector of any size, in this case to a 64-dimensional problem for a 8 $\times$ 8 tower detector. Instead of taking derivatives it is easier to form a N$\times$64 matrix A representing the measured values, and solving the equation $Ax = B$, where x is a 64-row vector representing the calibration constants and B is a N-row vector representing the incident electron energy. The solution of this equation can be found numerically by using standard matrix routines found in mathematical software, such as Matlab [101].

The tools for solving this problem are in place, but one important thing remains; how does one define the cluster that resulted from the electron, i.e. towers involved

in the event? Normally for an event in the mini-module one would have an electron incident perpendicular to the detector surface, creating a shower in the detector and a few towers will register deposited energy. In most cases most of the energy is located in the center tower, and the nearby towers have decreasingly less deposited energy as the distance from the impact increases. In the same event one can also have random towers showing small amounts of deposited energy, either from other particles or random fluctuations. The problem is then to distinguish between random fluctuations from towers that are just far away from the impact of the electron (having only a small fraction of the energy deposited). As a first approximation one can assign the whole mini-module as the total energy, summing up an 8×8 cluster. This of course includes random noise of the individual cells, adding unnecessary noise. On the other hand by doing this one can ignore any dependence on clustering algorithms, and all the parameters associated with it. At first a serious attempt was made with 8×8 clusters, but ultimately a realistic clustering tool that is used in the full ALICE EMCal was employed. This is described next.

Clustering algorithms

There are many candidates for algorithms performing the clustering of cells into clusters within the ALICE experiment. Clustering algorithms have been around for quite some time and they are all based on a set of simple rules. The two simplest of the standard algorithms found in AliROOT were used to define the towers included into the electron shower in this analysis. The two algorithms are called "v1" and "3×3" clusterizers. The v1 (version 1) algorithm starts with sorting the tower list in decreasing order according to tower response (seed tower), highest tower on top. The four closest neighbors (in a square lattice) are added to the tower with the largest response, if a signal is present. The algorithm will then move on to the newly added neighbors and check their closest neighbors, and if a signal is present it will add them as well. It will continue doing so until there are no more neighboring towers with signals, or in the worst case, no more cells to add. See Figure 3.6 (Left) for an example of a real electron shower event in the mini-module, along with the cluster generated by the v1 clusterizer. As always there are advantages and disadvantages with this algorithm. An advantage is that the clusterizer has a variable radius and will expand its radius in order to cover the entire cluster. A disadvantage is that it can potentially grow to infinity, or the whole detector, creating mega-clusters. This can be avoided by setting geometrical limits to the algorithm. Enter the 3×3 clusterizer, which just adds the 8 closest neighbors, if signal is present, in order to form a 3×3

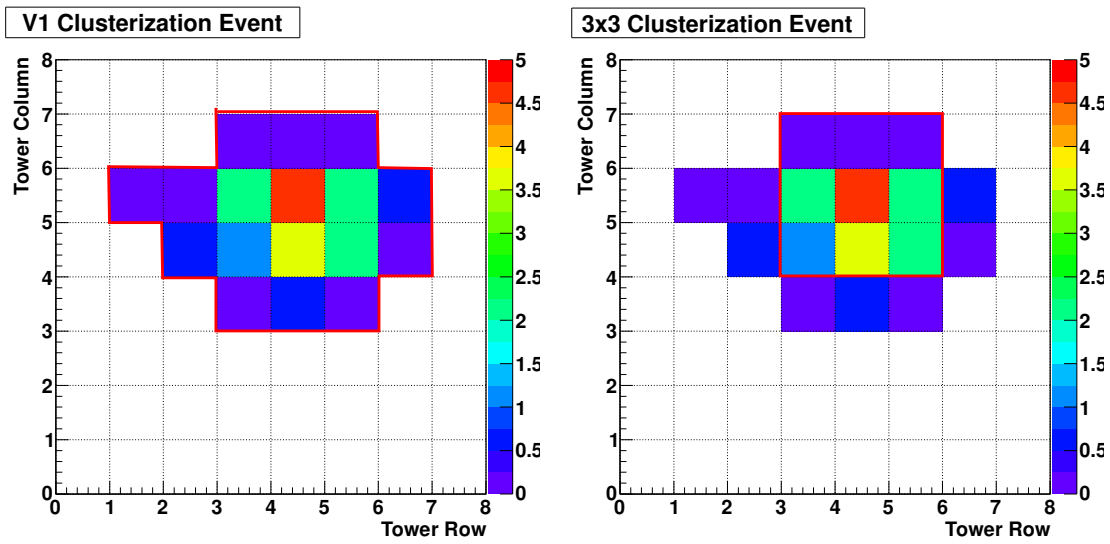

Figure 3.6: Left: The V1 clusterizer adds the four closest neighbors for each cell in the cluster. In this event the V1 clusterizer will sum all the active towers, forming one cluster. Right: 3 × 3 clusterizer. It adds the closest 8 cells surrounding the most energetic cell to form a 3 by 3 cluster.

tower cluster, see Figure 3.6 (Right). This works well for electrons at most energies, but when the shower starts to grow (as it does for some hadrons) this method will miss some towers and end up with a cluster sum, which is less than that of the incident particle energy, and leave residual clusters. These are two very basic clusterizers and there are many more, some involving advanced merging and splitting techniques for dealing with partially merged clusters. However, for the relatively simple test beam setup, these two algorithms are deemed adequate.

Event selection and calibration

Having dealt with defining the towers involved in a shower, and having a method to calculate the calibration constants, the event selection and statistical aspect of the calculation need to be clarified.

Hot, or malfunctioning, towers pose a serious problem to the calibration by distorting clusterization or giving a false response. Hot towers can be spotted by looking at raw response signals of the towers compared to the average tower; hot towers will have significantly higher signal response than the other towers, and on average register much more deposited energy. There were no hot towers present in the mini-module.

A malfunctioning cell, or bad cell, can be detected by looking at the χ^2 variable of the response (ADC) fit for the cell. A bad fit indicate deviations from the usual

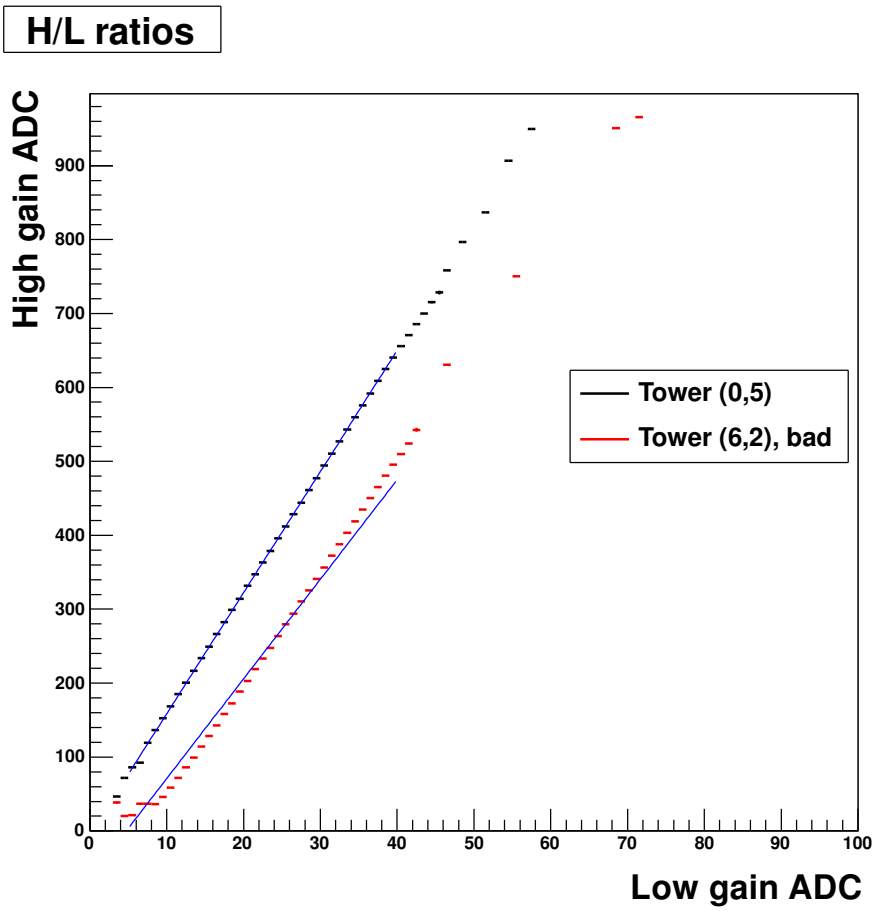

Figure 3.7: This shows a 2D plot of high and low channel signals for two towers in the test beam mini-module. The blue H/L ratio of tower (0,5) is a normal tower with a linear relationship between the low gain and high gain channel. The red H/L ratio of tower (6,2) shows some non-linearity at low ADC counts on the high-gain channel. This tower was excluded.

shape of the signal, thus larger χ^2. Additionally each tower in the calorimeter has two channels, one high gain and one with low gain. The high gain channel works up to about 15 GeV while the low gain channel can register deposits up to hundreds of GeV. Looking at a 2D histogram of the two channels they should display a linear behavior (until the high gain channel is saturated above $\sim$15 GeV). If there are deviations from a linear behavior then the channel is likely to be bad and the tower should be excluded. In studying these high-to-low gain 2D histograms one such tower was found. It had a bad high gain channel which can be seen by looking the high-to-low gain channel ratio, see Figure 3.7.

The 28 towers at the edge of the detector also pose a problem. Given that they are at the edge there is always a potential unknown fraction of the shower that escapes the

detector outwards, the four corner towers even more so. This means that the towers at the edge of the detector can never really be calibrated explicitly unless one performs a full calibration sweeping each individual tower with the electron beam, switches the edge towers with some of the innermost towers and repeats a full calibration. This is rather time consuming so one usually accepts this fact and considers the edge towers to be present only to provide calibration for the innermost cells. Since the test beam mini-module was a 8×8 tower calorimeter, only the innermost 6×6 cells could be calibrated properly.

The final problem to consider is the issue of proper, or even, statistics. Since the method used for solving for the calibration constant is statistical, each event receives a weight in the equation. If by some circumstance one particular cell is over (or under) represented it will be given an unfair weight. If there are one million events where one tower delivers a response only once and another tower is active for the remaining events, then the tower only represented a single time can be anything since its weight in the calculation is very small. It is therefore important to have an even statistical sample, where the relevant towers are represented evenly in the matrix equation $Ax = B$. The events were selected to represent the inner 6×6 towers in an equal and fair manner. Only data from the high gain channels were used in the calibration. By making use of the high-to-low gain correlation, the low gain channel calibration factor can be determined.

That the sample is even will represent itself in the estimated error (obtained from Matlab matrix equation solver routines) of the calibration constants. These can be seen for all 64 towers in Figure 3.8 when the matrix equation was solved for the full mini-module. Since events where the innermost 6×6 towers were selected, the edge towers are only sampled or activated if a nearby cluster happens to leak energy to it. This is the only way that the edge clusters are included when solving for the calibration constants. The weight for these towers in the matrix equation is therefore skewed, thus one can expect that the calibration constants for the edge towers are bad. This also manifests itself in the estimated error of the calibration constants, see Figure 3.8, where the edge towers are at tower index 0-8, 15-16, 23-24, 31-32, 39-40, 47-48 and 55-63, having larger estimated error. The four corner towers can also be seen with higher estimated errors (tower 58 is not a corner tower but has a large error due to low statistics). The errors and the calibration constants for the 6×6 innermost towers seem to have a small errors and stable calibration constants. Assuming that the calibration constants in the inner 6×6 sections were relatively reasonable, the not-so-precise calibration constants of the edge could possibly affect

the whole calculation, dragging the innermost towers' calibration constants away from their true value. The edge had to be removed from the equation somehow.

This was solved by first looking at the single tower raw ADC spectrum (essentially raw tower response). By taking the product of the calibration constant with the ADC value of the electron peak in a single tower (at slightly less than the electron energy due to shower leakage) one will end up with a value; the energy contained within the most energetic tower in the cluster. This should on average correspond to the ratio described above, which at first was estimated to be connected to the Molière radius R_M, i.e. about 0.9, and therefore be somewhat constant. By taking an average of the innermost towers one can effectively calculate this ratio. This ratio should be the same for any tower, provided that one has data for the tower when it had electrons incident at the center of the tower. Since this data were available the correct calibration factors for the edge could be calculated from the raw ADC histograms.

Having reasonable calibration constants for the edge one can get rid of the dependence of the edge towers in the calculation by subtracting the "leaked" energy: if a shower on the edge of the 6×6 activates some towers on the 8×8 edge, then this leaked energy was estimated using the response from the 8×8 edge towers and their respective calibration constants. This estimated leaked energy was subsequently subtracted from the incident electron energy, i.e. B in the matrix equation. This effectively reduces the problem to a 36 dimensional space and the effect of the edge is removed.

Rerunning the calculation for the 6×6 section with the edge subtracted yielded good constants for the 36 innermost towers. Yet again one can do an iterative calculation of the edges by using the non-edge tower calibration constants to recalculate the edge calibration constants, which was done. After one iteration the calibration constants in the 6×6 section did not change much and a set of calibration constants was obtained.

High to low gain ratios

When a set of calibration constants for the high-gain channels has been obtained the low-gain channel calibration constants remained. The high-gain channels have a resolution of 1024 ADC counts, with each ADC count corresponding to ∼16 MeV. Measuring past ∼15 GeV means that the high-gain channels will be saturated and the low-gain channels must be used. The low-gain channels are not as sensitive as the high-gain channels, thus performing a calibration to obtain the calibration constants using low-gain channels is difficult. It was tried but abandoned in lieu of a better

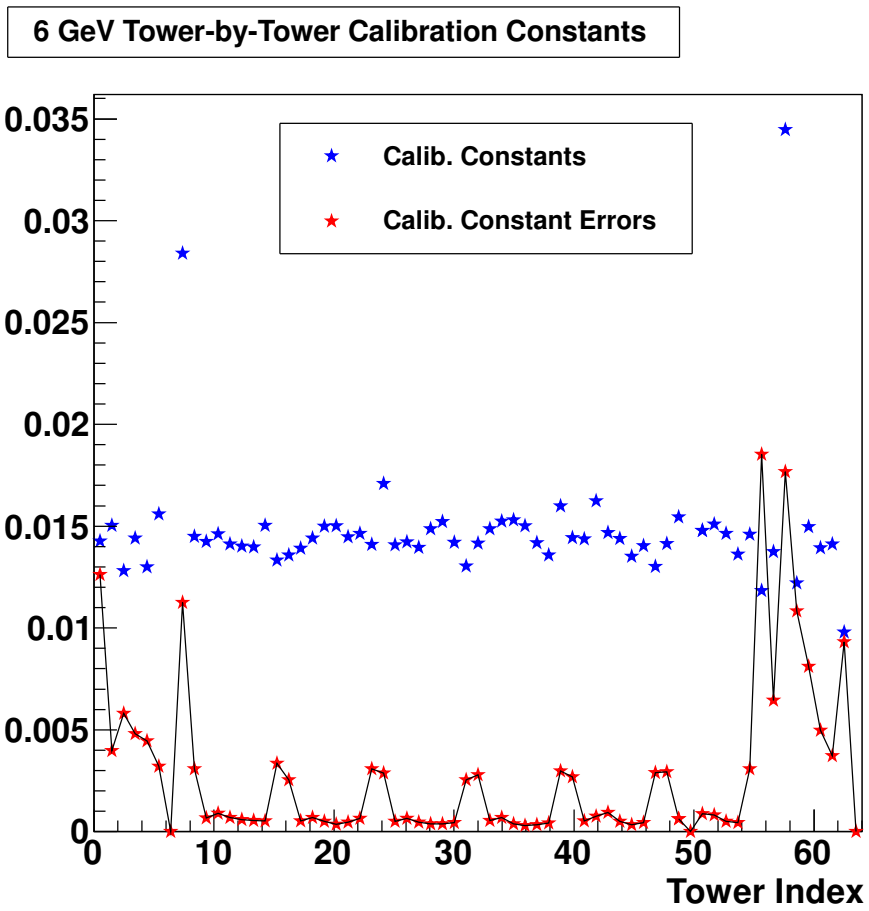

Figure 3.8: Calibration factors, along with associated error for solving for the 64 calibration constants without removing edge clusters. Note that two towers are excluded, i.e. the calibration constant is set to 0 (tower 6 and 50).

approach. Instead one takes a run where there are full statistics for each tower and plots a scatter plot of the high-gain signal versus the low-gain signal for all events. If the tower is linear and works as expected, a straight line will be observed. This can then be fitted with a first order polynomial fit and the slope of this line will be the high-to-low ratio. This was done on the 10 GeV SPS data, since both channels are active in this energy range. For the 6 GeV PS data the high-to-low ratios were not needed since the high gain channel never goes out of range. A fit of such a tower can be seen in Figure 3.7, along with one bad tower.

3.3.2 Non-linearity and energy resolution

The non-linearity of a calorimeter as discussed previously is due to several different processes and is more pronounced at low and high energies. When the energy is low, the effects of ionization will play an important role. The effect is that the observed response in the calorimeter will be less than for mid-range energies, i.e. the constant Bremsstrahlung interaction region. As the energy is increased the shower will be extended deeper into the calorimeter. At some point the shower will leak out at the back of the calorimeter. This causes the energy measured to be smaller than the actual incident energy. There are of course other processes involved, but all these effects combined are called the non-linearity, meaning deviation from linear behavior. Countless papers and books have been written about this topic, but the main method for obtaining the non-linearity correction curve is to look at the response of the detector when a known particle with a known energy is incident. The energy of the incident particle is then varied and the response of the detector is observed and parameterized as a function of energy. Taking test beam data at the PS and SPS yielded an electron response ranging from 0.5 to 200 GeV, this is well within the expected operational range of the calorimeter. Assuming that a proper calibration of the device has been done, the energy of the incoming electrons for the different energies is reconstructed and a Gaussian function is fitted to this reconstructed energy peak. The maximum of the peak is then compared to the incident particle energy. In most of the region it is linear, i.e. 1:1 and this flat plateau region serves as a point of normalization. A function of the form

$$f(x) = p[0] \cdot \frac{1}{1 + e^{-x/p[2]}} \cdot \frac{1}{1 + p[3] \cdot e^{(x-p[4])/p[5]}}, \tag{3.9}$$

can be fitted [102], and the resulting fit with data points can be seen in Figure 3.9 using both clusterizers. This non-linearity function is then implemented by the

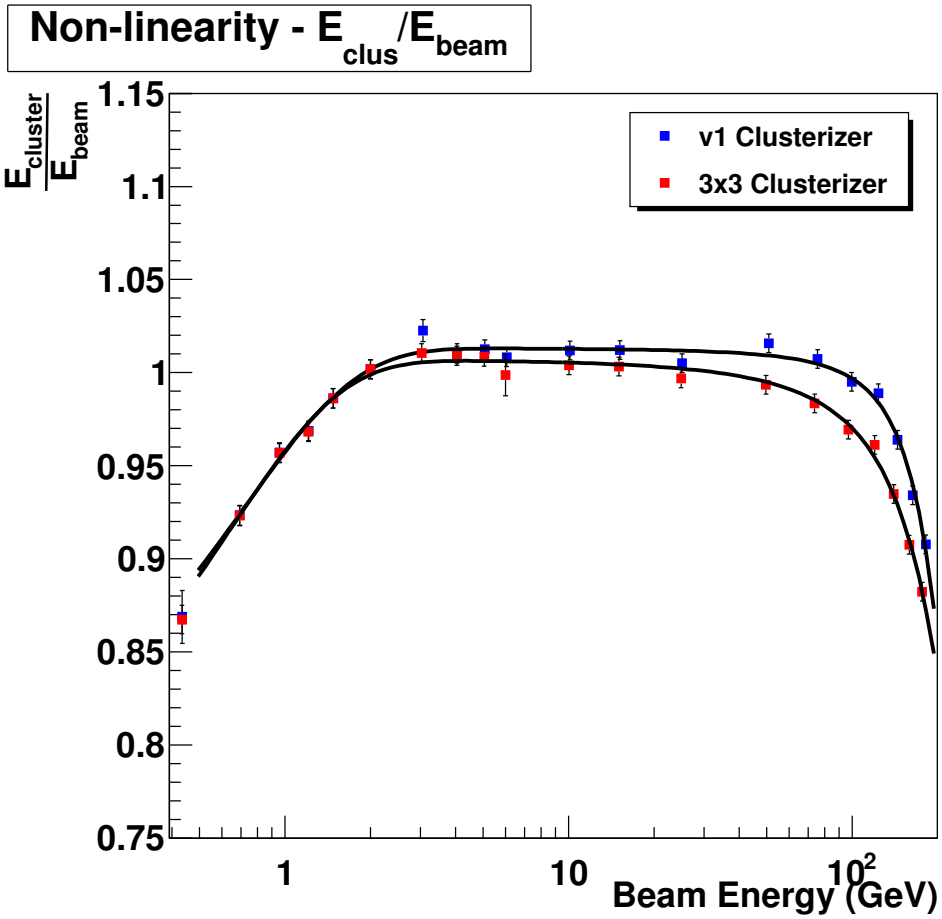

Figure 3.9: The non-linear response of the mini-module. The data points correspond to the measurement using two different clusterizers, v1 and 3×3. As expected at higher energies the 3×3 clusterizer will on average lose more energy than the v1 (due to increased spread of showers).

clusterizer to compensate for non-linear effects.

Having studied the response of the reconstructed clusters, having fitted the reconstructed energy with a Gaussian, one can now measure the energy resolution as the width of the corresponding Gaussian as a function of energy. The result along with a simulation is shown in Figure 3.2.

3.3.3 Shower shape studies and particle identification

Finally when a good set of calibration constants has been obtained, and a method for dealing with the non-linearity is in place, one can start to perform physical measurements with the calorimeter. One goal for this investigation was to study shower shapes of electrons and hadrons. The purpose being to investigate whether shower

shapes of clusters can be used as a complement in electron identification, or rather hadron rejection. So far only electrons have been used for calibration and non-linearity studies, but data from hadrons were also recorded, ranging from 0.5 GeV up to 250 GeV. This in addition to electron data gives an excellent platform for developing and studying different methods of electron identification; mainly pion rejection.

The production rate of hadrons to electrons for a typical pp run in the ALICE detector is roughly 100:1, [99]. Since electrons carry information about many interesting processes regarding the collision it is therefore important to be able to select these electrons, which mainly requires the rejection of pions. A variety of methods exist to distinguish electrons from pions. Among them, the shapes of showers created by electrons and hadrons in a calorimeter are different. The difference in shower shapes arises from the physics that governs how the different particles interact with the calorimeter. The characteristic parameters that distinguish the interactions are the radiation length X_0 and the nuclear interaction length λ_{int}. Electron interaction is, as described above, mainly dependent on X_0 while pion (hadron) interaction is mainly governed by λ_{int}. The largest difference in shower shapes occurs within material that has a large difference in these parameters. This difference generally increases with increasing atomic number Z. Heavy materials frequently used in calorimeters are iron, lead, tungsten and uranium. In the ALICE EMCal lead is used as absorber material. For some materials it is possible for the scintillator also to act as absorber material, such as the tungsten crystals in the PHOS detector [103]. If a material with different X_0 and λ_{int} is used one can observe very different shower structures for electrons and pions. In the longitudinal plane the electron tends to go deeper in a more focused shower, while the pion shower is more shallow but on average the shower develops (begins) deeper within the detector. Depth of showers is an excellent parameter to distinguish pions from electrons, however since the ALICE EMCal does not have longitudinal information, this technique is not available to reject pions. Shower shape parameters to distinguish electrons from pions are lateral shower shapes & dispersion of clusters, time structure of signals, K-factor and ξ-parameter, which are all explained in subsequent sections. Finally the E/p ratio, the main parameter for electron identification, is discussed.

In order to determine how effective a parameter is at distinguishing an electron from a pion, the rejection factor of hadrons was used as an indicator [104]. Rejection is defined as

$$R_{Hadrons} = \frac{N_{Hadrons}}{N_{Cut}}, \tag{3.10}$$

where $N_{Hadrons}$ is the number of all the hadrons in the sample and N_{Cut} is the number of hadrons (out of $N_{hadrons}$) that survive the electron efficiency cut. The electron efficiency cut is then up for debate, and this cut is a statement of how efficient the electron selection is. For this study the electron efficiency cut is defined to be where 90% of the electrons are included within the cut. The issue is then to find for each parameter where to place the electron cut in order to include 90% of all the electrons. The resulting hadron rejection is thus independent of the ratio of hadrons versus electrons, which is needed to perform a fair comparison of different parameters.

Lateral shower shapes

The lateral shower shape can be calculated if the granularity of the calorimeter is fine enough, i.e the size of a cell should be small enough not to contain the entire shower. The first and simplest parameter is the R_p parameter where the cells in a cluster are added with a weight according to distance from the mean position:

$$R_p = \frac{\sum_i r_i E_i}{\sum_i Ei}, \tag{3.11}$$

where E_i is the energy deposited in cell i and r_i is the distance from the i^{th} cell to the calculated center of gravity of the shower according to (for each coordinate):

$$\bar{X} = \frac{\sum_i w_i x_i}{\sum_i w_i}, \tag{3.12}$$

where x_i is the coordinate in one dimension of each cell and $w_i = E_i/E_T$ where E_T is the total energy of the cluster. This works well for most cases for fine granularity. R_p is shown in Figure 3.10. However this breaks down when the granularity of the calorimeter is coarse (comparable to the Molière radius), as for the EMCal. Instead of the R-factor one uses dispersion. Since the center of gravity will be dependent on the geometry of the granularity, in order to account for the exponential falloff of the shower energy distribution as a function of distance, see [102], one introduces a log factor so that

$$w_i = max\left(0, \left[W_0 + ln\left(\frac{E_i}{E_T}\right)\right]\right), \tag{3.13}$$

where E_i/E_T is the i^{th} tower's energy over total cluster energy, and W_0 is a free parameter. The W_0 is dependent on the calorimeter and is set to 4.5 for the ALICE EMCal [102].

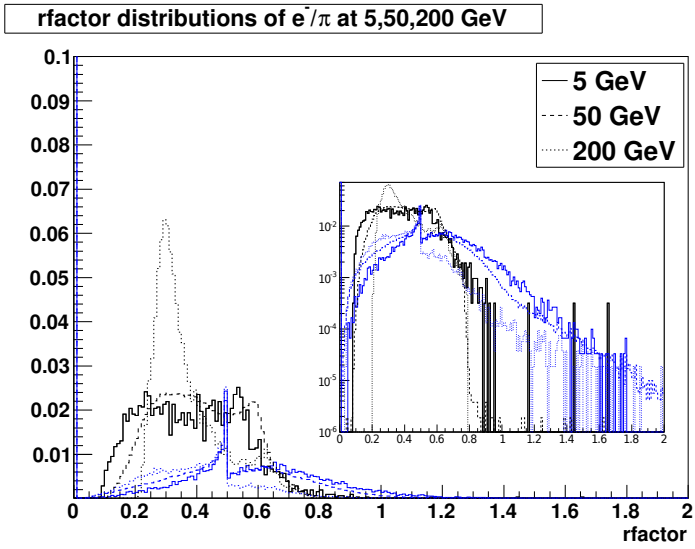

Figure 3.10: This shows R_p for electrons and hadrons at different momenta. Electrons in black, hadrons in blue. The inset contains the same figure but with a logarithmic vertical axis.

The dispersion around the x-axis can then be calculated as

$$D_x^2 = \frac{\sum_i w_i x_i^2}{\sum_i w_i} - \left(\frac{\sum_i w_i x_i}{\sum_i w_i}\right)^2 = \overline{x^2} - \overline{x}^2, \tag{3.14}$$

and the combined dispersion is given by $D = \sqrt{D_x^2 + D_y^2}$. The dispersion of a cluster is a measure of how much the cluster is spread away from the center tower in the lateral plane.

Since 90% of the energy of the shower for an electron is contained within a radius of $\sim 1\ R_M$, the rest leaks to the surrounding cells. A cluster formed by the clustering algorithm will have a certain spread and shape. By adding up the cells together as moments of inertia, using cell energy and distance to the center cell as parameters, one can fit an ellipse and define the two major axis as shower shape parameters. They are defined as

$$M_{02} = \frac{1}{2}\sum_i E_i(x_i^2 + y_i^2) + \sqrt{\frac{1}{4}\left(\sum_i (x_i^2 + y_i^2)^2\right) + \left(\sum_i E_i x_i y_i\right)^2}, \tag{3.15}$$

$$M_{20} = \frac{1}{2}\sum_i E_i(x_i^2 + y_i^2) - \sqrt{\frac{1}{4}\left(\sum_i (x_i^2 + y_i^2)^2\right) + \left(\sum_i E_i x_i y_i\right)^2}. \tag{3.16}$$

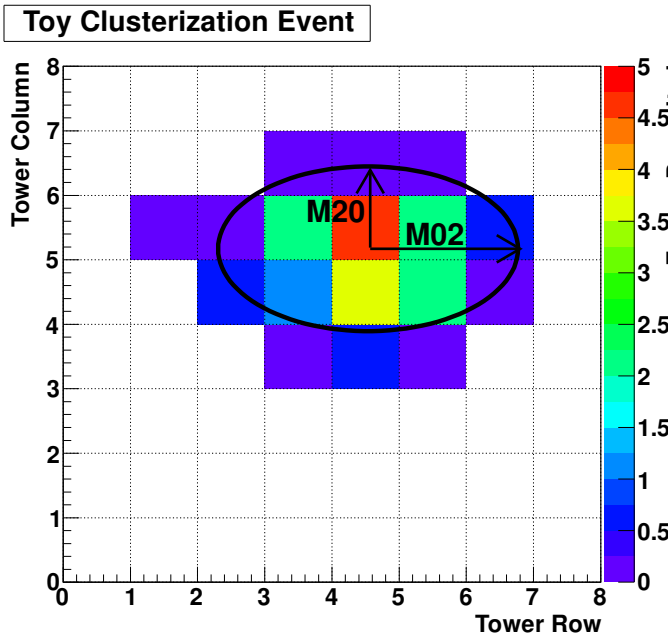

Figure 3.11: This figure shows a cluster in the mini-module generated by an electron. An ellipse is fitted and the two axes are labeled M02 and M20.

These two parameters can be seen for an example cluster in Figure 3.11. These along with dispersion D is commonly used within the ALICE collaboration. The distribution of these parameters for electrons and hadrons can be seen in Figures 3.12.

Containment parameter

The containment parameter is defined as

$$C = \frac{\sum_{i=1}^{n} E_i}{E_T} \tag{3.17}$$

where the sum is over n towers within the cluster, E_i is the tower energy and $E_T i$ is the total cluster energy. n is a free parameter but for most studies it is enough to check the case where $n = 1$, i.e. the energy of the tower with the most deposited energy over the total cluster energy

$$C = \frac{E_1}{E_T}. \tag{3.18}$$

This ratio is the same as the ratio discussed in the calibration of the mini-module, and is closely related to the Molière radius for electrons. It peaks at about 0.8-0.9

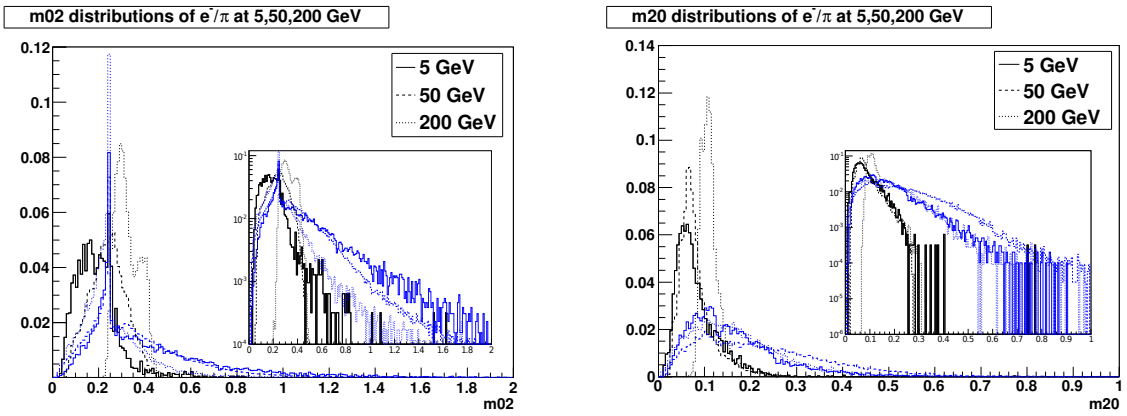

Figure 3.12: This shows the M02 (Right) and the M20 (Left) parameter for electrons and hadrons at different momenta. Electrons in black, hadrons in blue. Inlays show parameters in logarithmic y-axis.

and is fairly constant with energy. For hadrons this ratio is more evenly distributed. See Figure 3.13.

K-factor

The K-factor is defined by

$$K = \sum_i r_i [E_i/E_T - f(r_i)]^2, \tag{3.19}$$

where the function $f(r_i)$ describes the fraction of energy deposited in a cell at distance r_i from the center of the cluster for an ideal electron shower. The K-factor is then a comparison of how "electron like" the shower is. For an ideal electron the K-factor is zero. In order to compute this parameter the reference function $f(r_i)$ had to be obtained for electrons. These were obtained from the electron data by studying the shower shape of electrons and fitting a function to this, see Figure 3.14. This is then compared to an unknown cluster and ideally electrons should yield small K-factor, while hadrons should have larger K-factor. However, it is difficult to distinguish between hadrons and electrons since one cannot measure the full shape of the hadron showers in the mini-module due to the limited depth of the calorimeter. The corresponding hadron $f(r_i)$ can be seen in Figure 3.15. The resulting parameter presented in Figure 3.16.

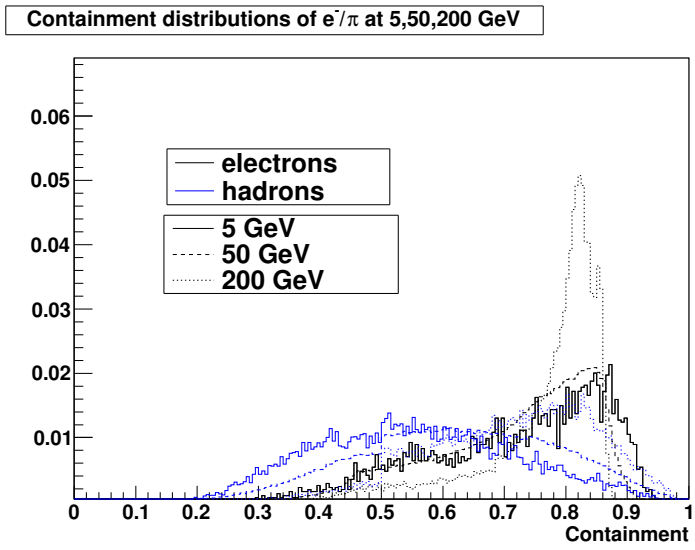

Figure 3.13: The containment parameter for electron and hadron showers for different momenta.

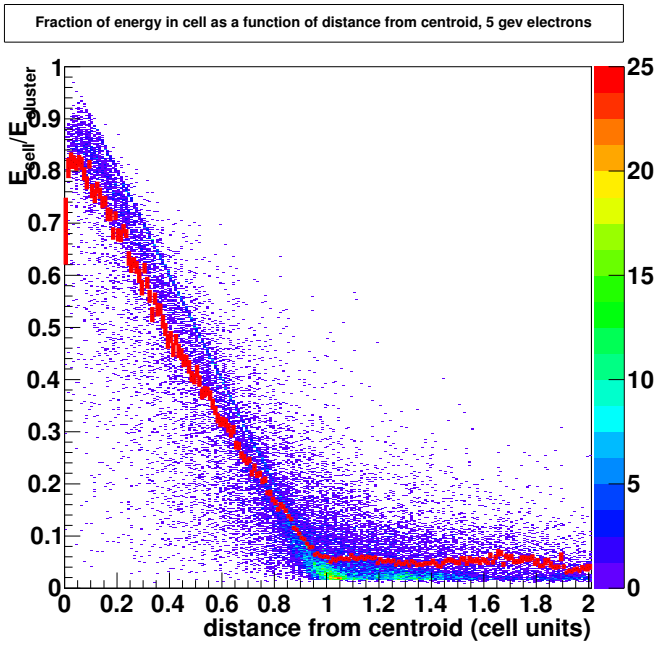

Figure 3.14: This figure shows the cluster energy (ratio) distribution as a function of distance from the center of the cluster for electrons. This data were obtained from 5 GeV electrons incident on the EMCal mini-module. The red band is the mean.

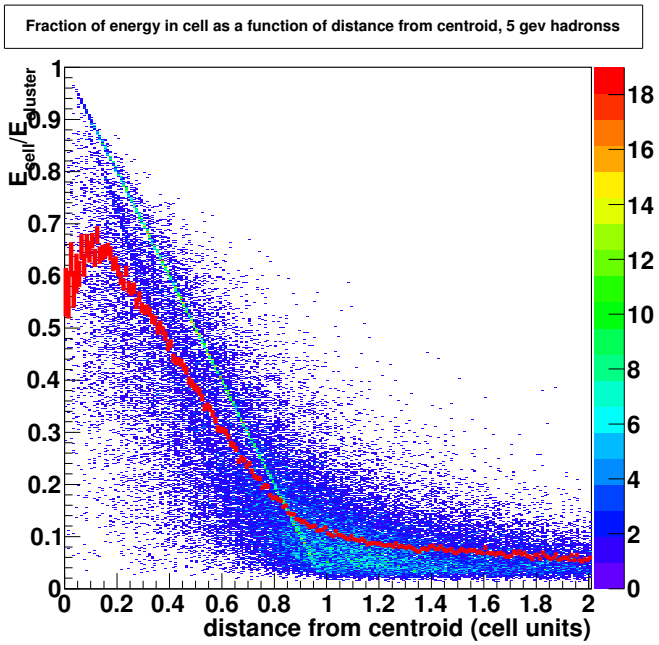

Figure 3.15: This figure shows the cluster energy (ratio) distribution as a function of distance from the center of the cluster for hadrons. This data were obtained from 5 GeV pions incident on the EMCal mini-module. The red band is the mean.

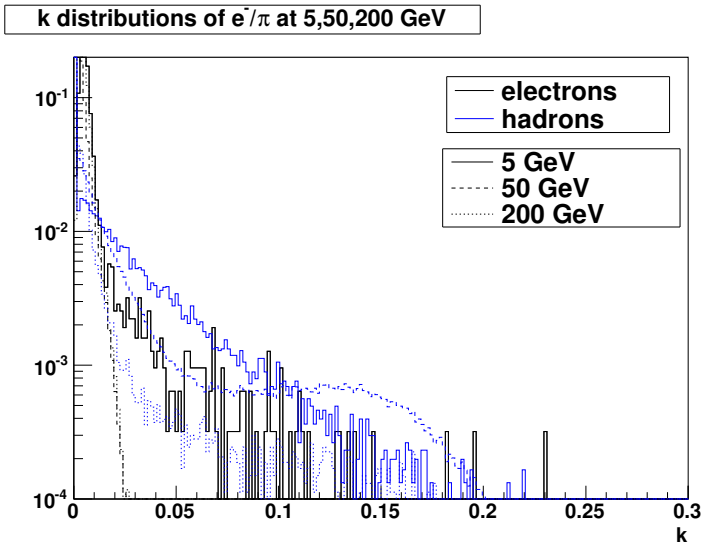

Figure 3.16: The K-factor parameter for electron and hadron showers for different momenta.

E/p discrimination

For the final ξ parameter a few words about the main ALICE EMCal electron identification method should be said, the reason will become apparent later. In general one can make use of other detectors within an experiment and combine information from these detectors with the calorimeter in order to reject hadrons. The momentum of the particle can be measured by magnetic spectroscopy of the inner tracking detectors, a combination of the ITS and TPC. The ratio of the cluster energy of an EMCal cluster versus the measured particle momentum, E/p, is an effective measure to reject hadrons. This is the main discriminator in the ALICE experiment to detect electrons at high transverse momentum.

Forming the fraction of measured particle energy over measured particle momentum is the most prominent discriminator of electrons and photons versus minimum ionizing particles (MIPs), such as hadrons and muons. As discussed previously, due to the interaction properties of electrons and photons with the calorimeter, the electron and photon deposits most or all of its energy into the calorimeter. By measuring the momentum of the particle through other means (magnetic spectroscopy in ALICE), the E/p fraction should be close to unity for electrons and photons. MIPs deposit only a fraction of this which makes E/p an excellent discriminator between electrons and pions. In Figure 3.17 the E/p fraction is plotted for electrons versus hadrons in the test beam data for three different energies.

ξ-parameter

The ξ-parameter is defined by

$$\xi = \sum_{i,j=1}^{N} (E_i - \overline{E_i}) H_{ij} (E_j - \overline{E_j}), \tag{3.20}$$

where $H_{ij} = M^{-1}$ and

$$M_{ij} = \frac{1}{N} \sum_{n=1}^{N} (E_i^{(n)} - \overline{E_i})(E_j^{(n)} - \overline{E_j}) \tag{3.21}$$

where $E_i^{(n)}$ is the energy observed in the i^{th} tower for the n^{th} event, and $\bar{E}_i$ is the average energy deposited in the i^{th} tower over all the n events. ξ is then a measure of how "electron-like" the shower is. The ξ-factor was developed and used in the SPACAL collaboration and described in [104] and [105]. In the original paper [105] a fixed geometry was used and since the full calorimeter had only 60 cells in total

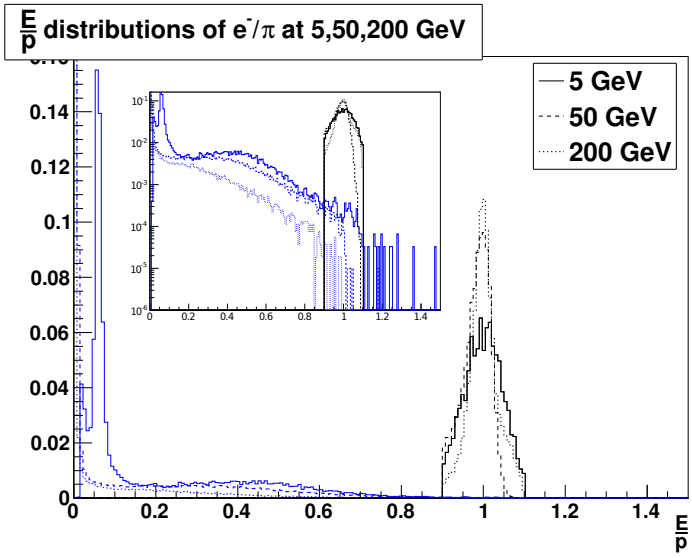

Figure 3.17: This shows E/p for electrons and hadrons at different momentum. Electrons in black, hadrons in blue. In the electron sample there is considerable contamination thus one has to use E/p to actually distinguish an electron from a hadron; the electron peak has been sampled only between 0.8 and 1.1 E/p. This is the definition of an electron in the mini-module study.

the calculations involved were not too complex. To use the same definition of the parameter on the full ALICE EMCal with its 12288 cells it makes the calculation quite elaborate; to perform computations with matrices of that magnitude is computationally very intensive on an event-by-event basis. Therefore, the method was modified and the calculation was mapped from full size physical space to an energy-ordered space. The 64 numbers that describe the cell energies will most of the time be zero since a cluster only has a few cells active. The towers were ordered adding the first entry as the tower with the highest energy, and thereafter with descending energy. By doing this one can reduce the calculations considerably since most of the entries are zero. The ξ parameter can be seen in Figure 3.18. When calculating the rejection of this parameter it turns out to be larger than the rejection of the E/p parameter. Initially there was some confusion why this was the case, however the reason for this was the definition of the ξ-parameter. The SPACAL collaboration had a calorimeter with a depth of about a meter; thus it was more a hadronic calorimeter than an electromagnetic calorimeter. It could absorb the entire hadron shower to obtain information of both electron and hadron showers. The shower shape parameters were the main method to discriminate electrons versus pions. For the ALICE EMCal and the mini-module a 10 GeV electron that deposits an energy of ∼10 GeV was compared

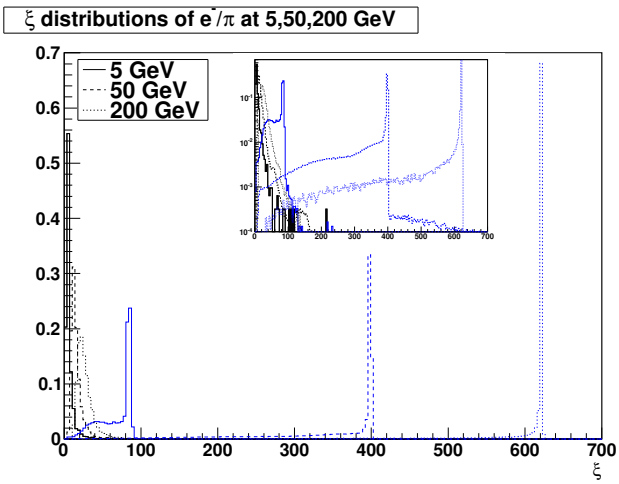

Figure 3.18: This shows ξ for electrons and hadrons at different momenta. Electrons in black, hadrons in blue.

with a 10 GeV hadron that deposits a fraction of 10 GeV. In that step the information about incident momentum is exploited, i.e. essentially E/p. The ξ-parameter is then a combined E/p and shower shape parameter, slightly better than E/p due to some additional information about the shower shape.

Time structure of the signal

Time structure of the signal in the calorimeter can also be used to distinguish electrons from pions since the timing of the electron signal is usually very well defined, with a uniform width. The timing of the pion signal is usually broader, and one can use this to reject pions. This was briefly studied, however the timing signal, to reasonable precision, is not available for the test beam data, thus the effort was without result.

3.3.4 Conclusion

Considerable time was spent investigating the response, calibration, non-linearity and shower shapes of the mini-module. The resulting rejection from the above parameters can be seen in Figure 3.19. The conclusion is that it is possible to slightly clean up the electron sample from contaminating hadrons, but the effect is at the cost of loosing 10% of the electrons (the definition of rejection requires minimum 90% of all electrons). The reason for the ξ parameter having larger rejection than E/p is due to the known incident momentum which essentially discriminates on E/p with some additional information about shower shapes. The lack of a larger benefit is

probably due to the fundamentals of the electromagnetic calorimeter; it fully absorbs electron showers, but only a fraction of hadronic showers. This lack of full information about hadron showers makes it difficult to tell electrons apart from hadrons. The reason the SPACAL collaboration could use the ξ parameter as a very effective electron/pion discriminator is because it was almost a meter thick, turning it into a hadronic calorimeter with full shower information. On the other hand the SPACAL collaboration did not have access to the momentum of the particle which ALICE does thanks to the ITS and the TPC. This provides for an effective pion rejection of a more than a hundred at 5 GeV, which yields a clean sample of electrons as shown in Section 4.3. In the end, shower shape parameterization and discrimination can marginally improve the purity of the sample at a cost of electron identification efficiency. Ultimately E/p is the most efficient parameter that serves as a trustworthy discriminator for identifying electrons. All the above described parameters have been coded into an AliROOT c++ class called AliEMCALClusterParams.cxx. This class is included in the common classes in the ALICE EMCal analysis train. The class takes a cluster and the momentum of the track that is associated to the cluster, and creates an object that can return any of the described shower shape parameters. Shower shape cuts were used in PbPb data where the statistics are plenty and the demand for a clean electron sample is great. For the pp analysis at 2.76 and 7 TeV shower shape cuts have been excluded due to statistics and the topology of pp events which are relatively clean.

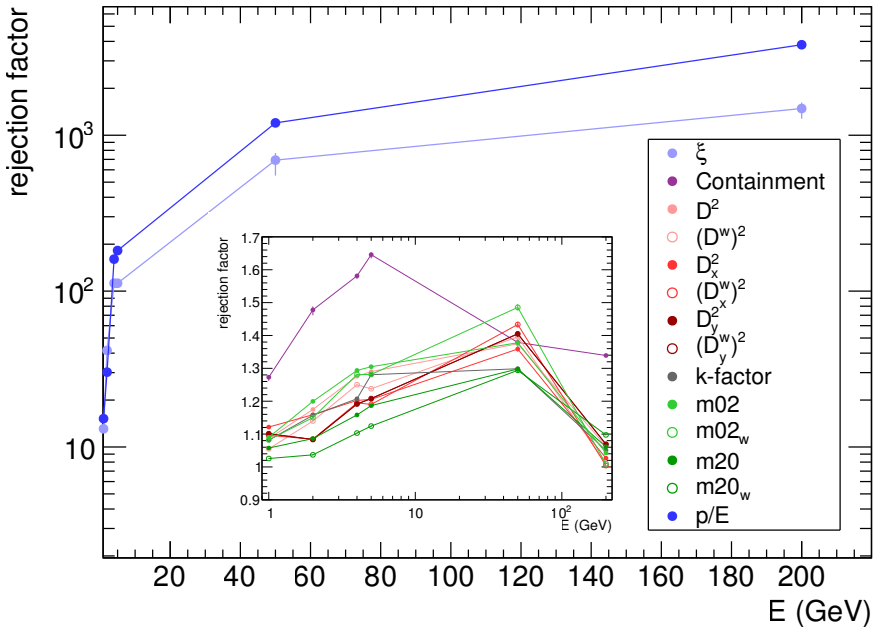

Figure 3.19: Rejection factor for the different shower shape parameters. Inlay shows the shower shape parameters with close to unity rejection. The x-axis is logarithmic. Clearly the E/p parameter is a very efficient discriminator between electrons and hadrons. The ξ is exploiting information about momentum to reach a rejection which is essentially E/p with an added component of shower shape information.

Chapter 4

Analysis of electrons

This chapter describes the electron-level analysis. In order to obtain a good sample of bottom-decay electrons ($e_b^{\pm}$), it is important to first select a pure sample of electrons. The previous chapter has dealt with calorimeters and how to select electrons in a controlled (test beam) environment. In this chapter, the first section describes event selection in 7 TeV proton-proton data. Section 4.2 deals with tracking efficiency, which is determined from Monte-Carlo (MC) simulations. Since tracking efficiency and p_T-unfolding are intertwined, p_T-unfolding is also presented here. In section 4.3 the particle identification steps are described. This includes the usage of TPC-EMCal to select electrons and to calculate the purity and efficiency of the particle identification selection. Finally in section 4.4 the EMCal trigger is described along with the efficiency correction needed to correct for the trigger bias. A summary of all cuts is displayed in Table 4.1.

4.1 Event selection

The data analyzed in this thesis were recorded in the summer of 2011 when the LHC was delivering proton-proton collisions at $\sqrt{s} = 7$ TeV. The period, labeled LHC11d by the ALICE run coordination, recorded about 23 M minimum-bias events, and about 10 M events where the EMCal was used as a trigger, labeled "kEMC7" triggered events. The data were split into *runs*, being separate recordings of collisions, a few minutes to hours in length. Only runs with the ITS-TPC-EMCal detectors active were selected since these detectors are essential for this analysis. As discussed in 2.2.2 the ITS suffered from cooling problems and dead pixels, mainly in the SPD and SSD. The TPC also had problems with the gain of the multi-wire proportional chambers in 90% of the TPC readout regions, resulting in a somewhat degraded tracking and the

Table 4.1: Summary of all cuts used in the electron level analysis.

Measurement	Condition
Run and Trigger Selection	
Runs	156620 $\leq$ run number $\leq$ 159582
Detectors included in runs	ITS, TPC and EMCal
Event Selection	
Triggers selected	kEMC7 (HT) & kINT7 (MB)
L0 EMCal trigger threshold	$\geq$ 4.8 GeV
Vertex z-cut	$\lvert V_z \rvert < 10$ cm
Reject pileup	true
Track Selection (electrons)	
ITS SPD hits	one hit in either layer
ITS total hits	$\geq$ 4 total hits in any layers
Require ITS refit	true
Number of TPC clusters	$\geq$ 100 hits
Accept kink daughters	false
Require TPC refit	true
Track to primary vertex xy-DCA	$\leq$ 3.0 mm
Track to primary vertex z-DCA	$\leq$ 3.0 mm
Ratio of found to findable TPC clusters	$\geq$ 0.6
TPC χ^2/cluster	$\leq$ 4
Electron Selection	
EMCal acceptance ϕ	$79^\circ \leq \phi \leq 191^\circ$
EMCal acceptance η	-0.7 $\leq \eta \leq$ 0.7
Transverse momentum	7.0 $\leq p_T \leq$ 12.0 GeV/c
TPC $n\sigma_e$	-1.5$\leq n\sigma_e \leq$ 3.0
Cluster-track residual	$\Delta\phi < 0.05^\circ$
	$\Delta\eta < 0.025$
EMCal $E_{cluster}/p_{track}$	$0.85 \leq E_{cluster}/p_{track} \leq 1.3$
Trigger Correction	
Clustering algorithm	V1 + unfolding, V2
Reject exotic clusters	$N_{cells} < (1 + E_{cluster}/3)$
Cluster time cut	560 $\leq t \leq$ 620 ns

exclusion of about half of the runs, see more details in the QA section. Within the ALICE data reconstruction framework there is an automated QA analysis software that runs after each run is recorded and reconstructed for the first time, called "pass0". Subsequent reconstructions of the raw data into progressively more fine-tuned analysis data are called pass$n$, where n is the full reconstruction iteration. The QA plots are analyzed and a quality flag is set for the run and pass, which are then posted on-line[1]. If the data are deemed in good condition the run gets assigned a "Global Quality" flag of 1. For all other cases there is a numbering scheme that indicates what seems to be the problem with the specific data set. In some cases the data are bad due to bad reconstruction, which is mostly due to incorrect calibration or problems in the reconstruction code. The next reconstruction of the raw data into progressively more fine-tuned analysis data is then called pass1. For some data sets this goes on until pass4. In other cases where the data are bad due to missing detectors etc., these runs will instead be labeled bad (Global Quality > 1) and will be excluded from analysis. For the LHC11d data 4.8 M minimum-bias events and 5.7 M kEMC7 events from pass1 have Global Quality $= 1$ which come from from 63 runs:

156620 156626 156629 156794 156797 156829 156889 156891 156896 157003 157025 157203 157220 157227 157257 157261 157262 157275 157277 157475 157476 157496 157562 157564 157567 157569 157734 157766 157818 157819 157975 157976 158086 158112 158115 158118 158192 158196 158200 158201 158285 158287 158288 158293 158301 158303 158304 158526 158604 159254 159258 159260 159286 159318 159450 159532 159535 159538 159575 159577 159580 159581 159582.

4.1.1 Off-line event selection

From the above listed runs a set of physics selection criteria were applied, shown in Table 4.2. The physics selection requires the calculated main vertex, called the primary vertex, to be somewhat centered around the defined interaction point([0,0,0] in ALICE coordinates). This is to ensure proper detector coverage, thus good track reconstruction. The cut was set at $|V_z| < 10$ cm. See Figure 4.1 and 4.2 for the distribution of z-position and $x - y$-position respectively of the vertex.

During reconstruction the trigger conditions of the event are set, which can later be used for rejection of certain events. It is stored in a trigger bit that includes information about run conditions. Pile-up[2] was also rejected through this trigger bit

[1]See the on-line run Run Condition Table, `http://alimonitor.cern.ch/configuration/`

[2]Pile-up events are events where several distinct collisions occur, e.g. more than one pp collision in one bunch-crossing.

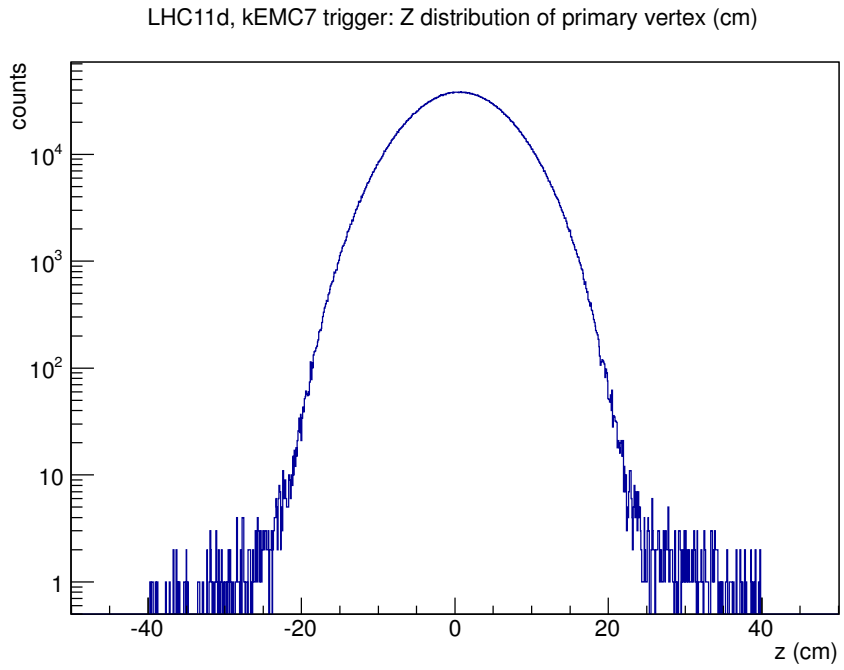

Figure 4.1: The z-position distribution of the reconstructed vertex for LHC11d 7 TeV 2011 proton-proton collisions before event selection cuts.

Table 4.2: Event criteria set on Global Quality = 1 events.

Parameter	unit
Vertex z-cut	$\|V_z\| < 10$ cm
Pileup	reject
Trigger bits	kEMC7 (1024) kINT7 (2)
No bunch crossing	reject

since pile-up events are identified at reconstruction and this information is also stored in the trigger bit. Additionally a check including information from the TOF detector was done to ensure that relevant electron tracks were taken from the defined primary vertex [3]. Information about events with no bunch crossing is also stored in the trigger bit, which makes beam-gas events available to be included or excluded in the analysis. Selecting events through the kEMC7 yields about 5 M remaining events, for a total integrated luminosity L_{int} of about 210 nb^{-1}.

[3]TOF has high-precision time measurements for tracks, which can be used to reject those tracks that come from other distant vertices in the event not associated with the primary collisions. The AliRoot function track->GetTOFBunchCrossing(fESD->GetMagneticField()) is used to reject such tracks.

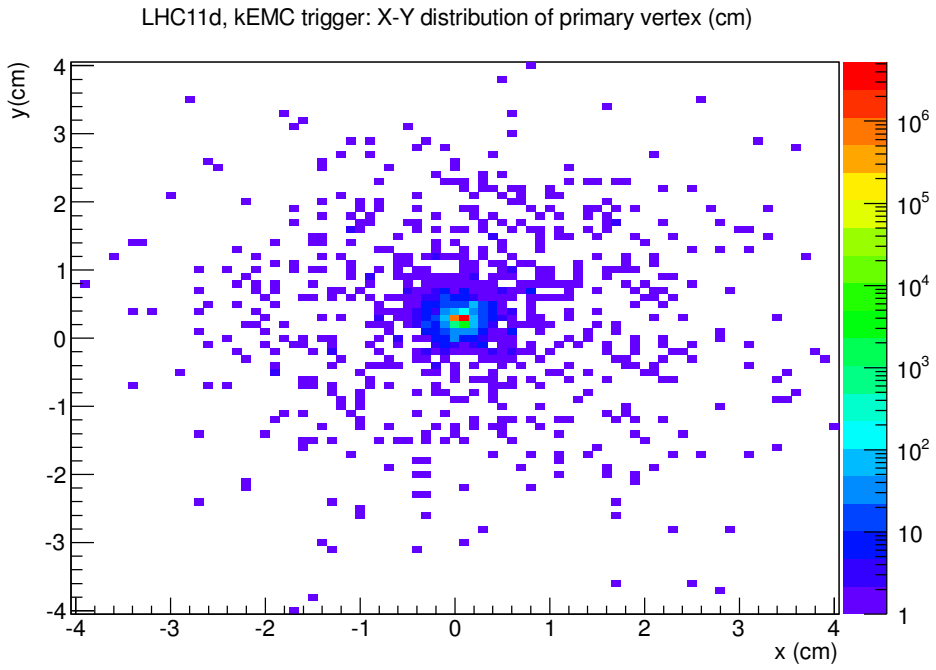

Figure 4.2: The $x-y$-position distribution of the reconstructed vertex for LHC11d 7 TeV 2011 proton-proton collisions before event selection cuts.

4.1.2 Simulation data

Monte-Carlo (MC) simulations within ALICE are an integral part of AliROOT [106], [107]. Without simulations, analysis would be impossible. Particle interactions with different detectors are well understood and simulations describe them well. When using MC to correct real measurements it is important to limit corrections to steps that are well understood. For example, the mechanisms involved in bottom and charm electron production are quite well understood, however the relative abundances or the suggested quenching of the parent bottom or charm hadrons are not well known. In order to correct data for losses in detectors etc. one cannot use purities, i.e. $e^{\pm}_{b-pur} = e^{\pm}_{b-detected}/(e^{\pm}_{b-all} + e^{\pm}_{c-all})$ but instead one has to limit oneself to efficiencies which are independent of any particle species ratio, i.e. $e^{\pm}_{b-eff} = e^{\pm}_{b-detected}/e^{\pm}_{b-all}$ and $e^{\pm}_{c-eff} = e^{\pm}_{c-detected}/e^{\pm}_{c-all}$, and a measured observable such as D mesons to remove charm contribution, yielding a b-electron measurement. Thus, MC was used for two steps in this analysis; estimation of tracking efficiency (detector and p_T unfolding efficiency) and removal of background in the b-electron sample.

Simulations within AliROOT consist of two steps: simulation and reconstruction. The simulation step starts with geometry and event definition, then it proceeds with

particle generation. The generated particles are then propagated through the material using libraries from GEANT3, GEANT4 or FLUKA [108], [109], [110] to simulate particle-material interactions. Then "hits" in the detector are generated. These contain the energy deposited in the detector by the particle, their position, impact time and which particle caused the hit. Finally digitalization of the hits is done, converting signals in the detector to simulated electronic readout which is observed in a real event. These steps are unique to the different detectors within ALICE, thus they have been tuned and tested by the individual ALICE sub-detector groups. For the EMCal [111] all hits within one tower are summed, then this is converted into ADC amplitude units along with added electronic noise. This is equivalent to the ADC response that is measured in the real EMCal.

The reconstruction step is equivalent to the reconstruction step involved in real data; it converts signals from detectors into detected particles. For the EMCal this involves collecting digits (or ADC signal) into clusters (clusterization as described above), converting these to a cluster energy, then finally calculating relevant parameters for particle identification such as cluster center to be used in track-cluster matching. Finally the output of this step is written into Event Summary Data (ESD), or Analysis Output Data (AOD) files to be used for analysis.

In both these steps the ALICE OCDB (Off-line Conditions Data Base) is accessed to ensure realistic simulation conditions. This will anchor the simulation to a specific run by passing the run number as a parameter in the simulation. Among many things the OCDB corrects for calibration voltages of the sub-detectors for the relevant run, off-line segments in a detector and detectors that were off-line for the particular run.

Since there were no simulations anchored to the LHC11d period available the simulation and reconstruction macros had to be generated, tested and evaluated prior to full simulation. This was done at the Yale Bulldogk cluster and the NERSC Carver cluster at LBL in spring 2012. Official AliROOT production v5-02-Rev-13 was used for the simulation. Before the production could be submitted to the GRID, all detectors had to give permission to go ahead. Since the TPC gain had been changed from the previous period where a simulation was available (LHC11a), these had to be re-tuned by TPC experts. The gain could never be fully changed to agree with data (to much dismay) so there is a known discrepancy in the TPC simulation part, as discussed below (Fig 4.6) which will add to the systematic error of the tracking efficiency. Finally in October 2012 the simulation production was submitted and took an equivalent of 24.5 CPU years to finish.

The simulation was named LHC12d2 and is a heavy-flavor electron enhanced

sample anchored to LHC11d data;

- Generator: Pythia6 Perugia-0 tune 320, proton-proton
- Collision energy: 7 TeV
- Detector simulator software: GEANT3
- Heavy-flavor electron (HFE) enhanced sample statistics: 6 M 50% b-hadron and 50% c-hadron events with forced decay to electrons
- AliRoot v5-02-Rev-13
- Anchored to runs: 156889, 156891, 157275, 157277, 157564, 157734, 158086, 158285, 158285, 158304, 158492, 158516, 158520, 159538, 159580 and 159582 with a flat distribution.

4.2 Tracking

This section describes tracking, data quality with regard to the ITS and TPC detectors, track cuts, tracking efficiency and the MC studies needed to correct for tracking inefficiency and unfolding in p_T.

Good tracking and track resolution is paramount both in identifying electrons and for calculating the different parameters involved in a b-tagging algorithm. Secondary vertexing mainly consists of calculation of distances between electron tracks and the primary vertex, thus the spatial resolution close to the primary vertex is critical.

As covered in Chapter 2, tracking in ALICE rests on the ITS and the TPC detectors, which were designed to operate in a charged track density $dN/d\eta$ of about 8000 with a tracking efficiency greater than 90% for tracks from 0.1 GeV/c and up.

Tracking in ALICE makes use of a Kalman filter approach for track recognition and reconstruction using the ITS and the TPC detectors [112], [113]. It is initiated with a vertex-finding algorithm that operates on the information delivered by the two innermost ITS (SPD) layers. When the primary vertex is identified, the full tracking, Global Tracking, commences. It starts with the best tracking detector, i.e. the TPC, at the outermost radius for minimal track density. Track candidates, or "seeds" are found and the tracking continues towards smaller radii. A Kalman filter is used to associate new clusters to the track candidates, and an iterative approach yields increasingly refined track parameters. After all seeds are extrapolated to the inner TPC radius the ITS information is included. The ITS attempts to extrapolate

the TPC tracks to the primary vertex and along the way ITS hits are assigned to the extrapolated track. After the TPC track candidates have had ITS hits assigned, the ITS runs an independent tracking algorithm on the ITS hits that were not associated with the TPC candidate tracks, in order to try to recover tracks that where not found in the TPC for various reasons (dead zones in the TPC, p_T cut off or decays). Next the tracking is restarted, this time from the primary vertex outwards to the outer radius of the TPC. At this point the track resolution is sufficient for extrapolation into the other detectors, such as the TRD, TOF, HMPID, PHOS and the EMCal. Now particle identification can be performed and this information is included in the track information and the tracks are again refitted with the Kalman filter backwards to the primary vertex for the final track parameters.

4.2.1 ITS TPC data QA

With regard to tracking and track resolution at the vertex, the SPD is an essential component for high-resolution tracking, thus bottom-electron analysis. Regarding the selection of data to analyze, the two layers of the SPD had several dead regions due to a cooling problem with the SPD for the 2009-2011 runs. Two hits in the SPD are required for good quality tracks. These dead zones in the SPD combined with the then more limited coverage of the four installed EMCal SMs (Super Modules) rejected many tracks in the EMCal η-ϕ coverage, see Figure 4.3. The combination of no EMCal trigger, limited coverage of the EMCal in 2010 and low yield of high quality tracks resulted in poor statistics available for bottom electron analysis with the EMCal in the 2010 data set. During the winter of 2010-2011 the EMCal was upgraded, see section 3.2, and the EMCal trigger became operational. This provided more statistics, an enhancement of high-p_T tracks and more quality tracks within the EMCal, see Figures 4.4 and 4.5. This was the main reason for selecting the LHC11d data sample as the basis for this thesis. In the Figure 4.4 the 2-D hit-map of tracks with hits in both layers is shown to indicate where tracks with good quality can potentially be found. Note that there is considerable deficiency within the EMCal acceptance. To cope with this it was decided to require only one hit in the SPD, but 4 combined hits for the total six layers of the ITS. The resulting tracks can be seen in Figure 4.5; it gives a reasonable track yield with good track resolution.

The next set of track quality parameters comes from the TPC. The main TPC track-quality parameter is the number of TPC clusters in a reconstructed track,

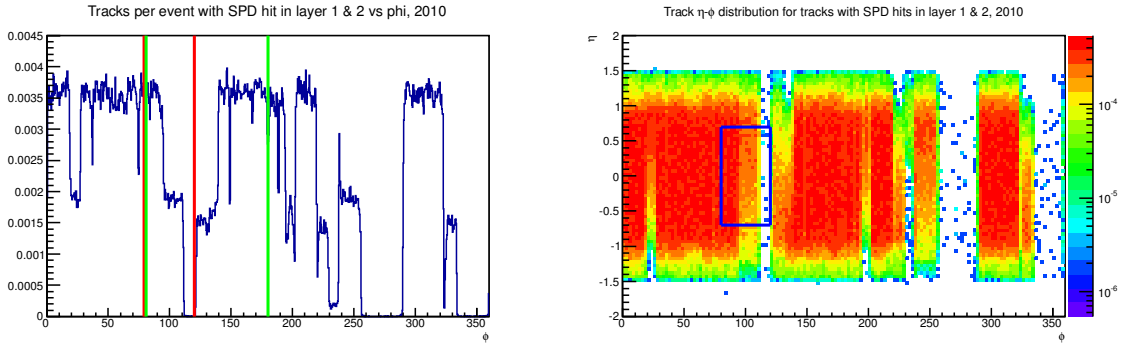

Figure 4.3: ITS SPD: tracks with hits in both layers. Left: tracks per event with $p_T > 1.0$ GeV/c. Red lines indicate EMCal 2010 ϕ-coverage, green lines indicate 2011 ϕ-coverage. Right: ITS ϕ-η hit-map for tracks with $p_T > 1.0$ GeV/c. The blue box indicates 2010 EMCal ϕ-η coverage.

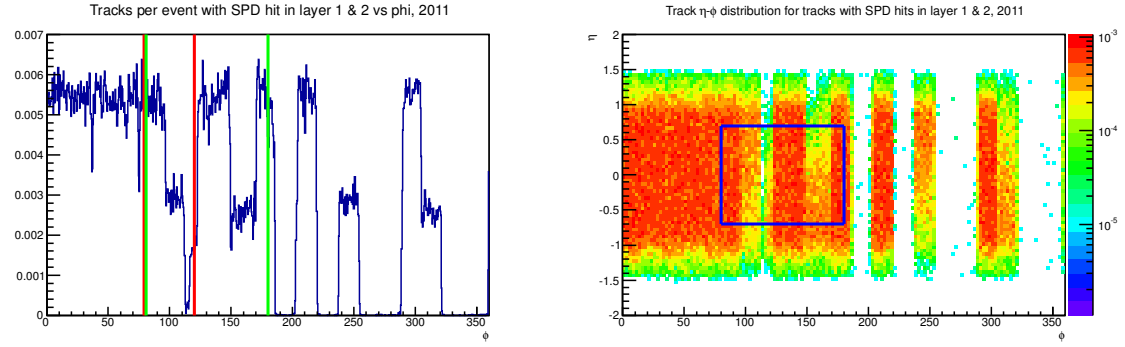

Figure 4.4: ITS SPD: tracks with hits in both layers. Left: tracks per event with $p_T > 1.0$ GeV/c. Red lines indicate EMCal 2010 ϕ-coverage, green lines indicate 2011 ϕ-coverage. Right: ITS ϕ-η hit-map for tracks with $p_T > 1.0$ GeV/c. The blue box indicates 2011 EMCal ϕ-η coverage.

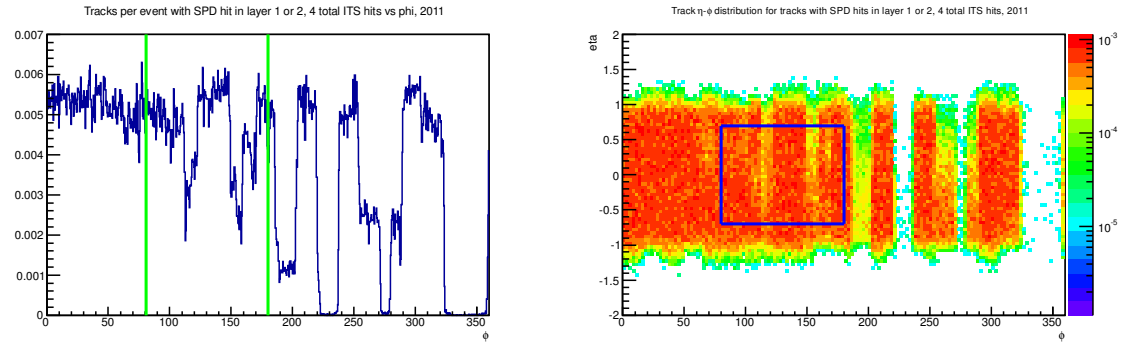

Figure 4.5: ITS SPD: tracks with hits in either SPD layer, with a total of 4 ITS hits. Left: tracks per event with $p_T > 1.0$. Green lines indicate EMCal 2011 ϕ-coverage. Right: ITS ϕ-η hit-map for tracks with $p_T > 1.0$. The blue box indicates 2011 EMCal ϕ-η coverage.

$N^{TPC}_{Clusters}$, out of the number of *findable clusters*[4] which count 159 in the $\hat{r}$-direction. Genuine tracks from the primary vertex have on average large $N^{TPC}_{Clusters}$, see Figure 4.6, thus in order to reject bad tracks made up from residue TPC clusters and other noise, a cut of $N^{TPC}_{Clusters} > 100$ was implemented. Standard track cuts employed by the ALICE collaboration place the cut at roughly half the number of findable clusters, i.e. $N^{TPC}_{Clusters} > 80$. However, high transverse momentum electrons from heavy flavor decay were analyzed, requiring a stricter cut of $N^{TPC}_{Clusters} > 120$ which was commonly used within most ALICE heavy-flavor analyses. For the 2011 run the gain of the TPC was lowered due to increased luminosity of the LHC beam [5]. This resulted on average in less found TPC clusters per track than for previous periods. As described in the MC section, this poses a problem; when the tracking efficiency is calculated one employs the real data cuts on simulated data, then the tracking efficiency is obtained from simulation and applied to real data. The assumption is then that the simulation, to a reasonable extent, describes real data. This means that the distribution of any cut parameter should be the same in data and simulation, or else wrong tracking efficiency is obtained from simulation and unjustly applied to data. The MC simulation that was supposed to describe real data did not describe the $N^{TPC}_{Clusters}$ parameter well; it did not account for the lower TPC gain in 2011, see Figure 4.6. Several attempts to correct this were tried, over the course of 8 months, but ultimately abandoned. Instead a general recommendation was issued by the ALICE simulation coordination to lower the $N^{TPC}_{Clusters}$ cut to about 100, so that the cut is done sufficiently below the point where the two distributions deviate from each other. The ultimate test, if this is an acceptable solution (which it is) is to look at the systematic error associated to tracking cuts which is discussed in Chapter 6. There is also a ratio-cut of found clusters over findable clusters $r^{TPC}_{findable}$ that is enforced, which is usable if the track is short. Thus placing a $N^{TPC}_{Clusters} > 100$ cut is too restrictive. The $r^{TPC}_{findable}$ was set to greater than 0.6. The tracking algorithm in the TPC involves fitting a track to a number of space points. The χ^2 associated with this fit is required to be less than 4. The last TPC parameter to check is the energy loss parameter of tracks, which is calculated from the amount of charge deposited in the TPC clusters, see [89]. On average the distribution of dE/dx versus p_T should be uniform throughout the different runs, however certain runs have significant deviations from this normal behavior. This indicates that something was wrong with the TPC for that run, and such runs

[4]Findable clusters means maximum number of possible clusters for a given track.

[5]The higher luminosity caused the TPC to *trip*; shutting it down in precautionary protection mode. Lowering the TPC gain makes the TPC less sensitive, thus preventing it to trip.

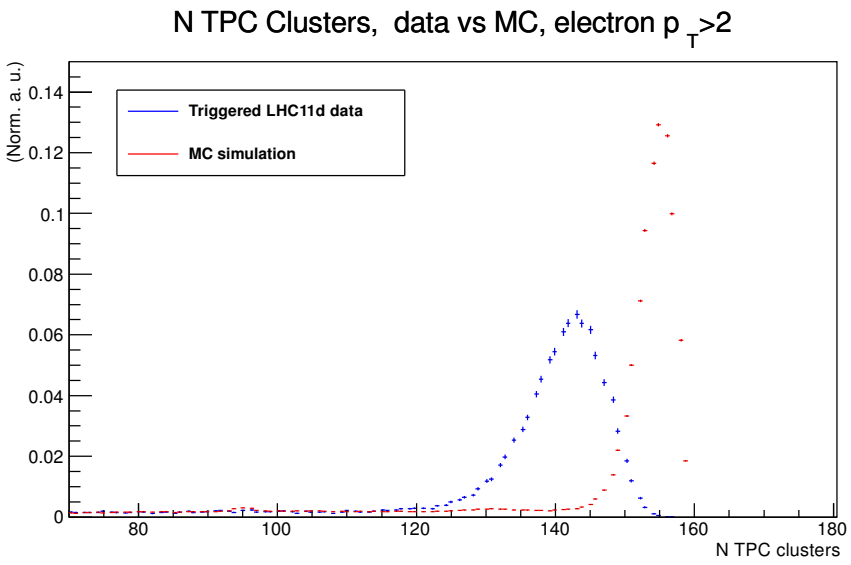

Figure 4.6: TPC number of clusters for all electron tracks with p_T greater than 2 GeV/c. The real data are shown in blue and simulations in red. The simulations do not describe data well for this parameter.

should be excluded. In Figure 4.7 a comparison between a general good run and a bad run is shown; such bad runs were excluded on the basis of bad dE/dx assigned to tracks.

Finally some general cuts are placed on tracks that are common in most analyses; no tracks with kinks and tracks must point back to the primary vertex. The primary vertex cut is placed at 3.0 mm in both x-y, and z-direction.

4.2.2 Tracking Efficiency

Now is the right occasion to properly define tracking efficiency. It is the ability of successfully reconstructing a track made by a charged particle in the ITS-TPC detectors as a function of transverse momentum, with the previously described track quality cuts imposed after the track reconstruction, in short:

$$\varepsilon_{Tracking} = \frac{Tracks_{\text{Reconstructed}} \wedge |\eta| < \text{geometric acceptance} \wedge \text{relevant track cuts}}{Tracks_{\text{All}} \wedge |\eta| < \text{geometric acceptance}}. \tag{4.1}$$

This requires the knowledge of "all tracks" and their respective momentum. This is however quite a challenge to actually measure in an assembled detector. Instead one has to rely on MC simulations. Simulations do an adequate job in describing

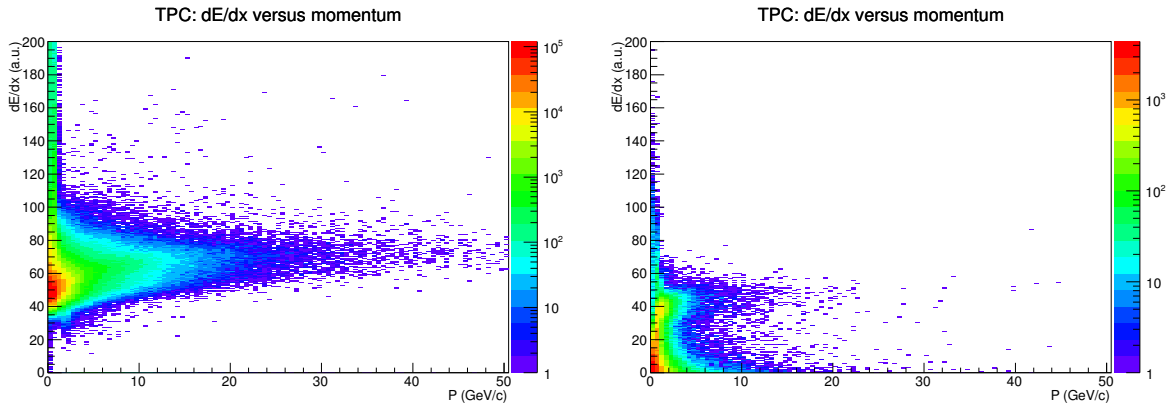

Figure 4.7: Left: TPC dE/dx parameter as a function of track momentum for the "good" run 159582. Right: The respective TPC dE/dx for a "bad" run, in this case run 157560. Note the lower average dE/dx for the tracks. This is probably due to several regions in the TPC having low/no gain for this particular run.

the full detector. In the simulation particles collide and new particles are created that interact with the simulated detector. The tracks are then reconstructed and one counts how many particles were recovered. The particle species matter (and so does charge), so for electron tracking efficiency a mix of $e^{\pm}$ is needed. Furthermore, bottom electrons are assumed to behave as any other electron, i.e. the tracking efficiency is similar for electrons originating from different sources. The tracking efficiency as a function of transverse momentum can then be written as:

$$\varepsilon_{Tracking} = \frac{\text{Track}_{Reco.} p_T(|PDG| = 11 \wedge |V_{Z,MC}| < 10 \wedge |MC_R| < 7 \wedge |\eta_{MC}| < 0.6)}{\text{Particle}_{MC} p_T(|PDG| = 11 \wedge |V_{Z,MC}| < 10 \wedge |MC_R| < 7 \wedge |\eta_{MC}| < 0.6)},$$

which means the MC-p_T of reconstructed tracks over the MC-p_T of actual simulated particles, with the demands that they are electrons, that the vertex in z-direction is within 10 cm (like data), that the electron is produced within 7 cm from the MC vertex (like the ITS de-facto physical limit in data) and finally that the particles have a MC η of ± 0.6. PDG is the particle data group particle code [48] (11 for electrons and -11 for positrons). Now the transverse momentum part has to be properly dealt with, which has been intentionally kept ambiguous until now. The measured p_T is different from the original p_T of the particle. Reconstructing particles with *exactly* p_T = 10 GeV/c will yield a somewhat Gaussian distribution in reconstructed p_T space. This is commonly referred to as "unfolding" or "p_T-smearing". There are two ways to deal with this, first the smearing effect may be included into the definition of the

Table 4.3: Summary of all track cuts used in the electron level analysis.

Track Selection (electrons)	
ITS SPD hits	one hit in either layer
ITS total hits	≥ 4 total hits in any layers
Require ITS refit	true
Number of TPC clusters	≥ 80 hits
Accept kink daughters	false
Require TPC refit	true
Track to primary vertex xy-DCA	≤ 3.0 mm
Track to primary vertex z-DCA	≤ 3.0 mm
Ratio of found to findable TPC clusters	≥ 0.6
TPC χ^2/cluster	≤ 4

tracking efficiency;

$$\varepsilon_{Tracking} = \frac{\text{Reconstructed MC electron-track p}_T}{\text{All MC electron-track p}_T}. \tag{4.2}$$

This definition then includes the effect of p_T smearing since the numerator is in measured p_T space, or reconstructed p_T space, and the denominator is measured in the actual real p_T space (called MC p_T since this is within MC simulations). If the difference between measured p_T versus real p_T is small, then this approximation is valid. If the difference is not small, then one has to first "un-smear" or "unfold" the measured spectra into real (MC) p_T space, and then apply the pure MC p_T efficiency defined as

$$\varepsilon_{Tracking} = \frac{\text{Reconstructed electron-track real (MC) p}_T}{\text{All MC electron-track p}_T}. \tag{4.3}$$

This is the definition used by most collaborations. Then in order to apply the tracking efficiency of a measured spectrum, the spectrum first has to be unfolded. The unfolding step is explained below. The tracking-efficiency for electrons (and pions) obtained from simulations can be seen in Figure 4.8. Applying this to unfolded real data results in the correct tracking-efficiency-corrected spectrum, assuming that the MC simulation is reliable. This hypothesis is tested in Chapter 6. For reference the tracking efficiency with the p_T-smearing effect included can be seen in Figure 4.9. A check was made to confirm that the tracking efficiency of electrons in general versus b-electrons is similar. Finally a summary of track cuts can be seen in Table 4.3.

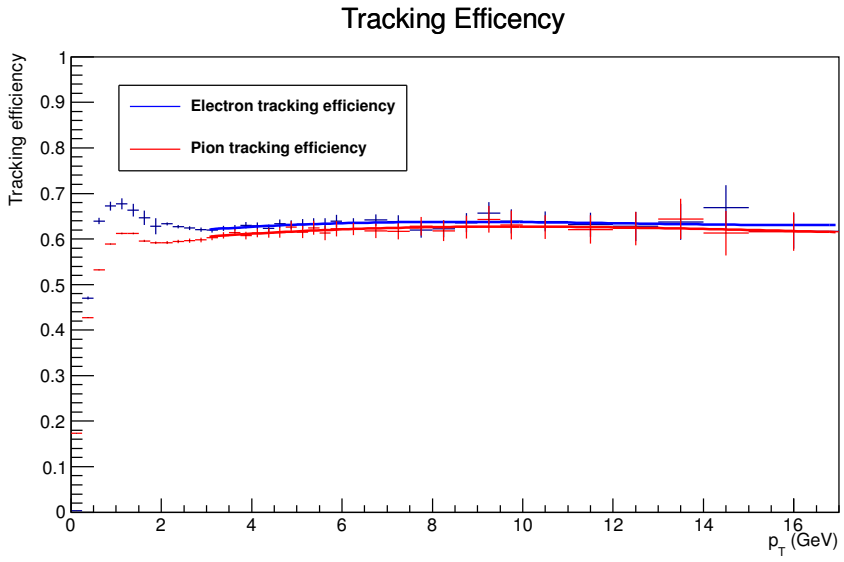

Figure 4.8: Tracking efficiencies for electrons and pions with the track cuts listed in Table 4.3. This is in real p_T space, i.e. unfolded p_T.

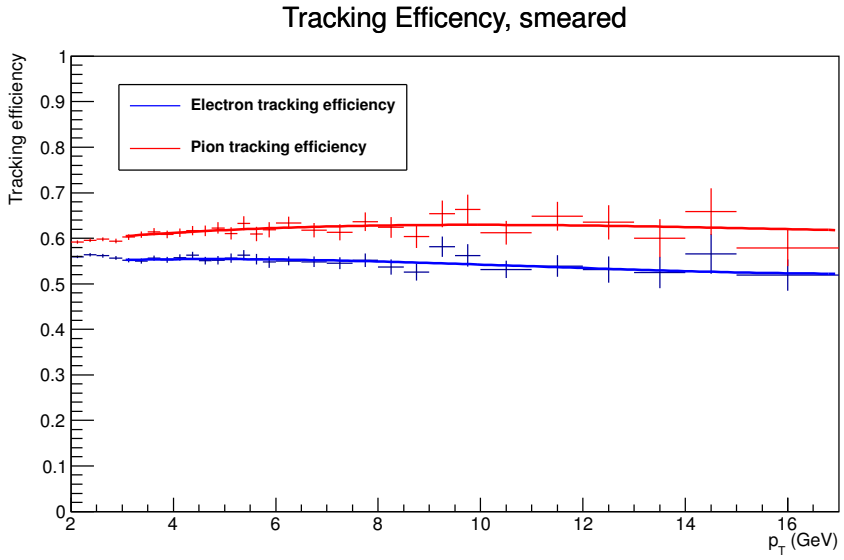

Figure 4.9: Tracking efficiencies for electrons and pions using the track cuts listed in Table 4.3 using reconstructed p_T over real p_T, i.e. smeared tracking efficiency.

4.2.3 p_T Unfolding

The p_T-unfolding or p_T-smearing correction is necessary since the measured p_T and actual p_T of a particle are different. This is mainly due to detector resolution and efficiency, particle energy loss, systematic biases etc. In general the measured transverse momentum is less than the real transverse momentum of a particle. p_T unfolding is important in p_T regions with high variation in measured versus real p_T, which is in general larger for lower transverse momentum. Simulations are used to study this p_T smearing and a 2-D plot of MC p_T versus measured MC p_T can be seen in Figure 4.10. In general for a histogram where the true and measured bins are labeled T_j and M_i one can construct a matrix R_{ij} that maps the true bins onto the measured ones. R_{ij} is called the response matrix and can be generated from available MC simulations, in this case by using simulated electrons within the ALICE detector. Then the unfolding algorithm will reconstruct the true T_j from the measured M_i, taking into account statistical fluctuations due to a finite sample. There are several packages capable of constructing such a matrix, and using it to unfold a physical measured spectrum through an unfolding algorithm. For the analysis in this thesis the package "ROOUNFOLD" [114], [115] was used, which is written in C++ and compatible with ROOT and AliROOT. It can make use of several different algorithms, such as iterative "Bayesian", singular value decomposition (SVD), bin-by-bin (simple correction factors) and simple inversion of the response matrix without regularization. Different algorithms were tested both to validate the algorithms and to estimate the systematic error involved in the unfolding step. This is explained in Chapter 6. The main unfolding algorithm used was the Bayesian algorithm. It is an iterative algorithm and the number of iterations can be passed as a parameter in the unfolding correction. This parameter was also changed and studied in order to estimate the systematic error involved. In Figure 4.10, where the true versus measured p_T can be seen for electrons and pions, the electrons show a larger deviation from a linear response due to Bremsstrahlung losses. This along with the finite p_T resolution are incorporated into the response matrix. In Figure 4.11 a closure test of the unfolding algorithm on the MC simulation data is shown. Here the measured p_T is unfolded back to real p_T which is compared to the true MC p_T. The unfolding works as expected. Note that the unfolding has to be performed prior to correcting with the tracking efficiency since the tracking efficiency is defined only in true p_T space.

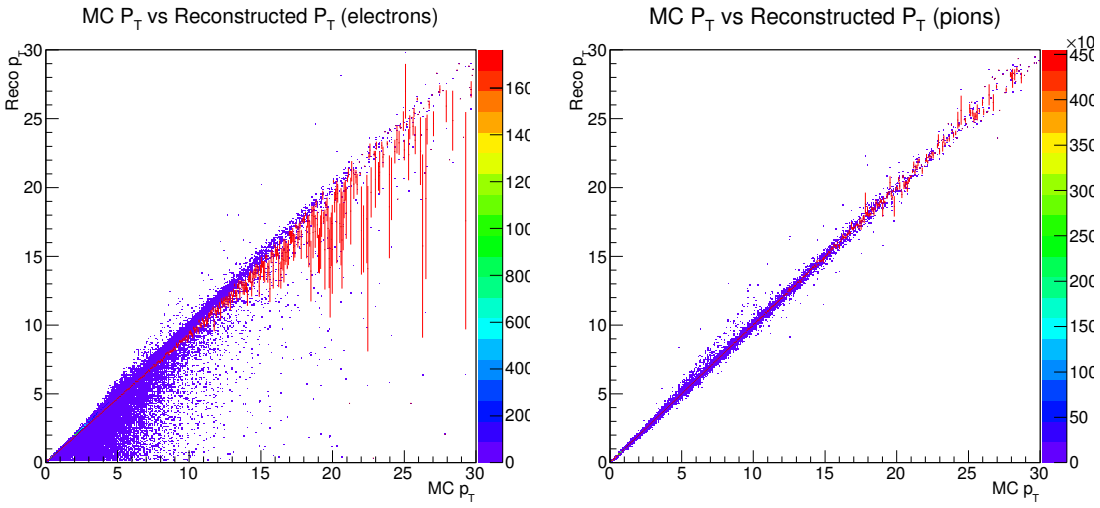

Figure 4.10: Left: reconstructed versus MC p_T (GeV/c) for electrons. The deviation from linear behavior is due to bremsstrahlung effects. Right: reconstructed versus MC p_T (GeV/c) for pions.

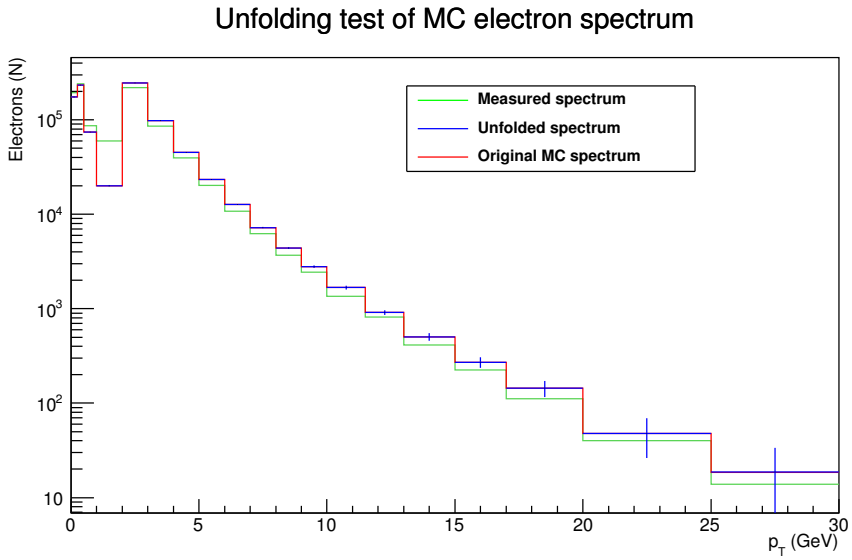

Figure 4.11: Toy model test of unfolding algorithm using simulated electron spectrum. The green histogram are the measured data points. This spectrum is then unfolded to yield the blue data points, the unfolded spectrum. This should coincide with the original red MC spectrum. The unfolding matrix is constructed from these data, thus per definition the unfolded spectrum must coincide with the original spectrum. The agreement is exact.

4.3 Particle identification

This section describes how electron particle identification (PID) was carried out, the cuts used, and the measured efficiency and purity of the electron sample. The previous chapter discussed electromagnetic calorimeters, how they interact with particles and how one can distinguish different particles. Here these concepts will be used on real data and the efficiency of this electron identification is discussed. Note that this section describes the efficiency of finding an electron from those that are available. It does not specifically describe electrons from a certain source, but rather all electrons in general. It is assumed that the efficiency for explicitly finding an electron from bottom decay is the same as finding electrons from any source. This assumption is valid unless there is some fundamental difference between electrons from bottom decay and electrons in general. In the "eyes" of the ALICE detector, and specifically the EMCal, electrons from bottom decay are as likely to be identified as any other electron. This electron identification efficiency is then applied on electrons from bottom, which will then correct for identification inefficiencies. The purity of the electron sample will also be discussed. The purity discussed here is the inclusive electron sample purity. This cannot be applied to the bottom electron sample since this purity changes when the b-tagging algorithm is executed on the electron sample (i.e. the probability of tagging electrons in general is different from the probability of tagging pions). The b-electron versus hadron purity is discussed in section 5.3.2. For a summary of PID cuts, see Table 4.4.

4.3.1 Track matching and E/p

Most of the charged tracks in an event originate from light hadrons, such as pions. Electron identification is used to reject hadrons while keeping the relevant electrons. In ALICE there are several detectors designed for electron PID, most notably the TPC, TRD and the EMCal. At the time of writing, the TRD, which was supposed to be the main electron PID detector at high p_T, is still not fully working and not fully installed. Thus, the combination of the TPC and the EMCal provides *the* method to identify electrons at high p_T. In section 3.3 different methods of identifying electrons were discussed, mainly shower shapes in an electromagnetic calorimeter. In the end, the improvement of using shower shape cuts is not very significant compared with the loss of statistical sample. Instead, the TPC/EMCal's main electron identification parameter is EMCal cluster energy over TPC track momentum, E/p. To calculate this parameter the track reconstructed in the ITS/TPC is extrapolated to the EMCal,

from the end of the TPC at a radius of 247 cm to the EMCal at a radius of 450 cm. Extrapolation is done with the assumption of the ALICE magnetic field of 0.5 T and using the track parameters at the end of the TPC. The track impact position in the EMCal is then compared to nearby EMCal clusters. The clusters are formed through a clustering algorithm, such as those described in Section 3.3. The distance from the cluster center to the track is called residual and is defined in $\eta - \phi$ space as $\Delta R = \sqrt{(\phi_{track} - \phi_{cluster})^2 + (\eta_{track} - \eta_{cluster})^2}$. A small residual indicates a direct match of track and resulting cluster. Due to the magnetic field the residual has an elliptic shape in $\eta - \phi$, with the major axis in the ϕ direction. Therefore an asymmetric residual cut is used, 0.05 in $d\phi$ and 0.025 in $d\eta$. A plot of the residual parameter is shown in Figure 4.12. If a track fails the residual cut it will not be matched to any cluster, which can happen if several tracks contribute to a single cluster, thus displacing the center of gravity of the cluster. It will then be assigned an $E/p = 0$. If a track did not generate a cluster or the cells in the vicinity of the track impact were bad, a cluster will not form and the track will be assigned $E/p = 0$. A cluster can have several tracks matched to it, but not the other way around. It is important to keep all tracks and not reject them since all the efficiencies must be accounted for, and if the track reconstruction step was successful, the rest of the rejected tracks such as no track-cluster match will go into the PID efficiency. The E/p parameter for electrons and hadrons within a p_T slice, along with simulation, can be seen in Figure 4.13.

4.3.2 EMCal QA

For the 2011 data taking, the EMCal consisted of 10 super modules. The trigger functionality of the EMCal had also been activated this year. One problem that occurred was that the LED system was active and somehow got mixed up with real events, yielding unreasonable activity in the EMCal. The LED system is a set of LEDs providing light directly into the scintillator for the EMCal to detect. Since the light provided should be constant in time, variations such as temperature can be corrected for with the use of the LED system. The intermix of LED events and real events can easily be separated since an LED event will have most towers active with order of GeV energy. This only occurred for the first period LHC11a. For the subsequent run periods this problem was resolved. The LED system was designed to be a calibration tool, but was never used for this. Temperature variations are corrected for by the LED system for the test-beam data and runs after 2012 (not in

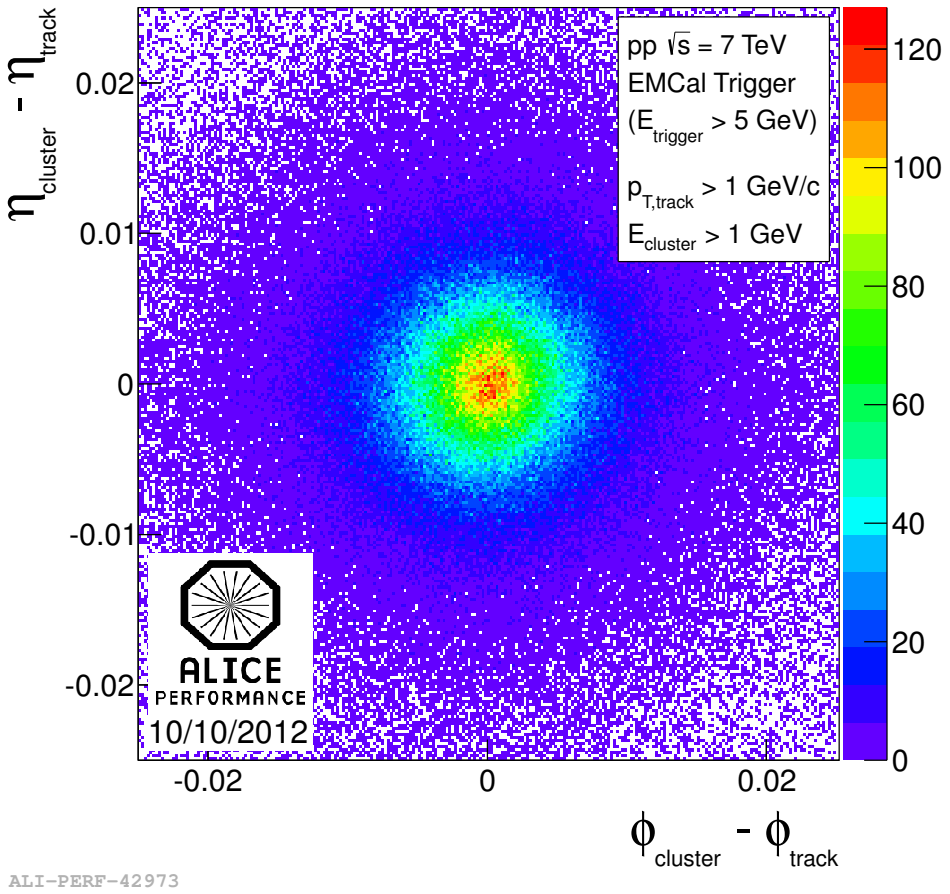

Figure 4.12: Distribution of the residuals for the EMCal clusters to track matching in pseudo-rapidity ($\eta_{cluster} - \eta_{track}$) vs. azimuth ($\eta_{cluster} - \eta_{track}$) in proton-proton collisions at $\sqrt{s} = 7$ TeV triggered by the EMCal. Only clusters with an energy $E_{cluster} > 1$ GeV and tracks with a transverse momentum $p_{T,track} > 1$ GeV/c are used.

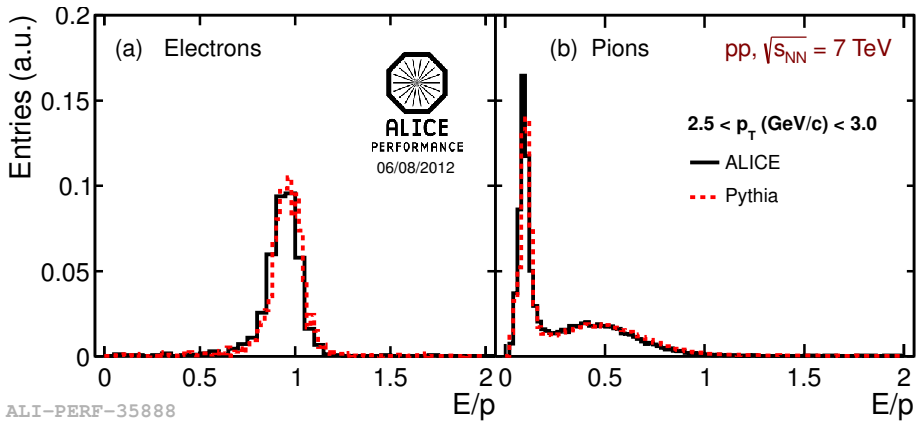

Figure 4.13: E/p for (a) electrons and (b) hadrons in simulation and 7 TeV proton-proton data, matched track p_T of 2.5-3.0 GeV/c. Rough particle selection is done with TPC nσ.

2010-2011 due to lack of code, available effort and higher priorities). The temperature variation for the EMCal in the ALICE detector is rather stable thus the effect from temperature variation was small.

For most runs during LHC11d about 100 towers were disabled, either through hardware or software disabling. Hot and defective towers must be removed, else clusterization will fail and likewise analyses. In Figure 4.14 is a $\eta - \phi$ plot of hits in the EMCal during the LHC11d period. Removed towers can be clearly seen. Larger dead areas can be due to faulty electronics etc. In Figure 4.15 the hit rate for run 158285 is shown. It should be uniform and any deviation from this rate is the result of bad cells. In this Figure the bad towers have been set to zero. If they were not masked out the hit rate would have been many orders of magnitude larger.

The EMCal tender (version r55343) which is a software class for applying corrections while analyzing data were used in the analysis. These corrections include non-linearity correction, energy recalibration, misalignment correction, reclusterization. Clusters are selected by applying the following criteria:

- 50 MeV of minimum energy is required for a tower to contribute to a cluster.
- Minimum cluster energy is 150 MeV.
- 100 towers are masked either through on-line masking or masking when off-line reconstruction is performed. Bad or hot towers are defined to be towers that have a 5σ firing rate away from the average firing rate.

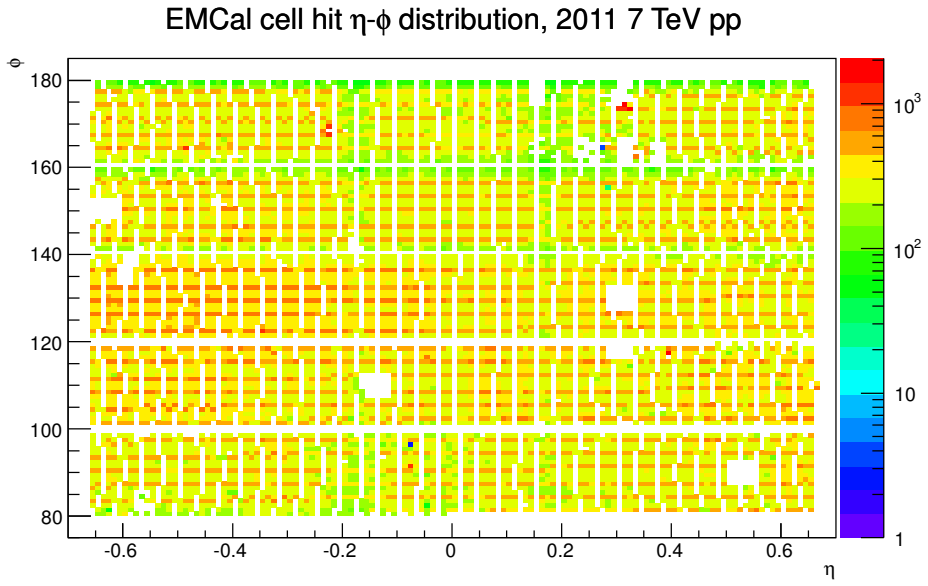

Figure 4.14: Hits in the EMCal during run 158285. Masked out towers can clearly be seen.

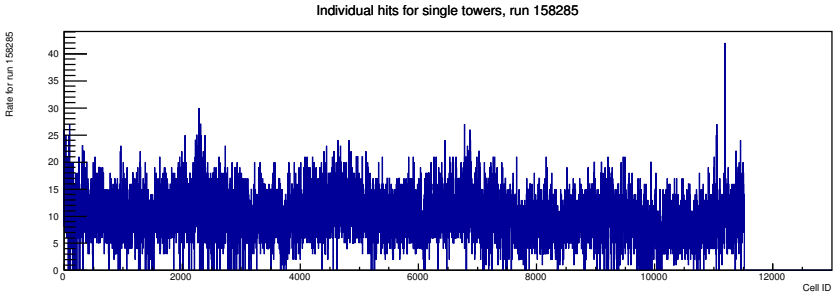

Figure 4.15: The hit rate in the EMCal for run 158285. Masked out towers are put to zero, or they would have orders of magnitude larger hit-rate.

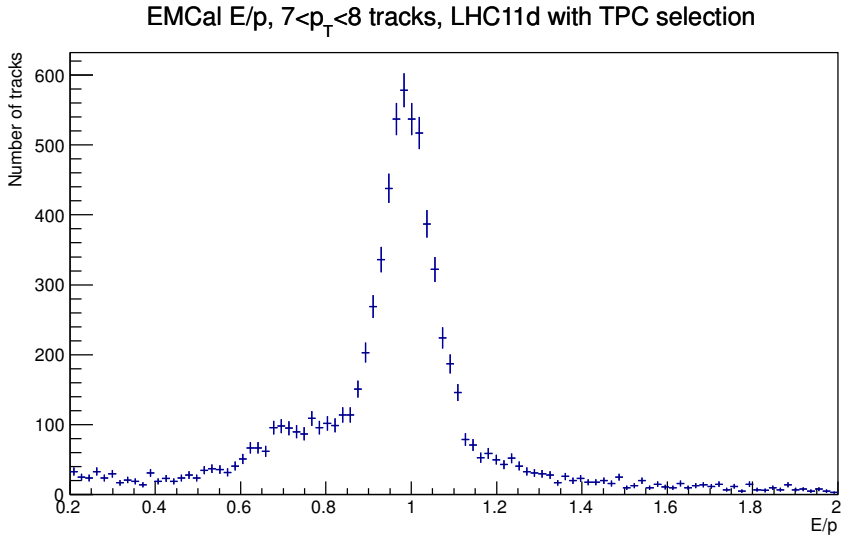

Figure 4.16: E/p for electron candidates in 7 TeV proton-proton data, $7 < p_T < 8$ GeV/c tracks. Basic track selection is done with TPC nσ.

Finally the E/p parameter can be seen in Figure 4.16. This was plotted for electrons with a transverse momentum of 7-8 GeV/c. It has been formed with the V2 clusterizer and corrected with non-linearity. The electron bump can clearly be seen near unity, which indicates a well performing calibration of the EMCal and good clusterization algorithms. The background is due to hadrons and can be corrected for by specifically selecting and looking at only background, i.e. pions. This is described in more detail in Section 4.3.4 and Section 5.3.2. The E/p plot has been cleaned up with the help of TPC nσ selection.

4.3.3 Efficiency & Purity TPC-EMCal

The PID efficiency and purity are two principal measurements that can be obtained from data. An attempt to obtain these values from simulations was done, however triggered data are different from minimum-bias data in the sense that high-p_T electrons and pions are enhanced in a biased way by introducing a cluster trigger. Since triggered data are not well simulated this step failed, data-driven methods had to be used. For the electron PID efficiency there was only one viable option, the energy-loss of the tracks (TPC dE/dx) must be used to define "all electrons", and then this compared to the selected tracks after all PID cuts. This was done by plotting the dE/dx parameter of all tracks in a histogram with different p_T slices. This will clearly show the separation in dE/dx due to the different particle species. The peaks are

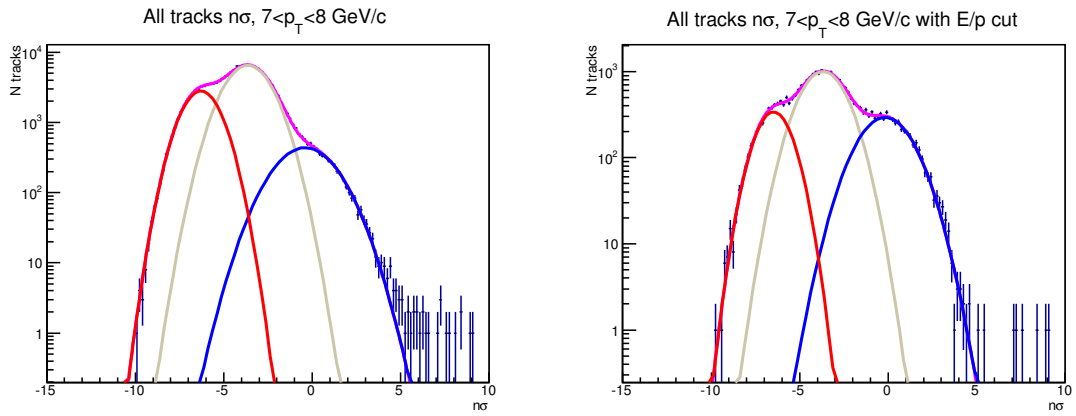

Figure 4.17: Left: nσ distribution for all tracks along with Gaussian fits to the different particle species peaks. Red is for "other hadrons", gray is for pions and blue is for electrons. Right: nσ distribution for all tracks with the EMCal E/p cut applied.

roughly Gaussian, so three Gaussians are used to fit the electron peak, the pion peak and the "other hadrons" peak (mainly kaons). By use of the Bethe-Bloch formula one can form the ideal energy loss lines, see Figure 2.8, and from these ideal lines one can transform any dE/dx signal to its number of sigmas away from the ideal electron line, called nσ. By fitting the three Gaussian peaks in nσ space, the electron Gaussian was defined to be at zero and one can conveniently re-define the otherwise arbitrary-unit parameter dE/dx. See Figure 4.17 for such a plot. "All electrons" was then commonly defined as the integral of the electron Gaussian, or as the number of tracks with n$\sigma > 0$ times two. The latter definition was ultimately used in this analysis.

The same procedure was then used with the nσ plot for all tracks after the E/p parameter had been applied. See Figure 4.17 (right). The E/p range for this analysis was fixed at 0.85 to 1.2. This E/p cut removed tracks where the extrapolation failed, track-cluster matching failed, or if the track was outside the geometric acceptance (the EMCal acceptance, including dead areas of the EMCal due to masking) etc, since $E/p = 0$ was assigned to such tracks. Only tracks with a proper E/p parameter were then counted and filled into the same nσ histogram. The three Gaussian peaks were fitted and identified electrons are those electrons that pass the E/p cut *and* the final nσ cut. The final nσ cut used was -1.5 $< n\sigma <$ 3.0. This includes most electrons and also removes most pions/hadrons. These electron candidates were then compared to "all electrons" and the electron PID efficiency thus defined as

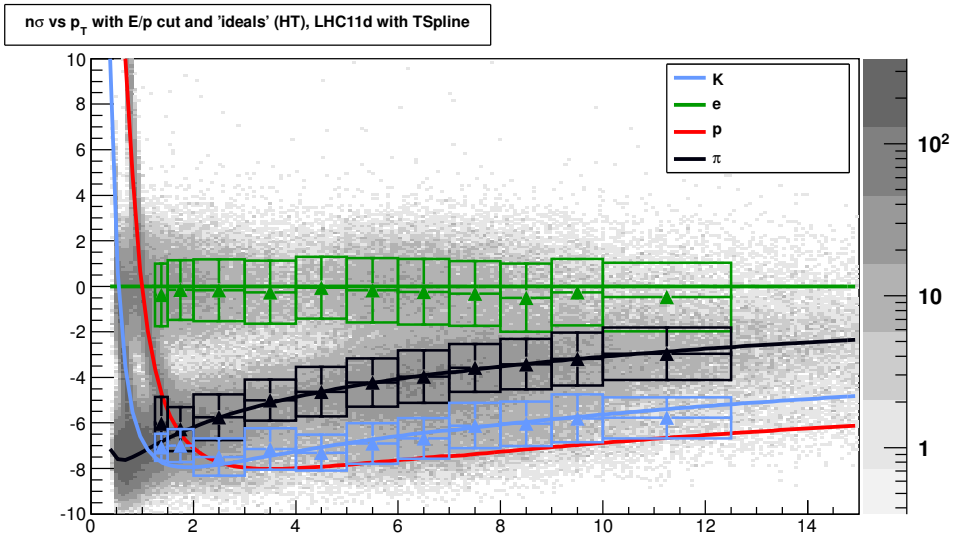

Figure 4.18: The nσ distribution as a function of p. Solid curves are ideal fits of particle species, taken from AliROOT (TSplines function). Data points are fitted Gaussian functions to the various particle species peaks in nσ space.

$$\epsilon_{PID} = \frac{\text{Number of tracks that pass all PID cuts}}{\text{All electrons}}. \tag{4.4}$$

This definition was used on p_T slices from 6-13 GeV/c. As a cross-check the fitted peaks and their widths were plotted on top of the ideal nσ as a function of p. This is shown in Figure 4.18. The fitted peaks are in agreement with the ideal lines. The electron peak is slightly off, but this has been observed in other data-sets and is likely due to non-Gaussian shape of distributions, difficulty in fitting Gaussian peaks and ideal lines that might be slightly off the "real" value. Since the definition of PID-electrons and "all electrons" is independent of any zero-scale, the final efficiency remains unaffected.

The same methodology can be used in order to obtain the PID purity. If the amount of background (B) within the electron track candidate sample can be determined, then the purity is defined as

$$\rho_{PID} = \frac{\mathrm{S}}{\mathrm{S} + \mathrm{B}}, \tag{4.5}$$

where S is the signal, i.e. actual electrons. This can be estimated from the Gaussian fits in the right plot in Figure 4.17. S is equal to the Gaussian area of the blue fit from -1.5 to 3.0 in nσ. B is the amount of hadron, or gray Gaussian, that leaks into the electron sample, i.e the area of the gray Gaussian within -1.5 to 3.0 nσ.

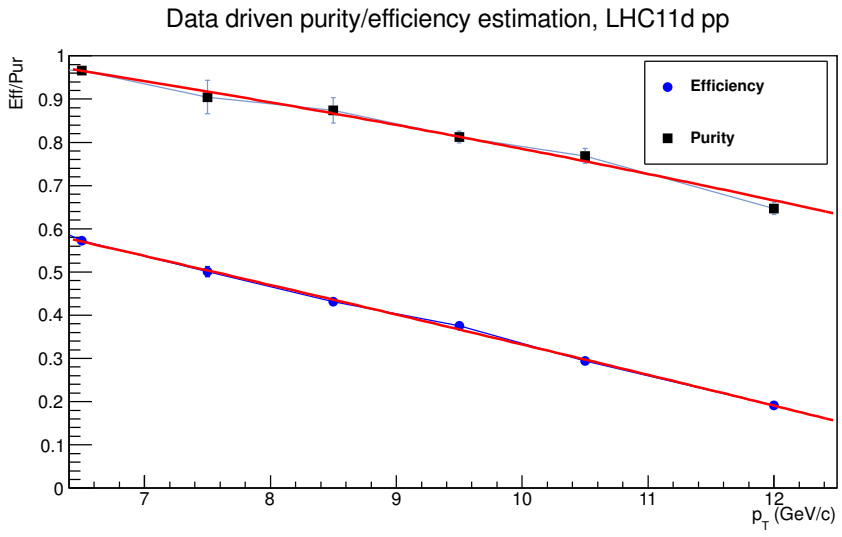

Figure 4.19: PID purity and efficiency as estimated from data. The red lines are fit to the curves and used in the correction step.

When performing these Gaussian fits a lot of care has to be taken into account. It is important that the global fit error is minimized and that the electron peak is centered properly close to zero. As momentum increases, the Gaussian peaks merge together, see Figure 4.18. This causes the fitting to be unstable. Also, the definition of "all electrons" might be contaminated by hadrons; if the hadron Gaussian stretches past zero nσ, then the assumption that all tracks above zero are electrons fails. This becomes a problem for the high momentum bins, thus the definition there is slightly changed to take the 1/3 of the upper nσ electrons, and multiply by three. This includes finding the nσ value when integrating from this point to infinity and one obtains exactly 1/3 of the area of the Gaussian. The result of this method can be seen in Figure 4.19, where the purity and efficiency are shown. The errors indicate how well the Gaussian functions were fitted, which is a statistical error to be propagated and included in the final correction steps. Fits have been made to the estimated purity and efficiency; these lines will later be used to correct for any p_T bin.

The purity of the electron sample is not necessarily needed for any b-tagging analysis. Since the b-tagging is performed on selected electron candidate tracks, a new sample of tracks is obtained, b-electron candidate tracks. The purity of this track population relative to hadrons is different due to the b-tagging algorithm which preferentially selects (b-)electrons. This is explained and performed in Section 5.3.2.

4.3.4 Purity - EMCal

There is another method to estimate the purity of the electron candidate sample. One can look at the E/p distribution to deduce the fraction of electrons versus hadrons. Hadrons most of the time deposit little or no energy, thus forming a "background" in E/p, while electrons deposit most or all of their energy, yielding an E/p close to unity. To estimate the purity, as an approximation, the background can be fitted as an exponential background, and the electron peak with a Gaussian function, a crystal-ball [116] or a double-crystal-ball function. The Gaussian function assumes a normally distributed E/p for electrons around 1, but this is not necessarily true since the electron can have "incorrect" momentum, can get matched to the wrong track or if another track hits nearby the cluster can have erroneous energy. This can be modeled with a Gaussian function along with an energy-loss "tail" which is called the crystal-ball function. A Gaussian function along with two such "tails" is called a double-crystal-ball function. These various fitting strategies were tried. The simple Gaussian plus exponentially falling background fails since the background has got a structure due to the trigger enhancement effect, causing a non exponential background. See Figure 4.16. The crystal-ball function is defined as

$$f(x;\alpha,n,\bar{x},\sigma) = N \cdot \begin{cases} \exp(-\frac{(x-\bar{x})^2}{2\sigma^2}), & \text{for } \frac{x-\bar{x}}{\sigma} > -\alpha \\ A \cdot (B - \frac{x-\bar{x}}{\sigma})^{-n}, & \text{for } \frac{x-\bar{x}}{\sigma} \leq -\alpha \end{cases} \tag{4.6}$$

where

$$A = \left(\frac{n}{|\alpha|}\right)^n \cdot \exp\left(-\frac{|\alpha|^2}{2}\right) \tag{4.7}$$

and

$$B = \frac{n}{|\alpha|} - |\alpha| \,. \tag{4.8}$$

However, the single crystal-ball function fails since there are plenty of tracks with E/p greater than 1. The double-crystal-ball function has got 10 free parameters, and fitting this is tedious but can be done. It however gives a large error and is very unstable [6].

Instead of using fitting functions one can estimate the purity by studying the background. This background is generated by hadrons that are randomly paired up to a cluster. Since the trigger is blind to particle species it also enhances the

[6] By using a large number of free parameters one can get almost whatever one wants. This gives an unstable estimate for the purity. When you come to think about it, the silhouette of an elephant can be fitted using a function with 10 free parameters!

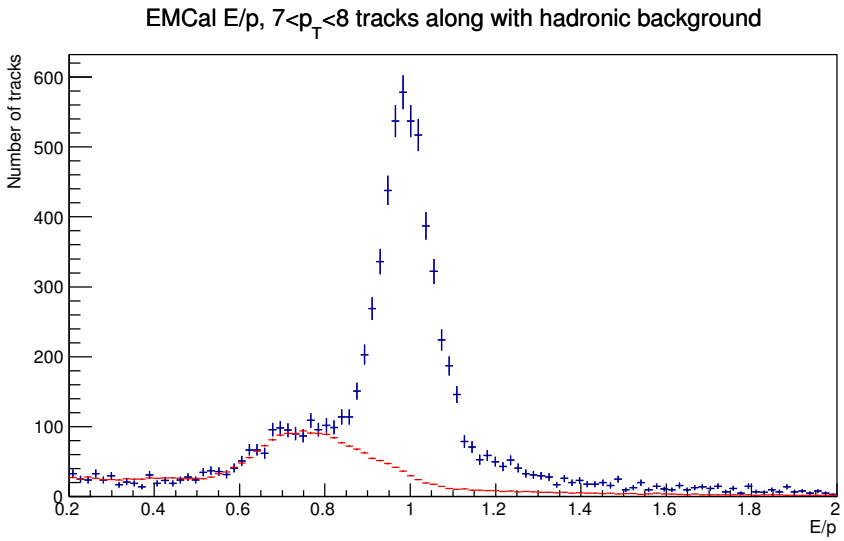

Figure 4.20: Data-driven E/p method to estimate the purity of an electron sample. The red line are pure hadrons (mostly pions) that have been randomly matched to clusters. This is the dominant reason for the background structure at lower E/p. By scaling the hadron background to fit the lower E/p region an accurate purity can be obtained.

number of high momentum pions. Pions can be selected by the use of TPC energy loss; they are far more abundant than electrons, thus getting a pure pion sample is not a problem. Selecting pions with an nσ of about -5 to -3 one can construct the background part. This can then be linearly scaled with *one* parameter to fit the low E/p region which is dominated by these background pions. Comparing a method that has got one free parameter with a method that has got 10 free parameters is of course amusing; the introduction of a trigger forced this data-driven one-parameter purity estimation method to be invented since all other previous methods failed or gave bad results. Since the function-fitting method relies on attempting to approximate reality with an artificial function, it will always fall short in comparison with a data-driven method. In the end the data-driven method has now become the standard method to estimate the purity of an EMCal electron candidate sample within ALICE. In Figure 4.20 this method is illustrated. This is done in detail in Section 5.3.2 for b-electrons. For electrons the purity was investigated and found to be in agreement with the calculated TPC-EMCal nσ purity. This was also the case for the double-crystal-ball function fit method, although the errors were larger. In the end the inclusive electron purity was never used, so the TPC-EMCal nσ purity is sufficient for cross-checking purposes.

Table 4.4: Summary of all PID cuts used in the electron level analysis.

Electron Selection Cuts	
EMCal acceptance ϕ	$79 \leq \phi \leq 191°$
EMCal acceptance η	$-0.7 \leq \phi \leq 0.7$
Transverse momentum	$7.0 \leq p_T \leq 12.0$ GeV/c
TPC $n\sigma_e$	$-1.5 \leq n\sigma_e \leq 3.0$
Cluster-track residual	$\Delta\phi < 0.05°$
	$\Delta\eta < 0.025$
EMCal $E_{cluster}/p_{track}$	$0.85 \leq E_{cluster}/p_{track} \leq 1.3$

4.4 Trigger correction

The EMCal Level-0 trigger extends the p_T reach of jets, electrons and direct photons. It is a fast trigger that sums the energy in a 4 $\times$ 4 tower window which slides over the entire EMCal with a 2-tower step. It sums the ADC signal before it is converted to energy, which is linearly proportional to energy as explained in Chapter 3.1. If any of these sums are larger than a threshold then the trigger signal will be issued and the event recorded. Due to small differences in the ADC-to-energy conversion factors this triggered on events with a trigger patch energy sum greater than about 5.0 GeV for the 7 TeV proton-proton LHC11d period. Since this threshold gives an increased yield of events around and greater than this threshold it is only safe to use events above this threshold, which is above about 7 GeV for the LHC11d period.

Since the trigger selects only certain events, effectively enhancing the statistics in the higher p_T region above the trigger threshold, the cross section involved in these processes are naturally different than compared to a minimum-bias spectrum. In fact, the trigger introduces two modifications to the spectra; first it off-sets the spectra by a trigger enhancement factor and second the spectrum is modulated by the trigger efficiency. The trigger efficiency ranges from 0 to 1 where it is 0 for p_T well below trigger and 1 for well above the trigger threshold. It can be modeled with an error function $\mathrm{erf}(x) = \frac{2}{\sqrt{\pi}} \int_0^x e^{-t^2} dt$ or similar turn-on curves. Problems can arise if the trigger efficiency does not approach 1 at energies above the threshold. This happens when a particle with larger energy than the trigger threshold does not set off the trigger. This can occur for example when the geometry of the detector and the trigger window are in such dimensions that all the deposited energy of a particle is never fully contained in any of the trigger patches; this has to be accounted for. This can also be the case in measurements of jet spectra, where the trigger efficiency

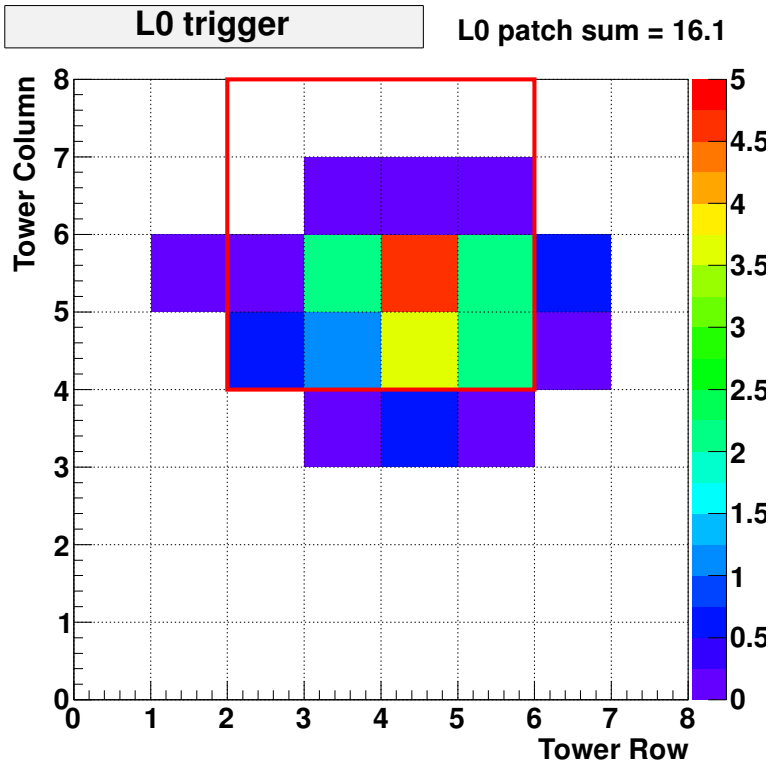

Figure 4.21: The L0 trigger patch sliding a 4 × 4 tower window over a real electron shower event in the EMCal test module. It moves by 2 towers each slide and integrates everything within the window to deliver a trigger decision on ADC level.

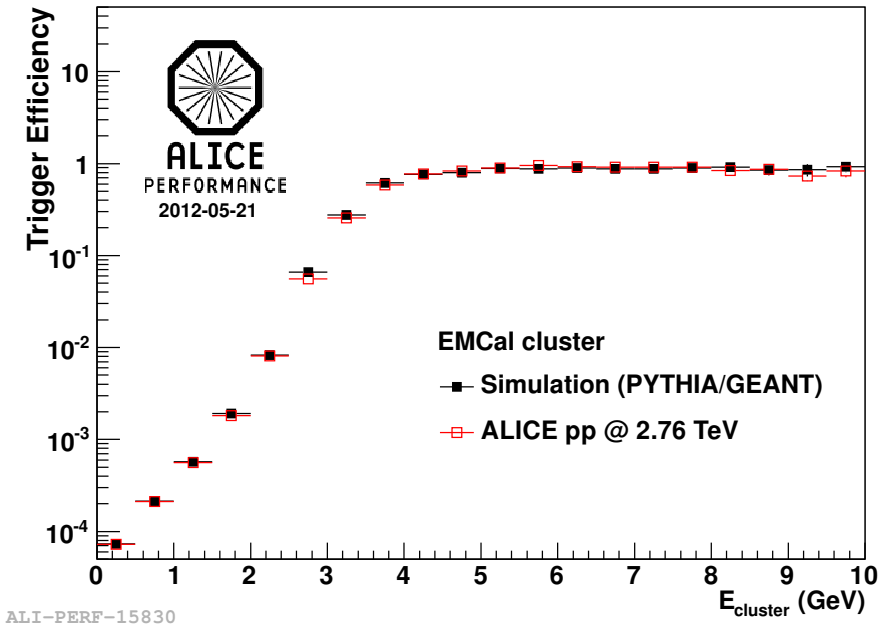

Figure 4.22: Trigger efficiency for LHC11a. Trigger threshold was set at about 3 GeV. Black data points are EMCal-L0 trigger efficiency for EMCal clusters calculated via simulation. Red points are a comparison using real data.

slowly goes to 1. For tracks, clusters, and electrons in particular, simulations show that the efficiency reaches 1 pretty fast after the trigger threshold. Simulations can only currently be done semi-data-driven, meaning one needs minimum-bias data and triggered data to model the actual trigger. Then this model of the trigger is applied to simulated minimum-bias data, and the trigger efficiency can be determined. This was done on clusters for LHC11a since there was enough minimum-bias data to obtain the trigger response in the separate super modules individually, see Figure 4.22. For LHC11d this was not possible to repeat the simulation process since there is not enough minimum-bias data, but the same applies for all proton-proton data sets, thus it is assumed that the trigger efficiency is 1 for p_T above the trigger threshold of about 5 GeV. That the cluster turn-on curve is similar to the electron turn-on curve was confirmed in PbPb measurements where enough statistics in minimum-bias, triggered data and electrons could be obtained [117].

The trigger offset must be calculated in relation to the minimum-bias spectrum since the cross section is measured for minimum-bias events [7]. The spectrum used

[7] Actually the minimum-bias cross section cannot directly be measured, but the cross section for the VZero trigger is measured and then the minimum-bias cross section can be obtained from there.

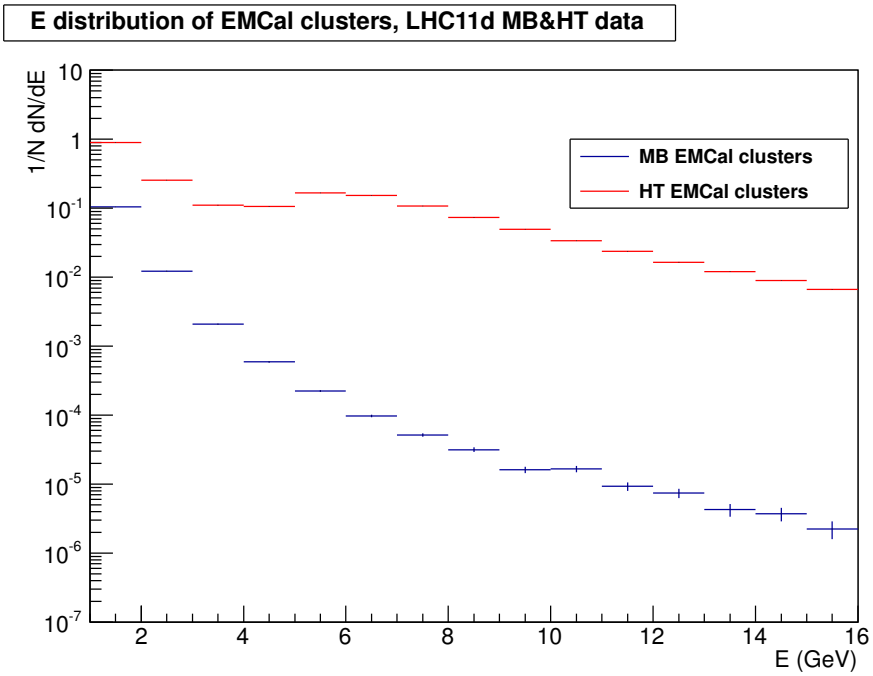

Figure 4.23: All clusters for MB and HT triggered events, normalized by number of events.

in order to determine this distribution should in the ideal case be fully corrected inclusive electrons from both minimum-bias and triggered events. For the 2011 data most of the minimum-bias events were either bad or not reconstructed, so it was not possible to get an overlap of inclusive electrons at high p_T. Instead all EMCal clusters can be used, and a plot of all non-exotic clusters as reconstructed by the V1 + unfolding algorithm for both minimum-bias and triggered data is shown in Figure 4.23.

This offset observed for the triggered events in Figure 4.23 is the trigger enhancement and must be corrected for. The ratio of clusters from the triggered data set and the clusters from minimum-bias data is shown in Figure 4.24 along with a fit in the p_T region of 7-14 GeV/c. The line fitted is at a ratio value of $\varepsilon_{trigger} = 2450$. A 10% systematic error is assigned to all bins for the triggered data set in the calculation of the combined error. A "turn-on" curve of the form $f(x) = A + B\frac{2}{\sqrt{\pi}}\int_0^x e^{-(x-C)^2}dx$ can be used to fit the region, yielding a similar plateau of 2500 at high p_T, while taking into account the turn-on behavior at lower p_T.

See Chapter 7.

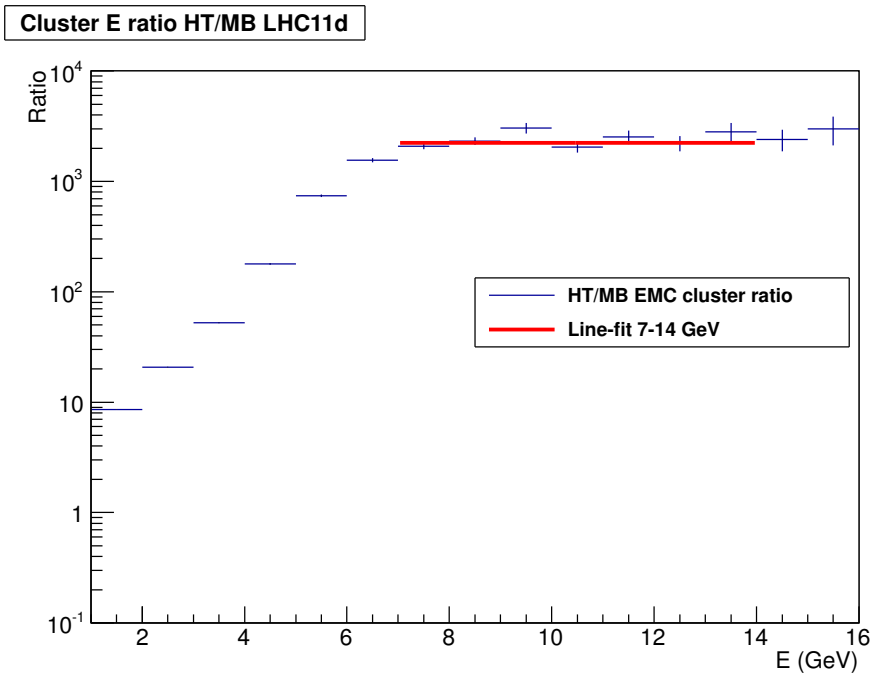

Figure 4.24: Ratio of all clusters for MB and HT triggered events, normalized by number of events, for the 7 TeV data-set, along with a line-fit at high p_T.

Chapter 5

B-tagging

The process of b-tagging is to identify particles that are associated with a bottom hadron decay. In general, the long lifetimes associated with weak-decay processes of b-quarks are exploited in order to "tag" particles coming from bottom decays. The long lifetimes result in average decay lengths on the order of a few hundreds of μm at large momentum. These decays stand out in comparison to the fast strong-force decays and the slower lighter-quark decays. Initially, when b-tagging came of interest b-jets were tagged because the jet axis could be computed with sufficient resolution to distinguish it from the primary vertex. A displaced jet axis would indicate a possible b-jet. With today's high-resolution silicon trackers individual tracks can be separated from the primary vertex and associated with a secondary vertex. Many important physics analyses within high-energy physics are based on b-tagging algorithms, the search for the Higgs boson and top quark physics to name a couple [118]. The b-tagging algorithm developed and used in this analysis is described in the subsequent section. It exploits the large branching ratio of the b-hadron semi-leptonic decay into electrons. Thus, electron identification is the second most important step in the process after the b-tagging algorithm.

Prior to describing the exact algorithm, a word about the strategy in obtaining an invariant production cross section of electrons from a sample of tagged particles is needed. If a perfectly pure b-tag sample can be obtained, the properly normalized invariant cross section of b-electron production can be written as

$$\frac{1}{2\pi p_T}\frac{d^2\sigma_{b\to e^\pm}}{dp_T dy} = \frac{1}{2\pi p_T}\frac{1}{N\Delta p_T \Delta y}\frac{1}{\epsilon}\left[\frac{N_{b-tags}}{\epsilon_{b-tag}}\right]\sigma_{MB}, \tag{5.1}$$

where Δp_T is the bin size in transverse momentum, Δy is the acceptance of the detectors, ϵ_{b-tag} is the b-tagging efficiency, N_{b-tags} is the raw and perfectly pure count

of b-tags (electrons labeled as coming from bottom decay), N is the number of events and σ_{MB} is the minimum-bias cross section associated with the collisions. ϵ is the combined efficiency which consists of the tracking efficiency ϵ_{trk}, the PID efficiency ϵ_{PID} and the trigger offset $\epsilon_{trigger}$: $\epsilon = \epsilon_{trk}\epsilon_{PID}\epsilon_{trigger}$. These have all been defined and measured in previous chapters. The missing piece lies in the ϵ_{b-tag} efficiency. This is unavailable from data-driven methods and thus MC simulations are used. The kinematics describing these processes are sufficiently well known for simulations to describe reality adequately.

In reality, no b-tagging algorithm coupled with any detector resolution will produce a pure b-tagged sample without contamination. Thus, background must always be accounted for. The background can be divided into two categories: hadrons and electron sources. For hadrons a data-driven method can be used to distinguish electrons from hadrons. The methods discussed in Chapter 4 to determine electron versus hadron purity, such as the TPC-nσ method or, even better, the E/p parameter method works well. The electron versus hadron purity is then employed by the introduction of a multiplicative factor ρ that removes the hadronic contamination. A hadron contamination of about 1-10% is estimated and removed from the b-tag sample, see Section 5.3.2.

As for the non-bottom-electron background, there are several ways to deal with additional electrons that do not originate from a b-decay. This is described in Section 5.3.2 where four different methods are discussed, most of them similar to one another in that MC simulations are a necessity and a hypothesis of the main background is needed. However, investigations indicate that the background mainly consists of electrons from charm. This can be attributed to the relative abundances of electrons from bottom versus charm (or other) along with the efficiency of tagging, or mistagging, such an electron. Other electron sources to consider are mainly conversion electrons, π^0 and η Dalitz decay electrons and electrons from J/Ψ or W decay.

Taking hadronic background and other background electrons into account, the invariant b-electron cross section can then be written as:

$$\frac{1}{2\pi p_T}\frac{d^2\sigma_{b\to e^\pm}}{dp_T dy} = \frac{1}{2\pi p_T}\frac{1}{N\Delta p_T \Delta y}\frac{1}{\epsilon}\left[\frac{\rho_h N_{b-tags} - N_{\text{other-}e^\pm}}{\epsilon_{b-tag}}\right]\sigma_{MB} \tag{5.2}$$

where ρ_h is the electron versus hadron purity, and $N_{\text{other-}e^\pm}$ is the number of background electrons that must be estimated and removed.

5.1 B-tagging Algorithm within ALICE

The b-tagging algorithm developed in this thesis exploits the large branching ratio of about 10% [48] of b-hadrons decaying into electrons plus another hadron or hadrons. The algorithm pairs an electron track and a "hadron" track, called associated hadron, in order to calculate certain parameters associated with this pair. These parameters seek to determine whether a secondary vertex exists that involves these two tracks. It is thus a two-track secondary vertex finder, with a high-p_T electron track as seed. It will take all electrons within an event as a seed and loop through all eligible associated hadrons in order to find a secondary vertex. If all parameters are fulfilled the electron is tagged as a b-electron. Initial attempts involved multi-track algorithms, however the complexity quickly rises with increased number of associated tracks (order of N^n where n is the number of tracks considered). Since this simple method shows a good efficiency coupled with a pure b-electron sample it was deemed adequate. The algorithm was proposed by Mark Heinz in 2008 [119], [99], and was properly formulated and implemented into AliROOT 2010. It draws from CDF b-jet tagging algorithms [120]. The method tried to couple tagged electrons with jets and was not finished or tested on real data. As a part of this thesis the algorithm was completed, optimized and re-written in a C++ class based structure that any analysis task in AliROOT can call in order to deliver a b-tag decision.

5.1.1 Associated Hadron selection

The hadron track, or associated hadron, is any track in the event that first of all satisfies a ΔR cut in $\eta - \phi$ space of 1.0 in relation to the electron track. The name is due to the semi-leptonic decay of b-hadrons into an electron plus typically another hadron. Also most tracks in an event are pions or other hadrons, which is then paired with the electron. The ΔR cut is applied to ensure co-linearity of the hadron track and the electron track, removing excessive background. The hadron tracks have to pass standard ALICE 2011 track cuts, specified in Table 5.1, along with number of ITS hits>3 cut. These cuts are a minimal requirement in any track based analysis within ALICE, along with a good ITS resolution requirement. The p_T of the associated hadron track is also used as a parameter in the b-tagging step where only tracks with transverse momentum above 1.0 GeV/c are accepted.

Type of cut	Value
TPC cluster cut	SetMinNClustersTPC(50)
TPC cluster χ^2	SetMaxChi2PerClusterTPC(4)
Accept Kinks	SetAcceptKinkDaughters(kFALSE)
Require TPC Refit	SetRequireTPCRefit(kTRUE)
Require ITS Refit	SetRequireITSRefit(kTRUE)
ITS cluster requirements	SetClusterRequirementITS(AliESDtrackCuts::kSPD, AliESDtrackCuts::kAny)
DCA z-cut	SetMaxDCAToVertexZ(2)
2D DCA cut	SetDCAToVertex2D(kFALSE)
Vertex sigma cut	SetRequireSigmaToVertex(kFALSE)
ITS cluster χ^2	SetMaxChi2PerClusterITS(36)
Number of ITS hits	nITShits>3

Table 5.1: ALICE track cuts used for selecting hadron tracks to pair with the electron.

5.1.2 B-tagging Parameters

The parameters of the b-tagging algorithm are calculated on an electron-hadron-pair basis. Once an electron track and a hadron track are paired together, the distance of closest approach (DCA) between the tracks, the so called "pair-DCA" or pDCA, is calculated. This will mark the point on both tracks where they are closest to each other. The two pDCA coordinates at each of the tracks are obtained and a "secondary vertex" is formed with the help of a "AliESDV0" vertex class in AliROOT. As the name implies the AliESDV0 class will take two tracks and form a v-vertex. Formation of v-vertices is common in many analyses. The center coordinate of the vertex is calculated from the AliESDV0 vertex, it is weighted according to the two tracks involved, but resides somewhere on the pair-DCA vector. There is yet no quality cut on the vertex, thus any two tracks can form these vertices. One electron can be associated to about 100 "pairs" which are created through a separate class called "AliBtagPair.cxx". Once the secondary vertex has been constructed and the center coordinate obtained, the decay vector $\vec{v}_b$ from the primary to the secondary vertex can be computed. The length, or absolute value, of this vector forms the main b-tagging parameter, namely the decay distance of the b-hadron. It also carries a sign modulation depending on the co-linearity and is called "signed-DCA" or sDCA, which is formulated as

$$sDCA = |\vec{v}_b|\Theta_{sign}, \tag{5.3}$$

where Θ_{sign} is 1 if the angle between the momentum vector of the electron and the secondary vertex vector is less than 90° and -1 if it is greater than 90°. The DCA or sDCA name for the decay vector is somewhat misleading. It is not a DCA, but rather a distance between two vertices. The DCA label is of historical origin when the DCA of tracks or jet-axes versus the primary vertex were calculated and used as the primary discriminating parameter. Sticking to old naming conventions the equivalent cut parameter decay distance is named sDCA.

The sDCA should be sufficiently distanced from the primary vertex, but not too far away to pickup other background sources. The sDCA is usually within a range of 0.1-1.0 mm. The reason for the addition of a sign is to remove background; in most b-hadron decays at high transverse momentum the electron and the associated hadron are somewhat co-linear. If their momentum vectors are not co-linear, in the same hemisphere at the secondary vertex, it is safe to reject the pair as background.

Another definition mentioned in [99] is when the sDCA is given a sign from the dot product of the decay and the electron momentum vector;

$$sDCA = \frac{\vec{v}_b \cdot \vec{p}_e}{|p_e|} = |\vec{v}_b| \cos(\theta_{e^{\pm}-h}), \tag{5.4}$$

where $\vec{p}_e$ is the momentum of the electron at the secondary vertex and $\theta_{e^{\pm}-h}$ is the angle between the secondary vertex vector and the momentum vector at the secondary vertex. This is a sign and cosine modulated distance between the primary and secondary vertex. Furthermore a vertex package called "KF" was used to create vertices. It forms a "KFParticle"-vertex from multiple tracks taking momentum resolution and other parameters into account. The secondary vertex is then recomputed and the distance from the primary to the new secondary vertex is calculated a third time. The sDCA is then formed with a Θ_{sign} applied to the magnitude of the distance vector.

From these three similar versions of sDCA the first and most basic definition was selected. Simulations show no large deviations other than perhaps the KFParticle method having a slight disadvantage. The KFParticle-vertex also had a χ^2-parameter from fitting two tracks to one point. This χ^2 is used equivalently to the pDCA of other vertices. This was attempted but later abandoned due to the wide range of χ^2 values and the difficulty of picking a χ^2 to cut on since it it not a physical quantity, but rather a measure of how well a fit is performed. In the end the first definition was chosen and thus sDCA from now on refers to this parameter.

5.1.3 Rejection of bad secondary vertices

Since a secondary vertex can be constructed with any two tracks some quality must be demanded of the computed secondary vertex. For the "AliESDV0" secondary vertex the distance pDCA between the electron and hadron tracks is used to reject bad secondary vertices; the tracks should originate from the same space point and the pDCA should be within a certain limit. This minimum distance is placed at or close to the resolution of the tracks close to the primary vertex, usually around a few tenths of μm. This is an effective tool to get rid of bad secondary vertices.

The next parameter to cut on is the sDCA parameter. This is the decay length of the b-hadron. For a $B^{\pm}$ hadron τ is about 1.638 ± 0.011 ps which at high momentum translates to an average decay distance of about 490 μm. The sDCA parameter is limited to be within as close to the primary vertex that is allowed up to about 1 mm. Different cuts were attempted and are discussed in Section 5.2.

Once a good secondary vertex is found with an acceptable pDCA and sDCA, two invariant mass M_{inv} calculations are performed. The first is M_{γ} which is used to reject events with photonic characteristics. M_{γ} is calculated with the assumption that both tracks are electrons, i.e. the mass hypothesis is set to $m_{e^{\pm}} = 0.000511$ GeV/c^2 and the cut is placed so that $M_{\gamma} < 0.1$ GeV/c^2 is rejected. This is an effective cut to reject electrons from photonic sources. The second invariant mass calculated is $M_{K-e^{\pm}}$ where one assumes that the hadron track is a Kaon with mass $m_K = 0.493677$ GeV/c^2. This is used to reject charm, for which the dominant branching ratio including an electron is $D \rightarrow e^{\pm}K$. Since the charm quark has a mass of about 1.5 GeV/c^2, a cut is placed to reject everything with $M_{K-e^{\pm}} < 1.7$ GeV/c^2 depending on p_T [121]. See Figure 5.1 for a MC simulation showing the distribution of $M_{K-e^{\pm}}$ for different sources paired up with hadron-tracks.

5.2 Optimization of parameters

Of the parameters listed above, pDCA, sDCA, the invariant masses and the p_T of associated hadrons were extensively investigated, separately and in combination, in order to find an optimal set of cuts. Optimal cuts is a concept that needs clarification. Normally when a statistical measurement is performed, signal S and background B are measured. The goal of optimization is to end up with as much S as possible while minimizing B. Often this is not possible, and one has to make a compromise and strike a balance between S and B. Three different sets of cuts were optimized. First

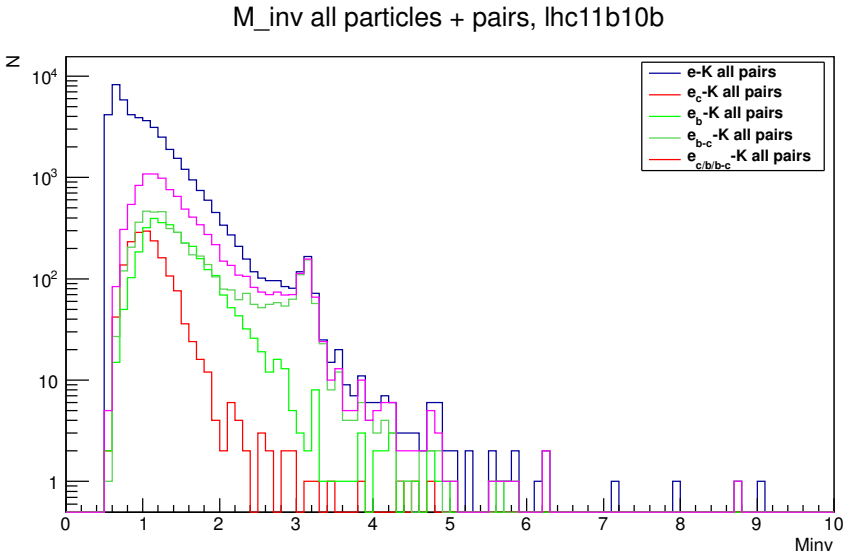

Figure 5.1: The $M_{K-e^{\pm}}$-distribution in a MC simulation, enhanced with electrons from heavy flavor decays.

when assuming normal distributions of both S and B, and their respective errors, the effective signal is the optimal parameter, defined as

$$S_{\text{effective}} = \frac{S}{2B/S + 1}. \tag{5.5}$$

See Appendix A for more details. The statistical error associated with low statistics is put in relation to the inclusion of more background associated with a larger statistical sample. Another optimal parameter that was tested was maximum purity cut, where the ratio of $S/(B+S)$ should be as close to one as possible. The last parameter that was investigated was 90% purity with maximum amount of statistics, i.e. $S/(B+S) > 0.9$ with as many b-tags as possible.

The optimization of these parameters took place within an external framework developed alongside AliROOT. It was written in C++ and took millions of electrons from ALICE MC simulations as input. Simulations had to be minimum-bias events since the relative abundances of the underlying processes producing electrons had to be as close to reality as possible. For every electron (since hadronic background can be removed through data-driven measurements) all the parameters are computed with all the eligible hadrons in an event. The four parameters are varied with 10 discrete steps each, for a total of 10,000 possible combinations for each electron-hadron pair. All information is stored into 4-dimensional matrices, if an electron had a tag or not or if it is truly a b-electron or not for each of the different possible

parameters. Then the different optimizations were undertaken, i.e. find maximum effective signal, maximize purity or maximize statistics with 90% purity. To cope with the large amount of computations and to reduce computation time, parallel computing libraries (OpenMP) [122] were used, utilizing up to 8 cores in parallel when computing, filling and optimizing 4-D parameter arrays.

The effective signal optimization tended to find quite loose cuts, i.e. lots of signal and background. Since the background of the b-tag sample consisted mainly of electrons (hadrons are removed primarily through data-driven methods), the origin of these background electrons is important. If there was only one type of background, say electrons from charm, then optimizing the effective signal would have been trivial. The reason for this is that it turns out that charm can be subtracted in a not too complicated fashion if the background is not too large, but other sources are a bit more complicated, eventually resulting in a form of electron-cocktail subtraction. Thus varying the cut parameters to maximize the effective signal versus electrons from all sources is tricky; if the cuts are too soft, electrons from Dalitz decays will come into play. These are more difficult to remove. It turns out that the cuts for optimized effective signal had a lot of π^0 and η electrons, which caused a lot of problems. In the end for this reason the effective signal is not a good guideline to get the optimal b-electron sample.

The "as pure as possible" cuts, i.e. the maximum purity of the b-tag sample, is a good indicator for a set of cuts. However the cuts turn out to be so hard that not many electrons survive the cuts and the statistics suffer. This is because none of the four parameters used in the optimization step is a clear indicator that the electron came from a bottom decay. Rather a combination of cuts will give a statistical probability that it might originate from a bottom. Maximizing this means to take the "hardness" of the cuts to infinity where only the purest of pure events survive. Instead, one can settle for 90% pure sample, with the largest amount of statistics possible. These cuts were similar to those for maximum purity, however a bit on the loose side. This set of cuts was ultimately selected for the cross section measurement. In addition to these cuts a fourth set of cuts was implemented; "guessed" cuts. This was to serve as a sanity check if a reasonable guess could come close to optimized parameters. Since the four parameters are physical quantities one can form a hypothesis of the individual values. They were not too far away from the optimized ones, perhaps a bit on the hard side, but certainly not catastrophic. The different sets of cuts are summarized in Table 5.2.

Finally it should be stated that the optimization process is done using MC sim-

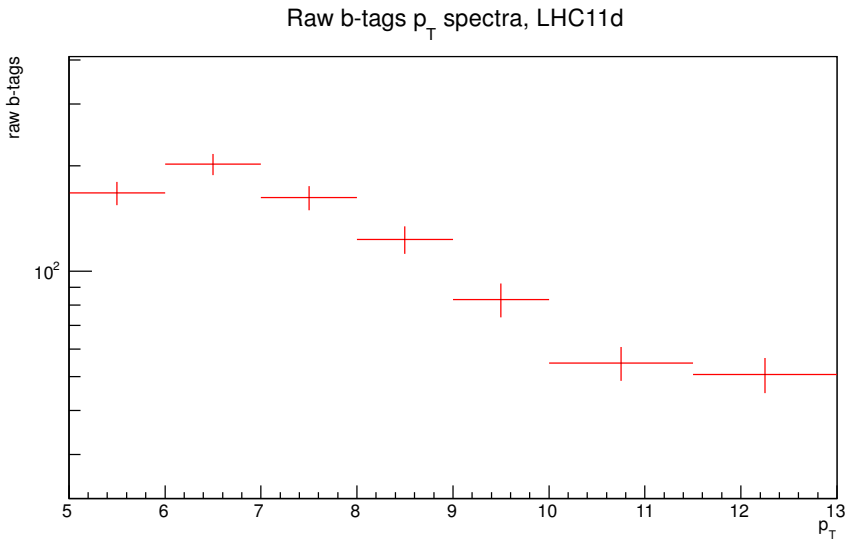

Figure 5.2: Raw b-tags using the 90% pure cuts on the electron candidate sample. The trigger turn-on has been included, and can be seen in the lower amount of b-tags at low p_T.

Table 5.2: Values of the different parameters for the different cut sets.

Cut/Parameter	sDCA (mm)	pDCA (mm)	M_{inv} (GeV/c^2)	p_T^{hadron} (GeV/c)
Pure	0.1-0.8	0.05	1.7	1.0
90% pure	0.09-0.8	0.1	1.75	1.0
$S_{effective}$	0.1-0.8	0.05	1.0	0.5
Guessed	0.05-0.8	0.05	2.0	1.0

ulations, not real data. As such it is at best an approximation of reality, not the absolute final truth. The statistics involved in the optimization process are also not optimal, the infinite limit is the final answer but unfortunately out of reach. Taking these two into consideration, the parameters obtained from the optimization process are merely indicators of what parameters are optimal. In the end however, one will always have background and if there is a method to deal with background then any set of cuts would suffice (in theory). That the set of cuts finally used for the cross section measurement is somewhat optimized is just a nice bonus. The p_T spectrum of raw b-tags can be seen in Figure 5.2.

5.3 B-tagging Background Estimation and Subtraction

Having different sets of cuts that are optimized or close to optimal, the algorithm is then executed on the electron sample obtained from particle identification using the TPC-EMCal. Regardless of algorithm or cuts used in the tagging process there will always be background, and this will now be addressed. As mentioned before one can divide the background into two parts, hadron and electron sources. The hadronic part can be measured using data-driven methods. This is done in Section 5.3.2. The background from electrons originating from other sources than bottom is more difficult to remove. There are no data-driven methods to distinguish electrons originating from charm versus electrons coming from bottom decay. MC simulations have to be used in this step. Several different ways to remove non-bottom electrons were investigated. The sources of these background electrons are mainly from charm, π^0 Dalitz decay and η Dalitz decay. Other sources such as conversion electrons are heavily suppressed due to the nature of the b-tagging algorithm (photonic mass check, high-p_T and the requirement that the track goes back to a secondary vertex close to the interaction point), and are not considered. The amount of background is important to estimate in order to determine how the different components can be removed. This was done through MC simulations. One way to determine the different components of the background is to look at efficiencies. The relative abundances, i.e. production cross section, are not well known so one cannot use purities in MC simulations. Instead the efficiency of tagging, or mis-tagging an electron from a different source can be used since this does not include relative abundances of the different sources of electrons. The efficiency is defined as

$$\varepsilon_x = \frac{N_{x-tagged}}{N_{x-all}}, \tag{5.6}$$

where x is the species of electrons and $N_{x-tagged}$ is the number of tagged electrons, by the algorithm, out of all the electrons originating from that source N_{x-all}. This efficiency is independent of data sample, i.e. MB or enhanced MC simulations does not matter. MC simulations show that electrons from bottom decay have the highest probability to be tagged as coming from bottom, see Figure 5.3. It also shows that electrons from charm do get (mis-) tagged, however, less than electrons from bottom. In the published article from ALICE regarding HFE at 7 TeV pp the ratio of inclusive electrons versus photonic electrons is shown to be about a factor three for large p_T

[123]. This indicates that bottom + charm electrons constitute 2/3 of all electrons, and 1/3 comes from photonic sources at the relevant p_T. The photonic sources are mainly π^0, η and conversion electrons. Conversion electrons are rejected through a photonic electron invariant mass as previously discussed. Simulations show that few conversion electrons survive the cut, so few that constructing a mis-tagging efficiency through a fit of the mis-tagging p_T spectrum fails due to low statistics. As for π^0 and η electrons simulations show that a small fraction of these are mis-tagged, see Figure 5.3, resulting in a mis-tagging efficiency of less than a percent. The contribution is estimated to be less than 2% taking relative abundances of electron sources into account. The same goes for electrons from η with about 1% mis-tagging efficiency; coupled with the amount of electrons from η at this energy relative to bottom electrons it is insignificant. This means that the rejection for electrons from π^0 and η is good, and combined with the actual abundance of these electrons compared with bottom or charm, the total contribution is a few percent or so. Since the systematic error of the tagging algorithm is about 20%, see Chapter 6, these sources are ignored.

The mean-lifetime of J/ψ is of the order of 10^{-21} s. This results in a decay very close to, or within, the primary vertex ($c\tau$ is about 10^{-13} m). The lifetime of the semi-leptonic decay of bottom is orders of magnitude larger, resulting in a $c\tau$ of about 10^{-4} m (as an order of magnitude). The secondary vertex demands the electron-hadron pair to have a secondary vertex away from the primary vertex. This effectively rejects electrons from the primary vertex, including electrons from J/ψ. As with the conversion electrons, simulations have shown that the mis-tagging efficiency is small, so small that it is difficult to construct a mis-tagging efficiency given the available statistics of mis-tagged J/ψ. The same goes for other rapid decays within the primary vertex that produce electrons (strong-force decays, W bosons, etc.).

In summary, hadronic and charm backgrounds are the only backgrounds removed, and the remaining background is deemed small and thus included in the systematic error of the b-tagging algorithm. In the end charm constitutes about 8-12% of the final cross section (depending on p_T) and is removed through subtraction, making electrons from charm the largest contributor of background. This important fact that most of the background electrons come from charm, and the rest can be ignored in a second order approximation[1], gives us the freedom to only focus on one background source.

[1]First approximation would be to even ignore charm, which yields a decent spectrum due to the fact that charm makes up only about 10%

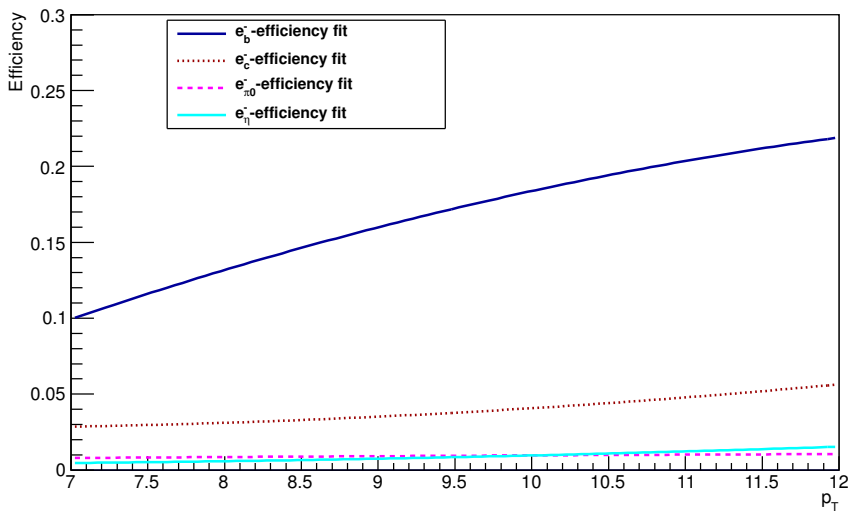

Figure 5.3: Efficiencies as a function of p_T (GeV/c) of the b-tag algorithm on different particles using the 90% pure cuts listed in Table 5.2. The b/c tagging efficiency is obtained from a b/c enhanced simulation, and the π^0 and η efficiencies from a π^0/η enhanced simulation.

5.3.1 Different methods to remove background

The first attempt to remove charm background came from the different sets of cuts that were used to obtain different b-electron samples, along with their respective tagging efficiencies and amount of charm background. Consider two measurements of b-electrons, M_1 and M_2. They have their respective cuts which result in different bottom and charm tagging efficiencies; ε_{b1}, ε_{b2}, ε_{c1} and ε_{c2}. If B is the total number of bottom electrons present before the b-tagging algorithm is executed on all electrons, and C is the total number of electrons present from charm, then the two populations (measurements M_1 and M_2) that result from the two cuts can be written as:

$$M_1 = \varepsilon_{b1} \cdot B + \varepsilon_{c1} \cdot C, \tag{5.7}$$

$$M_2 = \varepsilon_{b2} \cdot B + \varepsilon_{c2} \cdot C. \tag{5.8}$$

B and C are identical in both equations since the only thing that changes are the cuts in the b-tagging algorithm. The efficiencies in both cases are obtained from MC simulations using the definition of efficiency of bottom or charm electrons respectively. The values of M_1 and M_2 are different, and so are the ratios of charm to bottom. Solving for C, yields

$$C = \frac{M_2 - \varepsilon_{b2} B}{\varepsilon_{c2}} \tag{5.9}$$

which can then be used to solve for B,

$$B = \frac{M_1 - \frac{\varepsilon_{c1}}{\varepsilon_{c2}} M_2}{\varepsilon_{b1} - \frac{\varepsilon_{c1}}{\varepsilon_{c2}} \varepsilon_{b2}}. \tag{5.10}$$

This is valid as a function of p_T and has to be calculated on a p_T bin-by-bin basis. This can of course be generalized to higher order if other electron sources need to be taken into account. To solve for N sources of electrons, N different sets of b-tagging cuts are needed. For the two dimensional case with bottom and charm electrons, a third set of cuts can be used to estimate the error involved in the b-tagging algorithm. Three lines in a 2-D plane will form the different measurements, and up to three intersections can be obtained, i.e. one "normal" and two error limits. Note that in the equation solving for B, the denominator contains a subtraction. Not only that, but the subtraction is of two numbers that are of comparable size. This is highly problematic and great precision is needed so that the error of the efficiencies can be minimized, or the resulting error will blow up. Great precision is exactly what is not present in this measurement; the error associated with the b-tagging algorithm is estimated to be around 20%, see Chapter 6. Attempting this estimation on MC data where all the parameters are known yields a huge error, and on data it yields such large variations that the measurement sometimes ends up estimating negative (!) amounts of bottom electrons for certain p_T bins. Clearly, this method cannot be used in the context of this measurement.

The next method attempted, or at least formulated, is one that involves a heavy-flavor electron (HFE) measurement. This has been measured previously in ALICE [123]. The assumption is that the total $T = B + C$ is known. B can then be solved for like before, by using the tagging efficiencies obtained from MC:

$$M = \varepsilon_b \cdot B + \varepsilon_c \cdot C \tag{5.11}$$

$$T = B + C \tag{5.12}$$

$$B = \frac{M - \varepsilon_c T}{\varepsilon_b - \varepsilon_c}. \tag{5.13}$$

Again this involves a subtraction in the denominator, but at least this time it is without the factor $\varepsilon_{c1}/\varepsilon_{c2}$ that makes it even more difficult. The problem with this method is that the total HFE spectrum is only currently measured up to $p_T \sim 7$

GeV/c. That is precisely where the 2011 pp data starts to become usable due to the trigger threshold at 5 GeV. Furthermore, current cocktail methods only reach up to a p_T of about 10 GeV/c.

The third method attempts to use a charm to bottom electron ratio as a corrective term when obtaining a clean bottom electron sample. Again the efficiencies are used as above, and a ratio $r = C/B$ is introduced:

$$M = \varepsilon_b \cdot B + \varepsilon_c \cdot C \tag{5.14}$$

$$r = \frac{C}{B} \tag{5.15}$$

$$B = \frac{M}{\varepsilon_b + \varepsilon_c r}. \tag{5.16}$$

This does not have a subtraction in the denominator, and is a more stable expression. However, the ratio r is needed, along with an error. There have been measurements for this, but no final paper was published. Also the error involved in these measurements tends to be quite large and the ratio is measured up to $p_T \sim 7$ GeV/c.

Finally, instead of guessing a ratio of charm to bottom, a measurement of charm electrons can be used. There are currently a few measurements, none of which quite reach the relevant p_T range for this analysis. However, the measurements follow FONLL predictions quite well, see [124]. The methodology to be used is to try to remove the charm contribution by the knowledge of how many charm electrons were in the electron sample before the b-tagging took place. Then with the help of charm tagging-efficiency the charm background can be removed. A charm electron measurement would then have to be fitted with a function to yield a smooth physical spectrum, adding to the total error. However, if the relative abundance of charm to bottom electrons is small (from the ratio C/B being small, and or the charm tagging efficiency being small), then FONLL predictions can be used directly, since a large accompanying error would be suppressed. Since predictions indicate that bottom electrons are more abundant than charm electrons at 7 GeV/c and the charm tagging efficiency is a factor of 3-5 less than the bottom tagging efficiency, the approximation to use FONLL charm spectrum to remove charm is valid. As a side note, a similar tactic is used when the D meson spectrum is measured [125], but in reverse fashion, i.e. FONLL bottom cross section is used to remove bottom feed-down. Using this tactic the invariant cross section must be rewritten into:

$$\frac{1}{2\pi p_T}\frac{d^2\sigma_{b\to e^{\pm}}}{dp_T dy} = \frac{1}{2\pi p_T}\frac{1}{N\Delta p_T \Delta y}\frac{1}{\epsilon}\left[\frac{\rho_h N_{b-tags}}{\epsilon_{b-tag}}\right]\sigma_{MB} - \frac{\epsilon_{c-tag}}{\epsilon_{b-tag}}\frac{1}{2\pi p_T}\frac{d^2\sigma^{FONLL}_{charm}}{dp_T dy} \quad (5.17)$$

where the last term is the FONLL cross section term that will be subtracted. An additional factor of $1/\epsilon_{b-tag}$ must be inserted in the subtraction term since the raw b-tag yield, including background, is also divided by this amount. Note that the subtraction is on a cross section level, rather than subtracting charm from raw b-tag counts as earlier invariant cross section expressions indicated. This is because performing the subtraction on raw b-tag counts requires the conversion from charm cross section to raw counts (tracking efficiency, PID efficiency etc.), which would introduce more errors associated with each correction step causing the total error to grow quickly. Again by using a charm cross section to estimate the background and subtract, one does not have to postulate a bottom versus charm ratio which is tricky business. This is the final method used to subtract charm electrons. A FONLL pQCD calculation was used along with calculated conservative errors taking the charm electron production uncertainty into account [49].

5.3.2 Electron purity versus hadrons of b-tagged sample

Finally the purity of the electrons versus hadrons of the b-tagged sample ρ_h in equation 5.17 is estimated as a function of p_T through a data-driven method. Since the statistics are poor, and the efficiency is not relevant, the E/p method was selected to determine the electron versus hadron purity. E/p is plotted in p_T slices and one can clearly see the electron peak at unity. There is however some hadronic background as one can see a hint at lower E/p. E/p is plotted for pions and matched to the low E/p region of the b-tagged electron candidate sample. Pions are selected by taking an $n\sigma$ of -5.0 to -3.0, see Figure 4.18. From this the electron versus hadron purity of the b-tagged sample is calculated by taking the ratio of signal over signal and background. This is shown in Figure 5.4 for one p_T slice, and the resulting purity versus p_T can be seen in Figure 5.5 along with a fitted curve.

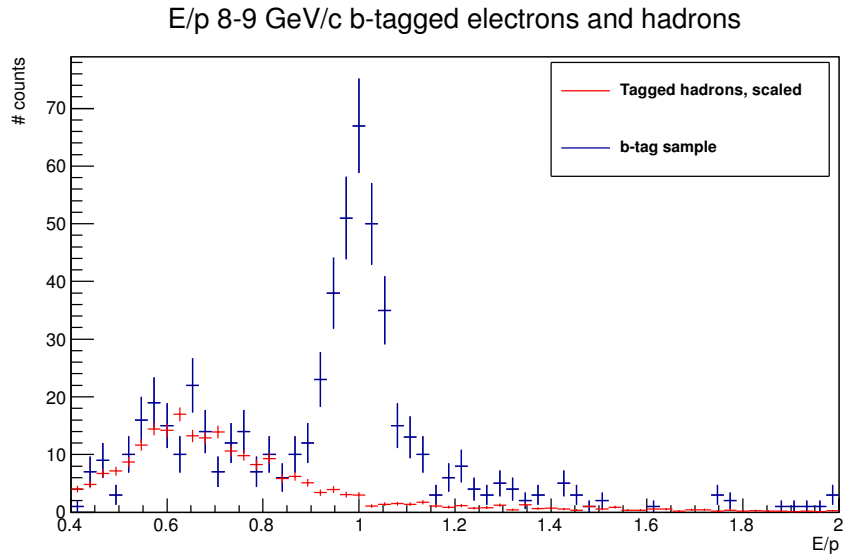

Figure 5.4: E/p for b-tagged sample (mainly electrons) and the corresponding "b-tagged" hadronic background (mainly pions) by b-tagging on tracks from pions. The hadronic background is scaled to fit E/p in the region of about 0.6-0.8.

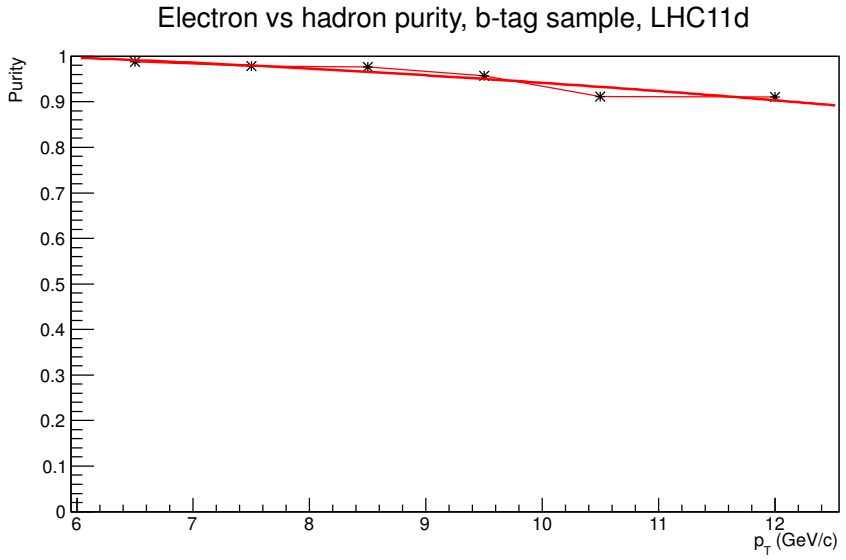

Figure 5.5: Electron vs hadron purity of b-tagged sample as a function of p_T.

Chapter 6

Estimation of Systematic Errors

In this chapter the calculation of systematic errors is described. The tracking and unfolding errors are split in to two parts, the first part being tracking efficiency and unfolding matrix errors combined into one error. The second error is due to the unfolding algorithm itself. The PID error originates from the TPC+EMCal electron selection. Then the trigger correction error is discussed. Finally the b-tagging systematic error is estimated using two methods, this includes the error associated with subtracting background electrons.

6.1 Systematic Errors

The systematic error is the error associated with non-statistical effects that manifest themselves when statistics are plenty but the average of a measurement is different from the actual value. It is an intrinsic error that originates from the measurement itself, such as detector imperfections or bad calibrations, that will not disappear with many measurements. In the context of a cross section measurement the systematic error comes from the detector itself (imperfect machine and calibrations) and for each correction applied to a spectrum the systematic error involved in that step must be accounted for. For example, the particle identification step involves the TPC and the EMCal and their respective PID decisions. They both carry systematic errors and to estimate them, or rather the combined PID error, the raw uncorrected spectrum is corrected with the purity and efficiency obtained in Chapter 5. Then the particle identification decision cuts are changed to become more restrictive, or harder, cuts. The PID purity and efficiency are again calculated, then the raw uncorrected (not identical to the original raw uncorrected spectrum due to cuts that were changed) spectrum is corrected. The process is repeated for a set of loose cuts and a third

corrected spectrum is obtained. If the PID detectors were perfect and the statistics were plenty the three corrected spectra should perfectly match. Any deviation is attributed to the systematic error involved in the PID step. The maximum deviation of the two spectra compared to the original spectrum is plotted as a function of p_T. If there is a trend in the deviation a curve or line will be fitted and symmetric systematic errors are assumed. This method has been applied to tracking, unfolding PID and b-tagging systematic errors. In some cases the different parameters involved in a correction step were varied individually to check for a potential correlation of parameters. All the parameters were found to be without correlation within statistical error and a global error could be computed from each of the correction steps. For the trigger systematic error a flat error is assumed, see Section 6.5.

6.2 Tracking and Unfolding

The tracking efficiency is defined in Section 4.2 as the tracking efficiency of reconstructed particle p_T over MC particle p_T. p_T unfolding is performed to transfer from reconstructed p_T space to real p_T space by use of MC simulations. The tracking efficiency is then dependent on unfolding through the response matrix. For this reason the systematic uncertainty of the tracking efficiency is combined from tracking efficiency and response matrix systematic errors. The p_T unfolding algorithm carries a separate error and is estimated in the next section. To estimate the systematic error the track cuts were varied from hard to loose cuts according to Table 6.1. For each set of cuts a tracking efficiency, a response matrix and a raw spectrum are obtained. Then for each set of cuts the raw yield is corrected by the respective tracking efficiency and unfolded while keeping the unfolding algorithm fixed. The maximum deviation of the spectrum with respect to the original spectrum within a bin is taken as the systematic error as a function of p_T. The corrected raw yield can be any spectrum whose other corrections are uncorrelated to the cuts used to calculate its systematic error. This can be all tracks, electron candidates or b-electron candidates. Here electron candidates were selected as the spectrum to correct. If a spectrum has cuts that depend on the tracking then it is unacceptable; changing the tracking cuts will cause any correlated cuts to also change, often resulting in unrealistically large systematic error.

The cuts varied are the essential cuts involved in selecting a good track sample with reasonable quality. The TPC parameter nTPC Clusters was already discussed in Section 4.2 and found to be significantly different for data and simulation. To

Cuts	TPC clusters	ITS hits	$DCA_{xy}(cm)$	$DCA_z(cm)$
Normal	>100	>2	<2	<3
Hard	>110	>3	<1	<2
Loose	>70	>4	<3	<4

Table 6.1: Values of the tracking parameters for different sets of cuts.

determine to what extent this is a problem, the nTPC parameter was varied and the systematic error calculated. If a cut is placed close to the region where the two parameter distributions are different there is a large systematic error, indicating that the MC-simulated tracking efficiency used to correct the spectrum is incorrect. By placing the nTPC Cluster cut far away from the region where the two distributions are different the systematic error is reduced and it is no longer a problem. The other parameters such as number of ITS hits and track DCA in $x - y$ and z directions were also checked individually and found to be uncorrelated[1]. Therefore a combined change with all cuts varied at the same time is performed and the systematic error is obtained from the resulting tracking-efficiency corrected spectrum.

Figure 6.1 shows the corrected raw yield for the triggered data set along with the systematic error indicated by the blue band. Figure 6.2 shows the error as a function of transverse momentum. Note that the other corrections such as PID and unfolding are kept constant/or not applied since multiplicative factors will not affect the relative offset of the different spectra. This assumes that there are no correlations with the other corrections. The systematic error is quite uniform over the relevant p_T range and a systematic error of 3% is assigned due to the tracking + response matrix.

6.3 Unfolding systematic error

The unfolding algorithm used to unfold the spectrum has an error associated with it; no matter how perfect the response matrix is there will be an error associated with the unfolding algorithm. In an attempt to estimate this error different parameters associated with the unfolding algorithm are changed, in addition to the unfolding algorithm itself. The Bayesian unfolding algorithm's iteration parameter was changed. Also, the SVD unfolding algorithm was used in parallel as a cross check. Table

[1]The correlation of parameters can be checked by looking at the distributions of individual parameters for specific cuts. If a cut on parameter 1 changes the distribution significantly for parameter 2, then parameter 2 is entangled with parameter 1. It is no longer acceptable to place the intended parameter 2 cut when a parameter 1 cut is active.

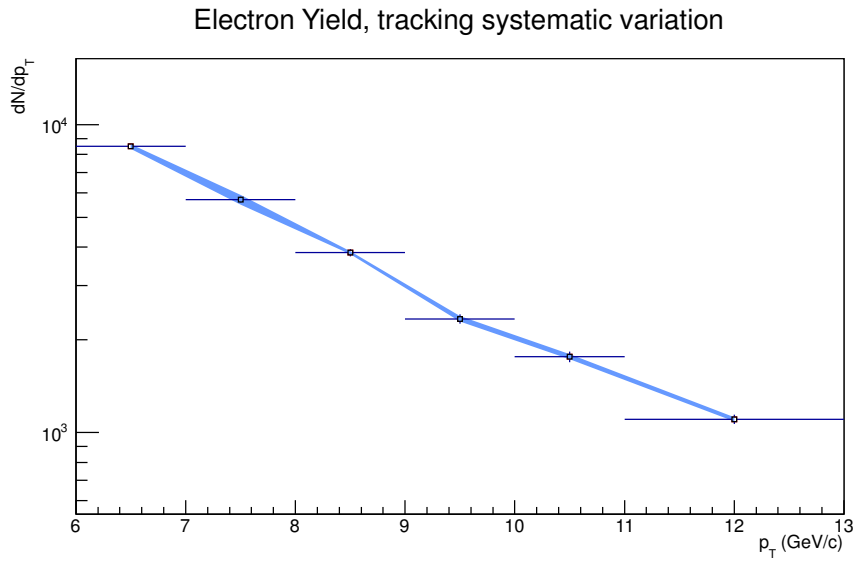

Figure 6.1: The blue band indicates the tracking efficiency plus response matrix combined systematic error.

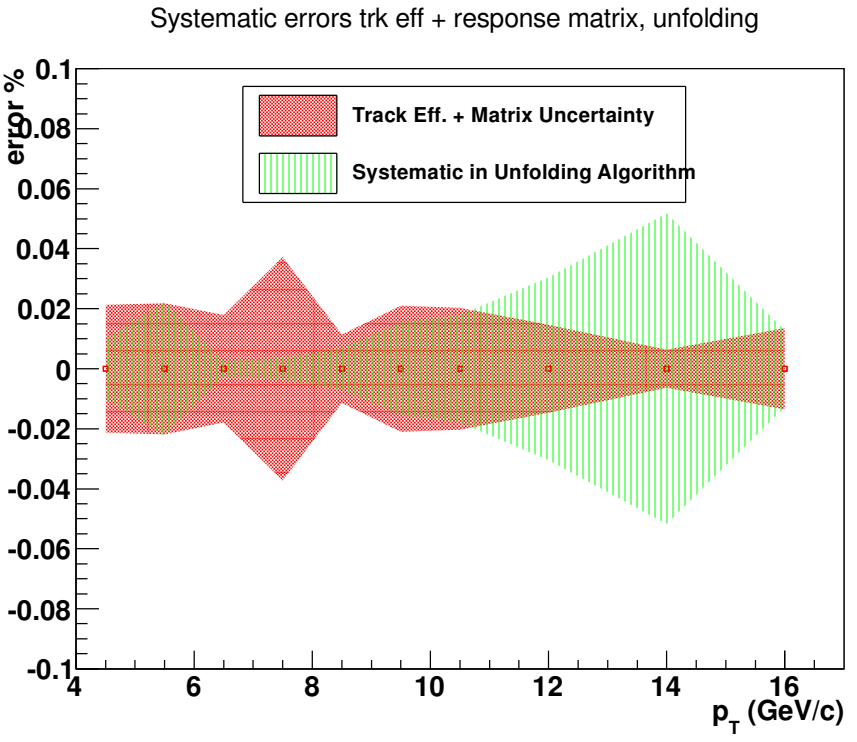

Figure 6.2: Systematic error of tracking+response-matrix and unfolding algorithm.

Algorithm	Iteration parameter value
Bayes	4
Bayes	5
Bayes	10
SVD	15

Table 6.2: Algorithms and parameters used to estimate the systematic error associated with the unfolding algorithm.

6.2 shows the parameters used for the different algorithms in order to estimate the systematic error. The algorithm was varied while all the other corrections were kept fixed resulting in several unfolded spectra. The maximum mutual deviation was again taken as the systematic error, this can be seen in Figure 6.2. The estimated uncertainty is quite uniform and the bin-by-bin deviations are fitted with a line to eliminate statistical fluctuations, and in the end a systematic error of 4% is assigned to the unfolding algorithm.

6.4 PID efficiency systematic error

The systematic error of the particle identification (PID) step includes the correction of the raw electron spectrum with purity and efficiency, since the two are strongly correlated[2]. For this step the relevant PID parameters, $n\sigma$ and E/p, were varied and spectra corrected for each set of cuts. The maximum mutual deviation of the spectra is taken as the bin-by-bin systematic error. This was fitted with a straight line in p_T to smooth out statistical effects in order to obtain a systematic error. Table 6.3 shows the different cut sets and in Figure 6.3 the different cuts in E/p and nσ can be seen for tracks with transverse momentum of $8< p_T <10$ GeV/c. As before the cuts were varied and PID purity and efficiency obtained for each of the cut sets. The respective spectra were then corrected and the maximum mutual deviation can be seen in Figure 6.4 where the blue band represents the systematic error. The error is relatively smooth but increases for large p_T, as expected due to the increased difficulty in separating the pion and the electron Gaussian peaks when determining the efficiency and purities, see Section 4.3. An error of 8% is assigned, except for the last bin which is assigned a 12% error. In Figure 6.5 the error as a function of transverse momentum is shown.

[2]If $n\sigma$ is changed, the distribution of E/p varies. Thus, the resulting efficiency and purity are entangled.

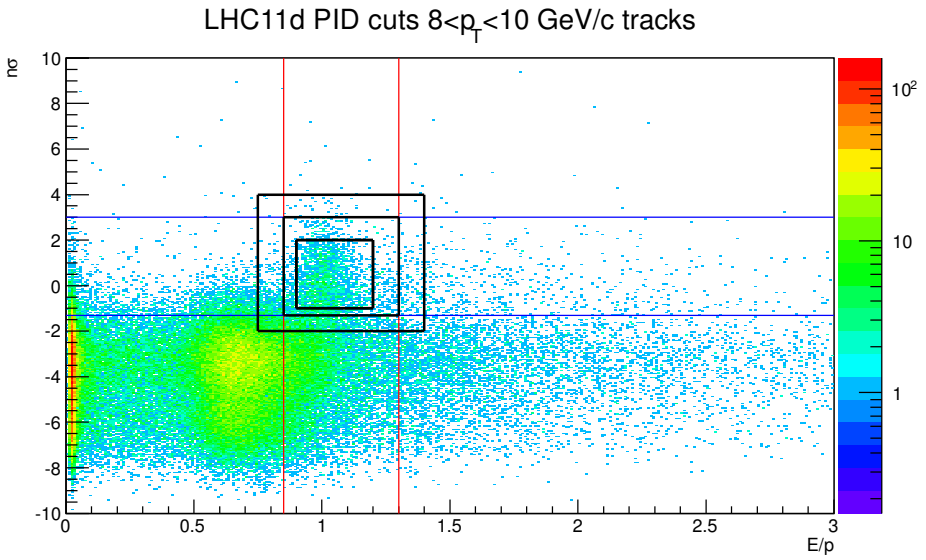

Figure 6.3: PID cuts in E/p and nσ used to determine the systematic error of the PID step. The middle window along with red and blue lines indicate normal cuts.

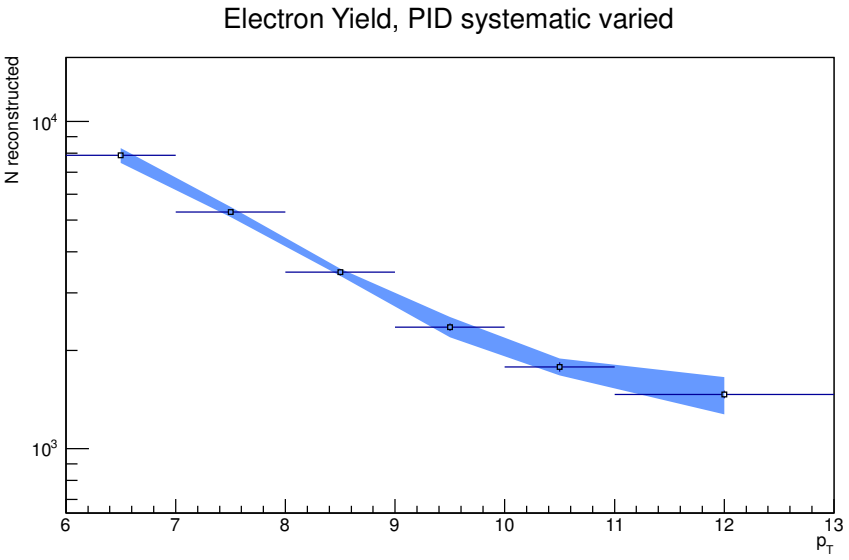

Figure 6.4: The blue band indicates the PID systematic error.

Table 6.3: The sets of cuts used to estimate the PID systematic error.

Cut/Parameter	Normal	Hard	Loose
TPC $n\sigma$	-1.5$\leq n\sigma_e \leq$ 3.0	-1.0$\leq n\sigma_e \leq$ 2.0	-2.0$\leq n\sigma_e \leq$ 4.0
EMCal E/p	$0.85 \leq E/p \leq 1.3$	$0.9 \leq E/p \leq 1.2$	$0.75 \leq E/p \leq 1.4$

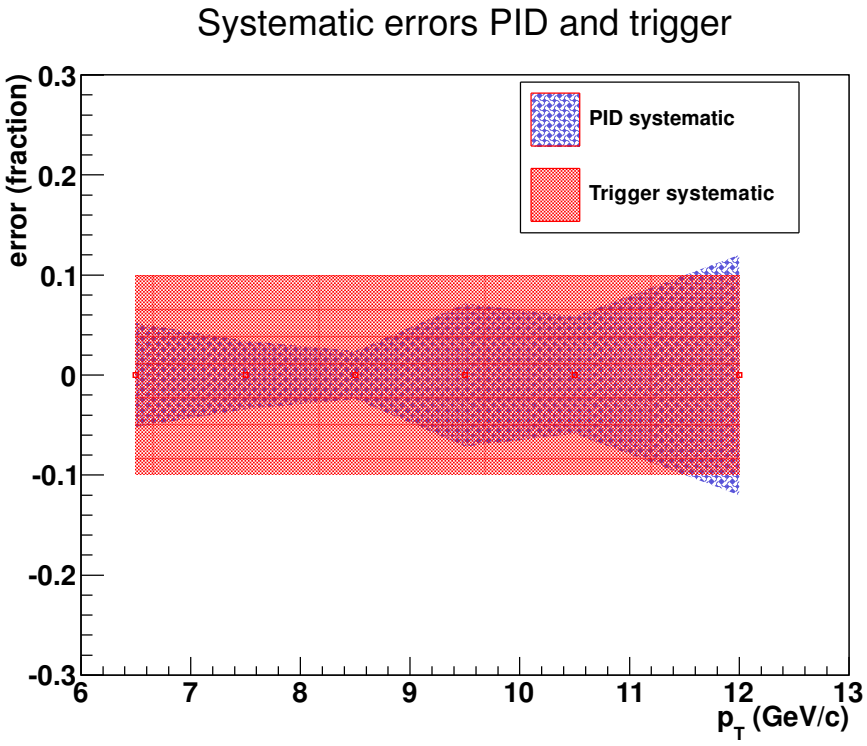

Figure 6.5: Systematic error of PID and trigger correction.

6.5 Trigger Correction

The trigger efficiency and its associated systematic error were discussed in Section 4. The main problem in obtaining this correction is the lack of MB data as a reference. The correction factor should ideally be obtained from fully-corrected inclusive electron spectra from MB and triggered data. Since statistics are lacking, clusters instead of electrons in the EMCal are used, in compliance with the 2.76 TeV pp and PbPb analyses (they both show consistent results indicating that this is a valid method). A simulation for the 2.76 TeV pp data is forthcoming and this may shed more light on the situation. At the present time, a conservative estimate of 10% systematic error is assumed. In Figure 6.5 the error as a function of transverse momentum is shown.

6.6 B-tagging

The systematic errors for the b-tagging step is estimated using the same procedure as for tracking and PID. The b-tagging cuts are varied, new correction functions are obtained and the resulting spectrum is corrected. The relevant corrections, as

Cut	sDCA	pDCA	M_{inv}	p_T^{hadron}
Normal	0.09-0.8	0.1	1.75	1.0
Hard	0.11-0.7	0.07	1.9	1.3
Loose	0.07-0.9	0.13	1.5	0.7

Table 6.4: Algorithms and parameters used to estimate the systematic error associated with the unfolding algorithm.

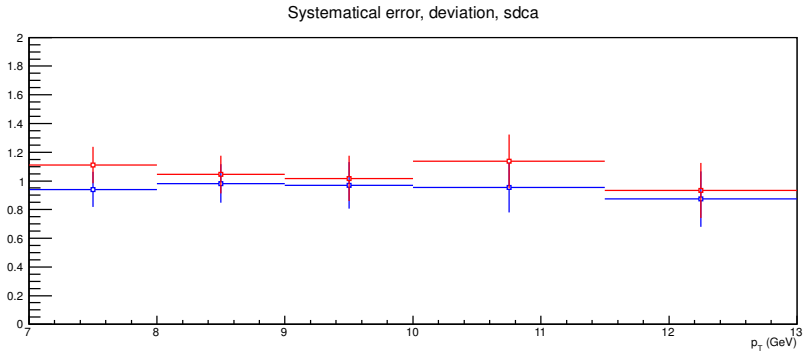

Figure 6.6: Systematic error when sDCA is varied.

discussed in section 4, are electron vs hadron purity, b-tagging efficiency, c-tagging efficiency and charm subtraction. The systematic errors from all these corrections are combined into one due to their mutual dependence through the b-tagging parameters. The different cuts that were used are shown in Table 6.4.

These cuts were varied first separately and then together all at once. As before, this results in different purities/efficiencies and they are each applied to the corresponding spectra. The maximum mutual deviation is taken as the systematic error. When each parameter was varied individually the systematic errors were estimated to be ∼10% for sDCA, ∼3% for pDCA, ∼15% for M_{inv} and ∼10% for p_T^{hadron}. This is shown in Figures 6.6 to 6.9. The combined error is formed through addition in quadrature and results in a total systematic error of about ∼19% for the relevant p_T range. The cuts were also changed simultaneously assuming that the different b-tag parameters are entangled and thus cannot be separated when studying the systematic error associated with the b-tagging algorithm. All the parameters were changed to hard and loose cuts at the same time. This resulted in an estimated systematic error of about 15% and indicates that varying the individual cuts is clearly a more conservative estimate. A 19% systematic error for the entire p_T range was used ultimately.

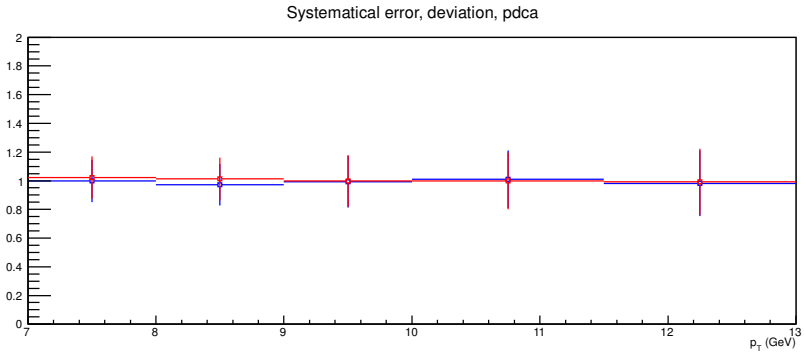

Figure 6.7: Systematic error when pDCA is varied.

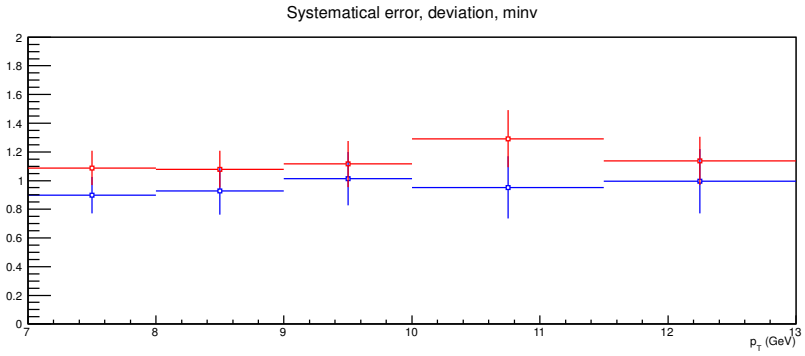

Figure 6.8: Systematic error when M_{inv} is varied.

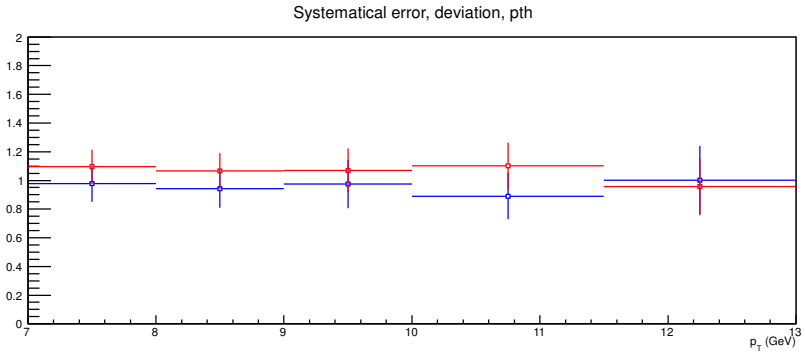

Figure 6.9: Systematic error when p_T^{hadron} is varied.

Correction	Estimated error
Tracking + response matrix	∼3%
Unfolding algorithm	∼4%
PID	∼8-12%
B-tagging	∼19%
Trigger correction	∼10%

Table 6.5: Summary of estimated systematic errors for the different correction steps.

6.7 Combined Systematic Errors

The combined systematic error is calculated by assuming normal-distributed systematic errors and then calculating the combined error by addition in square of the individual errors. For multiplication $Q = a \cdot b$ or division $Q = a/b$ the combined error is given by

$$\frac{\delta Q}{Q} = \sqrt{\left(\frac{\delta a}{a}\right)^2 + \left(\frac{\delta b}{b}\right)^2}. \tag{6.1}$$

Since the errors for all the corrections (except the charm subtraction error) are multiplicative the total error is given by

$$\delta\epsilon = \sqrt{\delta\epsilon^2_{trk} + \delta\epsilon^2_{PID} + \delta\epsilon^2_{trigger} + \delta\epsilon^2_{b-tag} + \delta\epsilon^2_{bkg}}. \tag{6.2}$$

The systematic errors associated with the different corrections are summarized in Table 6.5. For addition or subtraction, done when subtracting charm, the absolute values of the errors are added in quadrature

$$\delta Q = \sqrt{(\delta a)^2 + (\delta b)^2}. \tag{6.3}$$

The error in the charm FONLL cross section is about 50%, thus overly sufficient to compensate for any unknowns. However, since the charm electron mis-tagging efficiency is small compared with the bottom electron tagging efficiency, the error when propagated adds only about 5% overall error.

Chapter 7

Results and conclusion

In this section the final results of the analysis are presented. The cross section before charm subtraction is shown, along with the FONLL charm cross section used for subtraction. Finally the reconstructed b-electron cross section is presented.

7.1 Non-subtracted b-electron cross section

The non-subtracted b-electron cross section is obtained from the raw electron spectra by applying the b-tagging algorithm along with the b-tag, PID, trigger, tracking and unfolding corrections, see Equation 5.17. It is then normalized by number of events, per p_T, per $\eta - \phi$ and by a factor of $1/p_T^{center}$ to give the invariant yield. In order to obtain the b-electron cross section the invariant yield was multiplied with the pp cross section for the relevant energy. Since the trigger enhancement factor has been determined relative to minimum-bias pp events of the LHC11d period in the kINT7 class (VZEROAND), the cross section used for normalization was the kINT7 pp cross section. This corresponds to the VZEROAND cross section, determined in 2010 from a van der Meer scan (54.3 mb $\pm$ 3.5% [126]), corrected by a factor 0.9895 that accounts for the variation of the VZEROAND trigger efficiency from 2010 to 2011[1]. The decrease in trigger efficiency is mainly due to degradation of trigger detector components.

The resulting cross section is shown in Figure 7.1. This is the uncorrected b-electron cross section that is mainly electrons from bottom, a charm component, and a small residue of other electrons[2]. The charm electron component must still

[1] Courtesy of Martino Gagliardi and Ken Oyama.

[2] As discussed previously this residue is mainly from π^0 and η decay. The combined error from these sources is included in the b-tagging systematic error

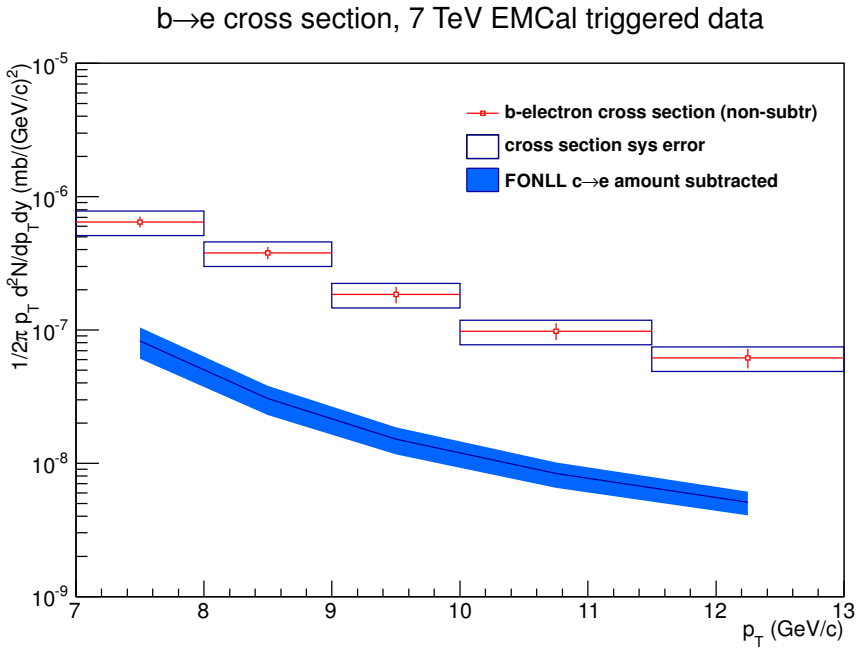

Figure 7.1: Non-charm-subtracted cross section of b-electron production in 7 TeV pp collisions, along with estimated charm background component. The charm background is obtained from a charm electron cross-section FONLL calculation, multiplied by the factor ϵ_c/ϵ_b, see Section 5.

be subtracted from this. This is done via calculating the efficiency of mis-tagging a charm electron and estimating the charm electron cross section. For this purpose a FONLL simulation [49] was used and was multiplied by the charm mis-tagging efficiency and the ϵ_c/ϵ_b factor (see Section 5). The resulting charm component to be subtracted is shown in Figure 7.1 in dark blue. It amounts to about 1/10th of the measured signal.

7.2 b-electron cross section

To obtain the b-electron cross section the subtraction of charm must be done. The predicted charm electron production cross section agrees well with measurements[125]. Since this is a smooth function in the relevant transverse momentum and the amount of charm to be subtracted is small, the FONLL cross section is used for subtraction. The uncertainty in the charm FONLL cross section is propagated to the total systematic error in the subtraction step, to include the systematic error associated with the FONLL prediction. The final spectrum is shown in Figure 7.2 along with a

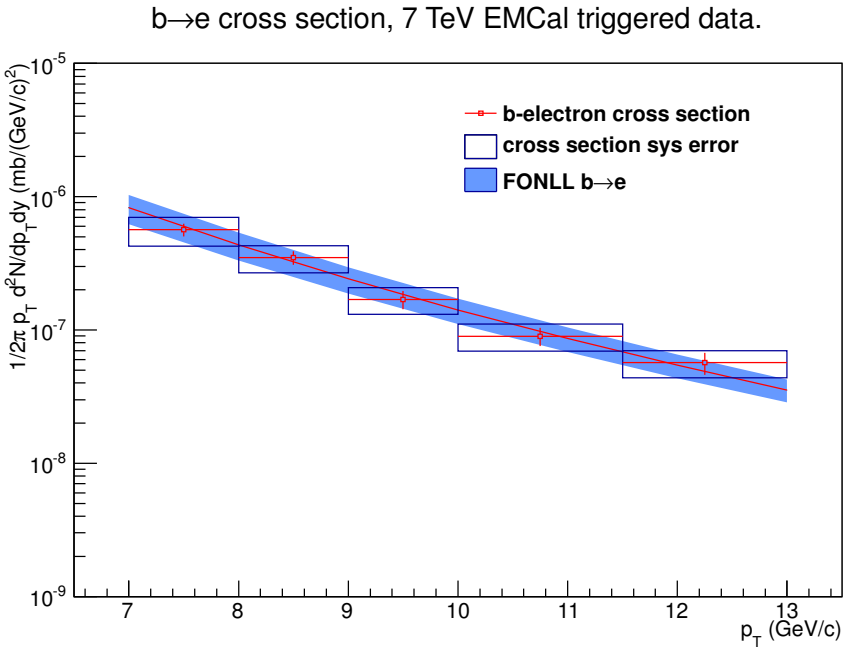

Figure 7.2: Cross section measurement of b-electrons for high p_T in pp collisions at 7 TeV.

comparison with FONLL versus p_T in Figure 7.3.

Finally in Figure 7.4 this is added to the existing and published ALICE bottom electron cross section measurements [124] at lower momenta. The extended b-electron production cross section agrees well with theoretical predictions but there is also internal agreement between the two different measurements. The data point from 7-8 GeV/c was measured by both analyses and agrees within error. The published measurements suffer from bad statistics at this data point, suggesting that the b-electron production at this data point is significantly more than the predicted value. The measurement presented within this thesis suggests that this is not the case. The general agreement of data with predicted values is quite good, considering the cross section measurement spanning four orders of magnitude.

7.3 Conclusion

In conclusion a new method for measuring the bottom electron production was presented, optimized and found to be in agreement with previous measurements and theoretical predictions. The method uses secondary vertices to tag electrons from semi-leptonic bottom decay. The b-tagging algorithm was optimized using the 2011 ALICE EMCal triggered data, along with the EMCal responsible for particle identi-

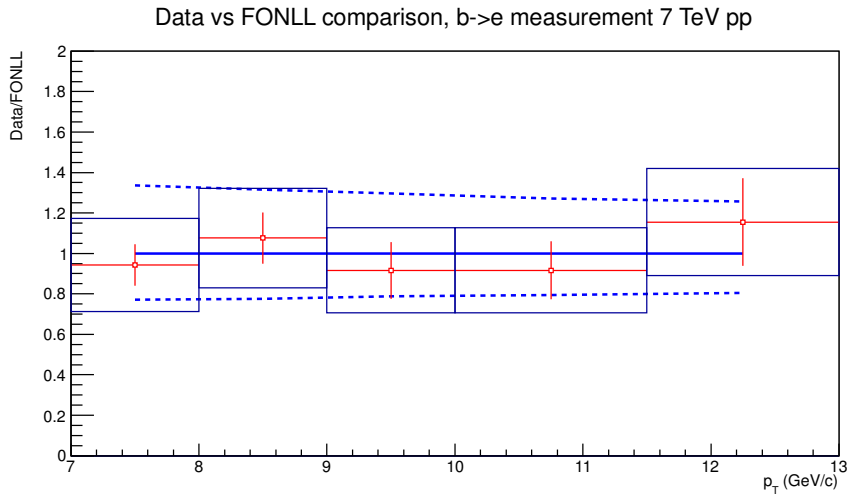

Figure 7.3: Bottom electron production cross section compared to FONLL[49]. The data points are divided by the FONLL prediction. Dashed lines are the corresponding FONLL prediction uncertainty. The boxes are the calculated systematic error and the vertical lines correspond to the statistical error.

fication, to yield an independent method to measure the bottom electron production. Compared to the ALICE measurements at lower transverse momenta [73], the method provides a fast, clean and simple way to measure bottom electrons. In the one overlapping transverse momentum bin the methods agree, which adds confidence to both measurements since they were performed using different data, at a different time and using different sets of sub-detectors. The cross section measurement is also in agreement with current theoretical FONLL models.

The bottom electron production in 7 TeV pp collisions will be used as a reference measurement for a measurement of R_{AA} in PbPb collisions. Since the statistics of the 2.76 TeV pp run are scarce (three days worth of pp data), the 7 TeV pp data is scaled to 2.76 TeV [127]. A very recent preliminary PbPb measurement (reported in May 2014) of the b-electron spectrum at lower momentum in the ALICE detector can be seen in Figure 7.5. This measurement is for the 0-20% centrality bin. When combined with the current ALICE bottom electron production cross section it yields the bottom electron R_{AA}, seen in Figure 7.6.

R_{AA} for pPb in ALICE is shown in Figure 7.7. The bottom electron production appears to be consistent with unity indicating no nuclear effect. The behavior for the bottom electron R_{AA} in Figure 7.6 at higher transverse momentum indicates that the bottom quarks are suppressed and interact with the QGP. To what degree and by which mechanisms is perhaps too early to state. Finally, comparisons with

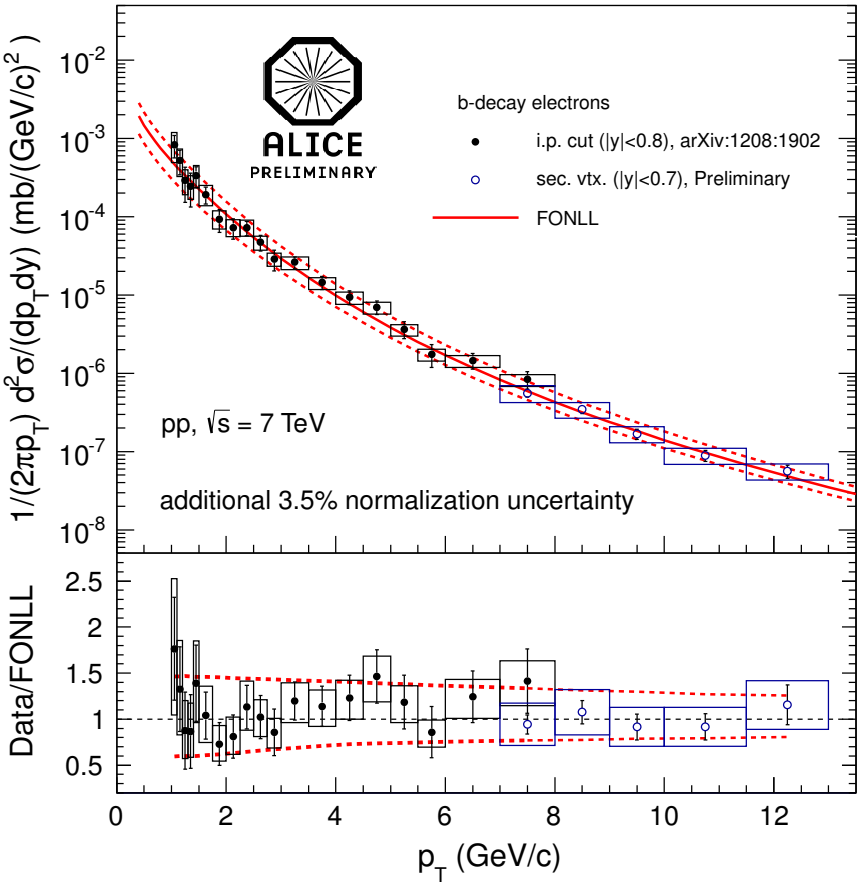

Figure 7.4: ALICE low and high p_T measurements of b-electron cross section.

recent charm measurements [128] seem to suggest that charm is more suppressed than bottom, perhaps in agreement with theoretical predictions. However, to draw any final conclusions a more careful investigation of existing data will need to be done. At least double the data exist (including year 2011 PbPb data at the LHC), along with specific triggers such as the EMCal which can extend the p_T range to much higher transverse moments, which might shed light on the heavy quark suppression in a QGP and also more specifically on mechanisms responsible for energy loss. The pp measurement, partly obtained through this thesis, allows construction of the bottom electron R_{AA} up to 13.5 GeV with reasonable accuracy once the b-decays from the PbPb data are completed. Perhaps even b-jets and the b-jet R_{AA} can be measured with a modified version of this b-tagging method in the future; it is certainly possible within simulation.

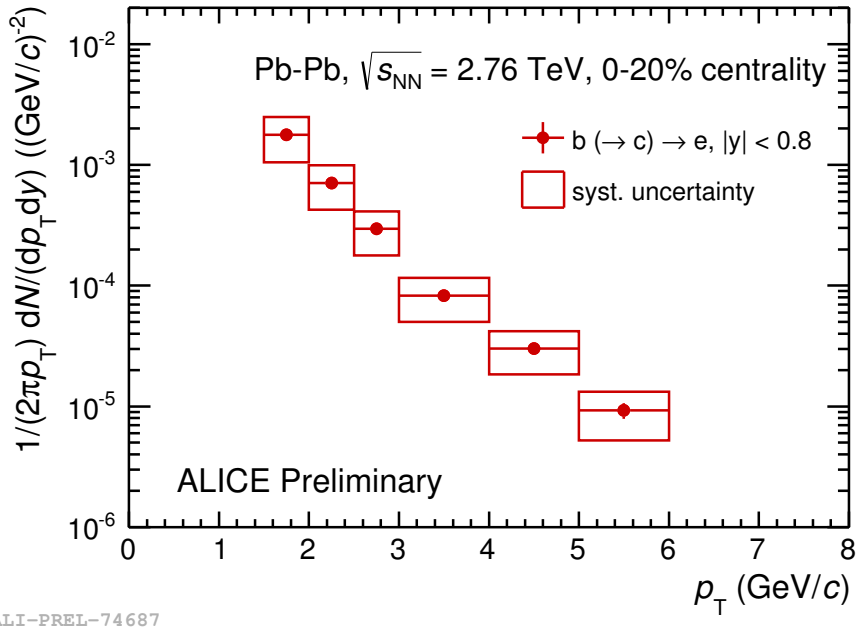

Figure 7.5: ALICE low p_T bottom electron cross section as measured using an impact parameter method, following the methodology in the published low p_T bottom electron cross section [73] measurement. The data are from 2010 2.76 TeV PbPb collisions, in the 0-20% centrality bin[128].

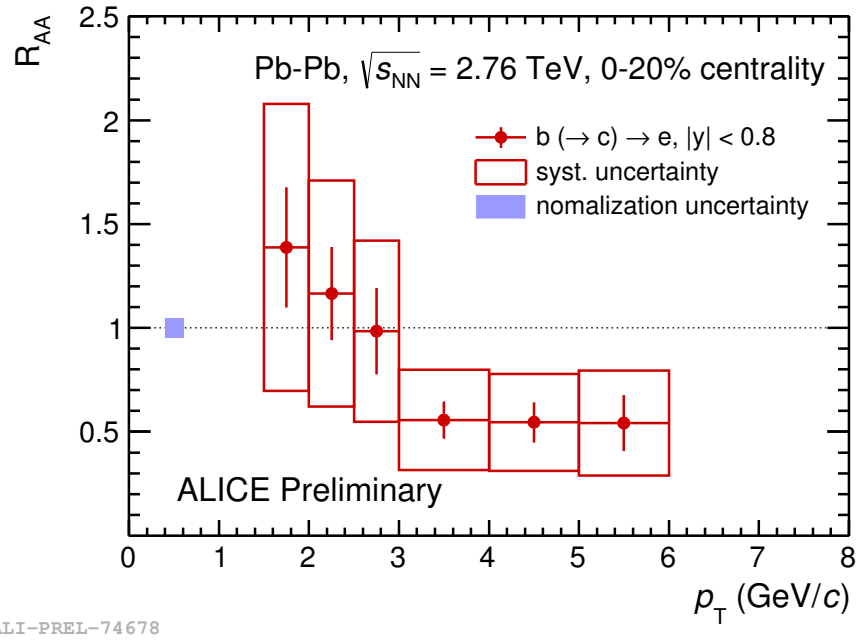

Figure 7.6: ALICE low p_T bottom electron R_{AA}. Source: ALICE repository.

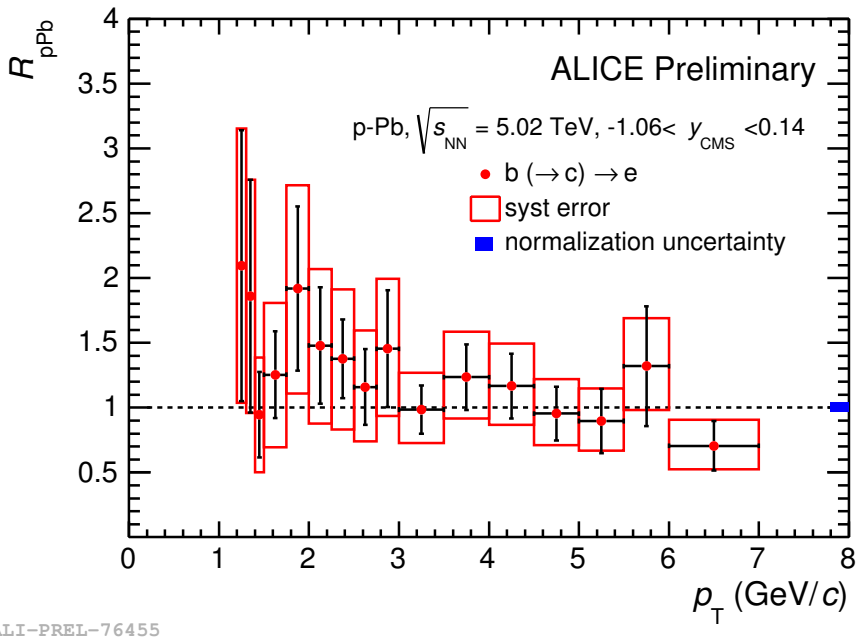

Figure 7.7: ALICE bottom electron R_{pPb} as a function of p_T, as measured from the pPb run at the LHC in 2013. Source: ALICE repository.

Appendix A - Effective Signal

The effective signal is defined as

$$S_{effective} = \frac{S}{2\frac{B}{S}+1} \tag{7.1}$$

If T is the total counts of a measurement and S is the actual signal and B is the background, then

$$S = T - B. \tag{7.2}$$

In the context of b-tagging, S would be correct b-tags and B would be other particles mistagged as a b-electron. The significance is comonnly given as $S/\delta S$. Assuming gaussian errors in equation 7.2, δS can be written as

$$\delta S = \sqrt{\left(\frac{\partial S}{\partial T}\delta T\right)^2 + \left(\frac{\partial S}{\partial B}\delta B\right)^2} \tag{7.3}$$

Assuming gaussian errors $\delta S = \sqrt{S}$ and $\delta B = \sqrt{B}$ and $T = S + B$, this can be written as

$$\delta S = \sqrt{S + 2B}. \tag{7.4}$$

This is true if one assumes gaussian error on the background. If this is not the case, then this turns into $\delta S = \sqrt{S + B}$. Using 7.4 the significance can be written as

$$\frac{S}{\delta S} = \frac{S}{\sqrt{S + 2B}}. \tag{7.5}$$

The significance in the absence of any background is given by $S_{eff}/\delta S_{eff} = S_{eff}/\sqrt{S_{eff}} = \sqrt{S_{eff}}$. In the case with background, assuming the same significance, the effective signal can be written as

$$\frac{S}{\delta S} = \frac{S_{eff}}{\sqrt{S_{eff}}} = \frac{S}{\sqrt{S + 2B}}. \tag{7.6}$$

This gives

$$S_{eff} = \frac{S}{2B/S + 1} \tag{7.7}$$

which is the definition of effective signal assuming gaussian errors of both signal and background.

Bibliography

[1] K. A. Olive, "The Quark-Hadron Transition in Cosmology," *Science 251, 1194*, 1991.

[2] BRAHMS Experiment, "Quark-gluon plasma and color glass condensate at RHIC the perspective from the BRAHMS experiment," *Nuclear Physics A*, vol. 757, no. 12, pp. 1–27, 2005. First Three Years of Operation of RHIC.

[3] PHENIX Collaboration, "Formation of dense partonic matter in relativistic nucleus-nucleus collisions at RHIC: Experimental evaluation by the PHENIX Collaboration," *Nuclear Physics A*, vol. 757, no. 1-2, pp. 184 – 283, 2005. First Three Years of Operation of RHIC.

[4] PHOBOS Experiment, "The PHOBOS perspective on discoveries at RHIC," *Nuclear Physics A*, vol. 757, no. 1-2, pp. 28 – 101, 2005. First Three Years of Operation of RHIC.

[5] STAR Collaboration, "Experimental and theoretical challenges in the search for the quark-gluon plasma: The STAR Collaboration's critical assessment of the evidence from RHIC collisions," *Nuclear Physics A*, vol. 757, no. 1-2, pp. 102 – 183, 2005. First Three Years of Operation of RHIC.

[6] M. K. Gaillard, P. D. Grannis, and F. J. Sciulli, "The standard model of particle physics," *Rev. Mod. Phys.*, vol. 71, pp. S96–S111, Mar 1999.

[7] J. Ellis, "Beyond the standard model with the LHC," *Nature*, vol. 448, Jul 2007.

[8] S. Weinberg, "A model of leptons," *Phys. Rev. Lett.*, vol. 19, pp. 1264–1266, Nov 1967.

[9] J. J. Aubert, U. Becker, P. J. Biggs, J. Burger, M. Chen, G. Everhart, P. Goldhagen, J. Leong, T. McCorriston, T. G. Rhoades, M. Rohde, S. C. C. Ting,

S. L. Wu, and Y. Y. Lee, "Experimental Observation of a Heavy Particle J," *Phys. Rev. Lett.*, vol. 33, pp. 1404–1406, Dec 1974.

[10] J. E. Augustin, A. M. Boyarski, M. Breidenbach, F. Bulos, J. T. Dakin, G. J. Feldman, G. E. Fischer, D. Fryberger, G. Hanson, B. Jean-Marie, R. R. Larsen, V. Lüth, H. L. Lynch, D. Lyon, C. C. Morehouse, J. M. Paterson, M. L. Perl, B. Richter, P. Rapidis, R. F. Schwitters, W. M. Tanenbaum, F. Vannucci, G. S. Abrams, D. Briggs, W. Chinowsky, C. E. Friedberg, G. Goldhaber, R. J. Hollebeek, J. A. Kadyk, B. Lulu, F. Pierre, G. H. Trilling, J. S. Whitaker, J. Wiss, and J. E. Zipse, "Discovery of a narrow resonance in e^+e^- annihilation," *Phys. Rev. Lett.*, vol. 33, pp. 1406–1408, Dec 1974.

[11] G. Ross, *Grand Unified Theories*. Addison Wesley Pub Co Inc, 2003.

[12] M. E. Peskin, "Beyond the standard model," *arXiv:hep-ph/9705479*, 1997.

[13] J. D. Lykken, "Beyond the standard model," *arXiv:1005.1676*, 2010.

[14] A. Pomarol, "Beyond the standard model," *arXiv:1202.1391*, 2012.

[15] ATLAS Collaboration, "Observation of a new particle in the search for the Standard Model Higgs boson with the ATLAS detector at the LHC," *Physics Letters B*, vol. 716, no. 1, pp. 1 – 29, 2012.

[16] CMS Collaboration, "Observation of a new boson at a mass of 125 GeV with the CMS experiment at the LHC," *Physics Letters B*, vol. 716, no. 1, pp. 30 – 61, 2012.

[17] M. Peskin and D. Schroeder, *An Introduction to Quantum Field Theory*. Westview Press, 1995.

[18] V. Barnes, *et al.*, "Observation of a hyperon with strangeness minus three," *Phys. Rev. Lett.*, vol. 12, pp. 204–206, Feb 1964.

[19] S. Boffi and B. Pasquini, "Generalized parton distributions and the structure of the nucleon," *arXiv:0711.2625*, 2007.

[20] R. Brandelik, *et al.*, "Evidence for planar events in e+e- annihilation at high energies," *Physics Letters B*, vol. 86, no. 2, pp. 243 – 249, 1979.

[21] Beringer, J., *et al.*, "Review of particle physics," *Phys. Rev. D*, vol. 86, p. 010001, Jul 2012.

[22] S. Bethke, "World summary of α_s 2012," *arXiv:1210.0325*, 2012.

[23] H. D. Politzer, "Reliable perturbative results for strong interactions?," *Phys. Rev. Lett.*, vol. 30, pp. 1346–1349, Jun 1973.

[24] D. J. Gross and F. Wilczek, "Asymptotically free gauge theories. i," *Phys. Rev. D*, vol. 8, pp. 3633–3652, Nov 1973.

[25] Siegfried Bethke, "Experimental tests of asymptotic freedom," *arXiv:hep-ex/0606035*, 2006.

[26] R. Gupta, "Introduction to lattice QCD," *arXiv:hep-lat/9807028*, 1998.

[27] A. Bazavov, T. Bhattacharya, M. Cheng, N. H. Christ, C. DeTar, S. Ejiri, S. Gottlieb, R. Gupta, U. M. Heller, K. Huebner, C. Jung, F. Karsch, E. Laermann, L. Levkova, C. Miao, R. D. Mawhinney, P. Petreczky, C. Schmidt, R. A. Soltz, W. Soeldner, R. Sugar, D. Toussaint, and P. Vranas, "Equation of state and QCD transition at finite temperature," *Phys. Rev. D*, vol. 80, p. 014504, Jul 2009.

[28] J. Cleymans, H. Oeschler, K. Redlich, and S. Wheaton, "Comparison of chemical freeze-out criteria in heavy-ion collisions," *Phys. Rev. C*, vol. 73, p. 034905, Mar 2006.

[29] M. A. Stephanov, "QCD phase diagram: an overview," *arXiv:hep-lat/0701002*, 2006.

[30] A. Poskanzer and S. V. for the NA49 Collaboration, "Centrality dependence of directed and elliptic flow at the SPS," *Nucl. Phys. A661*, p. 341, 1999.

[31] E. S. D. Teaney, J. Lauret, "Flow at the SPS and RHIC as a Quark Gluon Plasma Signature," *arXiv:nucl-th, 0011058v2*, 2000.

[32] STAR Collaboration, "Elliptic flow in Au+Au collisions at $\sqrt{s_{NN}} = 130$ gev," *arXiv:nucl-ex/0009011*, 2000.

[33] M. Gyulassy, *et al.*, "0302077v2," *arXiv:nucl-th*, 2003.

[34] A. Dainese, "Review on heavy-ion physics," *arXiv:1012.4038*, 2010.

[35] R. Snellings, "Elliptic flow: a brief review," *New J. Phys. 13, 055008*, 2011.

[36] U. Heinz and R. Snellings, "Collective flow and viscosity in relativistic heavy-ion collisions," *Annual Review of Nuclear and Particle Science*, vol. 63, no. 1, pp. 123–151, 2013.

[37] R. Averbeck, "Heavy-flavor production in heavy-ion collisions and implications for the properties of hot QCD matter," *Progress in Particle and Nuclear Physics*, vol. 70, no. 0, pp. 159 – 209, 2013.

[38] T. Ullrich, "RHIC Experimental overview - what we have (not) learned. ," *Colliders to Cosmic Rays*, 2007.

[39] A. K. Chaudhuri, "Viscous Hydrodynamic Model for Relativistic Heavy Ion Collisions," *Advances in High Energy Physics, 693180*, vol. 2013.

[40] Yu-Ming Zheng, C.M. Ko, Bao-An Li, Bin Zhang, "Elliptic flow in heavy ion collisions near the balance energy," *arXiv:nucl-th/9906076*, 1999.

[41] D. d'Enterria, "Jet quenching," *arXiv:0902.2011*, 2009.

[42] STAR Collaboration, "Experimental and theoretical challenges in the search for the quark gluon plasma: The STAR collaboration's critical assessment of the evidence from RHIC collisions," *Nuclear Physics A*, vol. 757, no. 1-2, pp. 102 – 183, 2005. First Three Years of Operation of RHIC.

[43] ALICE Collaboration, "Production of charged pions, kaons and protons at large transverse momenta in pp and Pb-Pb collisions at $\sqrt{s_{NN}}$= 2.76 TeV," *arXiv:1401.1250*, 2014.

[44] H. Satz, "Colour deconfinement in nuclear collisions," *arXiv:hep-ph/0007069*, 2000.

[45] NA57 Collaboration, "Recent results from NA57 on strangeness production in p-A and Pb-Pb collisions at 40 and 158 A GeV/c," *arXiv:hep-ex/0405052*, 2004.

[46] ALICE Collaboration, "K*$(892)^0$ and $\phi(1020)$ production in Pb-Pb collisions at $\sqrt{s_{NN}}$= 2.76 tev," *arXiv:1404.0495*, 2014.

[47] ATLAS Collaboration, "Measurement of the centrality dependence of J/ψ yields and observation of Z production in lead-lead collisions with the ATLAS detector at the LHC," *Physics Letters B*, vol. 697, no. 4, pp. 294 – 312, 2011.

[48] K. Nakamura, *et al.* (Particle Data Group), "The Review Of Particle Physics," *J. Phys. G 37. 075021*, 2010.

[49] M. Cacciari, S. Frixione, N. Houdeau, M. L. Mangano, P. Nason and G. Ridolfi, "FONLL Heavy Quark Production," *arXiv:1205.6344*, 2012.

[50] Torbjorn Sjostrand and Stephen Mrenna and Peter Skands, "PYTHIA 6.4 physics and manual," *Journal of High Energy Physics*, vol. 2006, no. 05, p. 026, 2006.

[51] Torbjorn Sjostrand and Stephen Mrenna and Peter Skands, "A brief introduction to PYTHIA 8.1," *arXiv:0710.3820*, 2007.

[52] M. Gyulassy and X.-N. Wang, "HIJING 1.0: A Monte Carlo program for parton and particle production in high-energy hadronic and nuclear collisions," *Comput.Phys.Commun.*, vol. 83, p. 307, 1994.

[53] G.Corcella, I.G.Knowles, G.Marchesini, S.Moretti, K.Odagiri, P.Richardson, M.H.Seymour, B.R.Webber, "HERWIG 6.5: an event generator for hadron emission reactions with interfering gluons (including supersymmetric processes)," *arXiv:hep-ph/0011363*, 2000.

[54] F. Busser, L. Camilleri, L. D. Lella, B. Pope, A. Smith, B. Blumenfeld, S. White, A. Rothenberg, S. Segler, M. Tannenbaum, M. Banner, J. Cheze, J. Hamel, H. Kasha, J. Pansart, G. Smadja, J. Teiger, H. Zaccone, and A. Zylberstejn, "Observation of high transverse momentum electrons at the CERN ISR," *Physics Letters B*, vol. 53, no. 2, pp. 212 – 216, 1974.

[55] C. Albajar, *et al.*, "Beauty production at the CERN proton-antiproton collider," *Physics Letters B*, vol. 186, no. 2, pp. 237 – 246, 1987.

[56] C. Albajar, *et al.*, "Beauty production at the CERN $p\bar{p}$ collider," *Physics Letters B*, vol. 256, no. 1, pp. 121 – 128, 1991.

[57] STAR Collaboration, "Measurements of D^0 and D^* production in p+p collisions at $\sqrt{s}$=200 GeV," *Phys. Rev. D*, vol. 86, p. 072013, Oct 2012.

[58] STAR Collaboration, "Charmed hadron production at low transverse momentum in Au+Au collisions at RHIC," *arXiv:0805.0364*, 2008.

[59] PHENIX Collaboration, "Heavy-quark production in p + p and energy loss and flow of heavy quarks in Au + Au collisions at $\sqrt{s_{NN}}$=200 GeV," *Phys. Rev. C*, vol. 84, p. 044905, Oct 2011.

[60] PHENIX Collaboration, "Nuclear-modification factor for open-heavy-flavor production at forward rapidity in Cu+Cu collisions at $\sqrt{s_{NN}}$=200 GeV," *Phys. Rev. C*, vol. 86, p. 024909, Aug 2012.

[61] STAR Collaboration, "Transverse momentum and centrality dependence of high-pt nonphotonic electron suppression in Au+Au collisions at $\sqrt{s_{NN}}$=200 GeV," *Phys. Rev. Lett.*, vol. 98, p. 192301, May 2007.

[62] STAR Collaboration, "High p_t nonphotonic electron production in p+p collisions at $\sqrt{s_{NN}}$=200 GeV," *Phys. Rev. D*, vol. 83, p. 052006, Mar 2011.

[63] PHENIX Collaboration, "Measurement of bottom versus charm as a function of transverse momentum with electron-hadron correlations in p+p collisions at $\sqrt{s_{NN}}$=200 GeV," *Phys. Rev. Lett.*, vol. 103, p. 082002, Aug 2009.

[64] STAR Collaboration, "Measurement of the bottom quark contribution to non-photonic electron production in p+p collisions at $\sqrt{s_{NN}}$=200 GeV," *Phys. Rev. Lett.*, vol. 105, p. 202301, Nov 2010.

[65] Yu.L. Dokshitzer, D.E. Kharzeev, "Heavy quark colorimetry of QCD matter," *arXiv:hep-ph/0106202*, 2001.

[66] PHENIX Collaboration, "Nuclear modification of electron spectra and implications for heavy quark energy loss in Au+Au collisions at $\sqrt{s_{NN}}$=200 GeV," *Phys. Rev. Lett.*, vol. 96, p. 032301, Jan 2006.

[67] CMS Collaboration, "Measurement of the B^0 production cross section in pp collisions at $\sqrt{s}$=7 TeV," *Phys. Rev. Lett.*, vol. 106, p. 252001, Jun 2011.

[68] CMS Collaboration, "Measurement of the B^+ production cross section in pp collisions at $\sqrt{s}$=7 TeV," *Phys. Rev. Lett.*, vol. 106, p. 112001, Mar 2011.

[69] CMS Collaboration, "Measurement of the B_s^0 production cross section with $B_s^0 \to J/\psi\phi$ decays in pp collisions at $\sqrt{s}$=7 TeV," *Phys. Rev. D*, vol. 84, p. 052008, Sep 2011.

[70] ATLAS Collaboration, "Measurement of the differential cross-sections of inclusive, prompt and non-prompt production in proton-proton collisions at $\sqrt{s} = 7$ tev," *Nuclear Physics B*, vol. 850, no. 3, pp. 387 – 444, 2011.

[71] ALICE Collaboration, "Measurement of charm production at central rapidity in proton-proton collisions at $\sqrt{s} = 7$ tev," *Journal of High Energy Physics*, vol. 2012, no. 1, pp. 1–30, 2012.

[72] ALICE Collaboration, "Measurement of electrons from semileptonic heavy-flavor hadron decays in pp collisions at $\sqrt{s} = 7$ tev," *Phys. Rev. D*, vol. 86, p. 112007, Dec 2012.

[73] ALICE Collaboration, "Measurement of electrons from beauty hadron decays in pp collisions at $\sqrt{s} = 7$ TeV," *arXiv:1208.1902*, 2012.

[74] ALICE Collaboration, "First proton–proton collisions at the LHC as observed with the ALICE detector: measurement of the charged-particle pseudorapidity density at $\sqrt{s} = 900$" GeV," *The European Physical Journal C - Particles and Fields*, vol. 65, pp. 111–125, 2010. 10.1140/epjc/s10052-009-1227-4.

[75] S. Traweek, *Beamtimes and Lifetimes: The World of High Energy Physicists*. Harvard University Press, 1992.

[76] ALICE Collaboration, "Volume 1: The ALICE Experiment," *JINST 3 S08004, IOP Publishing Ltd and SISSA*, 2008.

[77] G. F. Knoll, *Radiation Detection and Measurement*. John Wiley & Sons, Inc., third ed., 2000.

[78] G. Dearnaley and D. Northrop, *Semiconductor Counters for Nuclear Radiations*. John Wiley & Sons, Inc., second ed., 1966.

[79] G. Bertolini and A. Coche, *Semiconductor Detectors*. Elsevier-North Holland, 1968.

[80] R. H. Pehl, F. S. Goulding *Nucl. Instrum. Meth.* **59**, p. 45, 1968.

[81] G. Vanstraelen *Nucl. Instrum. Meth.* **A273**, p. 625, 1988.

[82] G. Dellacasa, *et al.*, "ALICE Technical Design Report of the Inner Tracking System ITS," 1999.

[83] G. A. *et al.*, "The silicon pixel detector (SPD) for the ALICE experiment," *J. Phys. G: Nucl. Part. Phys.* **30**, pp. 1091–1095, 2004.

[84] E. Gatti, P. Rehak, and J. T. Walton, "Silicon drift chambers - first results and optimum processing of signals," *Nucl. Instrum. Meth.* **226**, p. 129, 1984.

[85] A. Rashevsky *Nuclear Science Symposium Conference Record, 2004 IEEE*, vol. 2, pp. 917–921, 2004.

[86] M. Oinonen *11th Workshop on Electronics for LHC and Future Experiments, Heidelberg*, pp. 92–97, 2005.

[87] D. Nygren, "Future Prospects of the TPC Idea," *Phys. Scripta* **23**, p. 584, 1981.

[88] S. Klein, "The time projection chamber turns 25," *CERN Courier, Jan*, 2004.

[89] G. D. *et al.*, "ALICE Technical Design Report of the Time Projection Chamber," 1999.

[90] J. Alme, *et al.*, "The ALICE TPC, a large 3-dimensional tracking device with fast readout for ultra-high multiplicity events," *Nucl. Instrum. Meth.* **A622**, pp. 316–367, 2010.

[91] F. Sauli, *et al.*, "GEM: A new concept for electron amplification in gas detectors," *Nucl. Instrum. Meth.* **A386**, p. 531, 1997.

[92] P. Cortese, *et al.*, "ALICE Technical Design Report of the High-Level Trigger HLT," 2003.

[93] H. V. Bethe, "Zur Theorie des Durchgangs schneller Korpus- kularstrahlen durch Materie," *Annalen der Physik*, vol. 397, pp. 325–400, 1930.

[94] E. Segre, H. Staub, H. Bethe, J. Ashkin, N. F. Ramsey, and K. T. Bainbridge, *Experimental Nuclear Physics*. John Wiley & Sons, Inc., 1953.

[95] D. Antonzyk, *et al.*, "Performance studies with an ALICE TPC prototype," *Nucl. Instrum. Meth.* **A565**, pp. 551–560, 2006.

[96] Y.Belikov, J.Bracinik, M.Ivanov, and K.Safarik, "TPC tracking and particle identification in high-density environment," *Computing in High Energy and Nuclear Physics, 24-28 March 2003, La Jolla, California*, 2003.

[97] G. Dellacasa, *et al.*, "ALICE Technical Design Report of the Computing," 2005.

[98] P. Cortese, *et al.*, "ALICE Electromagnetic Calorimeter Technical Design Report," 2008.

[99] *ALICE EMCal Physics Performance Report, for submission to the U.S. Department of Energy*, 2009.

[100] J. Allen, *et al.*, "Performance of prototypes for the ALICE electromagnetic calorimeter," *Nucl. Instrum. Meth. A* **615**, pp. 6–13, 2010.

[101] MathWorks, "Matlab," *Version R2010a*, 2010.

[102] T. Awes, *et al.*, "A simple method of shower localization and identification in laterally segmented calorimeters," *Nucl. Instrum. Meth. A* **311**, p. 130, 1992.

[103] G. Dellacasa, *et al.*, "ALICE Technical Design Report of the Photon Spectrometer (PHOS)," 1999.

[104] R. Wigmans, *Calorimetry, Energy Measurement in Particle Physics*. Oxford University Press, first ed., 2000.

[105] R. Engelmann, et al., "Response of a highly segmented extruded lead glass calorimeter to electrons and pions between 15 GeV/c and 45 GeV/c," *Nucl. Instrum. Meth. A* **216**, p. 45, 1983.

[106] G. Conesa, "AliRoot for beginners," *http://aliweb.cern.ch/secure/Offline/sites/aliceinfo.cern.ch.secure.Offline/files/uploads/EMCAL/EMCal_Beginners.pdf*, 2010.

[107] ALICE Collaboration, "AliRoot: ALICE Offline Project," *http://aliceinfo.cern.ch/Offline/*.

[108] S. Agostinelli, *et. al*, "Geant4 - a simulation toolkit," *Nucl. Instrum. Meth.* **A506**, pp. 250–303, 2003.

[109] S. Agostinelli, *et. al*, "Geant4 developments and applications," *IEEE Transactions on Nuclear Science* **53 No. 1**, pp. 270–278, 2006.

[110] FLUKA Team, "FLUKA," *www.fluka.org*.

[111] ALICE Collaboration, "EMCal Documentation," *http://aliceinfo.cern.ch/Offline/Detectors/EMCALOffline.html*.

[112] ALICE Collaboration, "ALICE: Physics Performance Report, Volume II," *J. Phys. G: Nucl. Part. Phys.* **32**, p. 1295, 2006.

[113] Y. Belikov, *et. al*, "Kalman Filtering Application for Track Recognition and Reconstruction in ALICE Tracking System," *ALICE-INT-1997-24*, 1997.

[114] T. Adye, "Unfolding algorithms and tests using RooUnfold," *ISBN 978-92-9083-367-3*, pp. 313–318, 2011.

[115] T. Adye, "RooUnfold: ROOT Unfolding Framework," *http://hepunx.rl.ac.uk/~adye/software/unfold/RooUnfold.html*.

[116] M. J. Oreglia, *A Study of the Reactions psi prime → gamma gamma psi*. Ph.D. Thesis, SLAC-R-236, 1980.

[117] Private conversation with Shingo Sakai, LBNL

[118] C. Campagnari, M. Franklin, "The discovery of the top quark," *Rev.Mod.Phys.*, pp. 137–212, 1997.

[119] M. Heinz, "Heavy flavor measurements using high-pt electrons in the ALICE EMCal," *arXiv:1006.1278*, 2010.

[120] T. Wright, "B-Tagging at CDF and DO, Lessons for LHC," *arXiv:0707.1712*, 2006.

[121] PHENIX Collaboration, "Measurement of bottom versus charm as a function of transverse momentum p_t with electron-hadron correlations in p-p collisions at $\sqrt{s}$ 200 gev," *PRL 103*, 2009.

[122] OpenMP organization, "OpenMP," *http://openmp.org/wp/about-openmp/*.

[123] ALICE Collaboration, "Measurement of electrons from semileptonic heavy-flavour hadron decays in pp collisions at $\sqrt{s} = 7$ TeV," *arXiv:1205.5423*, 2012.

[124] ALICE Collaboration, "Measurement of electrons from beauty hadron decays in pp collisions at $\sqrt{s} = 7$ TeV," *arXiv:1208.1902*, 2012.

[125] ALICE Collaboration, "Measurement of charm production at central rapidity in proton-proton collisions at $\sqrt{s} = 7$ TeV," *arXiv:1111.1553*, 2012.

[126] ALICE Collaboration, "Measurement of inelastic, single- and double-diffraction cross sections in proton–proton collisions at the LHC with ALICE," *arXiv:1208.4968*, 2012.

[127] R. Averbeck, N. Bastid, Z. Conesa del Valle, P. Crochet, A. Dainese, X. Zhang, "Reference heavy flavour cross sections in pp collisions at $\sqrt{s} = 2.76$ TeV, using a pQCD-driven $\sqrt{s}$-scaling of ALICE measurements at $\sqrt{s} = 7$ TeV," *arXiv:1107.3243*, 2011.

[128] A. Festanti, "Heavy-flavour production and nuclear modification factor in Pb-Pb collisions at $\sqrt{s_{NN}} = 2.76$ TeV with ALICE," *Quark Matter 2014, Darmstadt*, 2014.